SUBMESOSCALE VORTICES AND NEAR-INERTIAL WAVES IN COASTAL BUOYANCY-DRIVEN FLOW

A Dissertation

by

LIXIN QU

Submitted to the Office of Graduate and Professional Studies of
Texas A&M University
in partial fulfillment of the requirements for the degree of

DOCTOR OF PHILOSOPHY

Chair of Committee,	Robert Hetland
Committee Members,	Steven DiMarco
	Xiaopei Lin
	Scott Socolofsky
Head of Department,	Shari Yvon-Lewis

August 2019

Major Subject: Oceanography

ABSTRACT

As two ubiquitous features in open oceans, baroclinic instability vortices and near-inertial waves can coexist in coastal zones under certain conditions and exhibit unique features. This study attempts to improve the fundamental understanding of the submesoscale baroclinic instabilities and near-inertial waves in coastal buoyancy-driven flows. Baroclinic instabilities in coastal buoyancy-driven flows exhibit the self-inhibiting feature (the reduction of the growth rate), which is not revealed in the classical quasi-geostrophic theory. The first part of this study explores the non-geostrophic baroclinic instability theory adapted to the scenario with sloping bathymetry and demonstrates that the suppression of instabilities is related to the Rossby wave resonance. A non-dimensional parameter, slope-relative Burger number, is defined for the instability suppression. On the other hand, near-inertial waves in coastal buoyancy-driven flows can be modified by the curved fronts of the instability vortices, which is not revealed in the previous modification theories accounting for straight, jet-like fronts. The second part of this study focuses on the curvature effect of a front on modifying the properties of near-inertial waves. The primary finding is that the waves modified by a baroclinic vortex can be trapped deeper and hence cause deeper mixing than the ones modified by a front without curvature. Furthermore, to better simulate coastal buoyancy-driven flows, the simulation errors caused by temporally subsampling winds are quantified in the last part of this study. The primary finding is that the simulation error is proportional (1:1) to the fraction of the energy missing in the high-frequency wind caused by subsampling. Analyzing the fast Fourier transformation spectrum of a single-point wind measurement in the simulation region is helpful for estimating simulation errors due to temporal resolution.

ACKNOWLEDGMENTS

I would like to acknowledge Professor Robert Hetland for invaluable research guidance and philosophy, freedom to pursue "crazy" research ideas, and an enjoyable graduate school experience. I would like to thank the members of my committee, Professors Steven DiMarco (TAMU), Xiaopei Lin (OUC), and Scott Socolofsky (TAMU), for being supportive to my work and career and for many valuable suggestions. I would like to thank Professor Leif Thomas (Stanford) for his guidance leading me to the submesoscale regime. Professor John Taylor (Cambridge) is also gratefully acknowledged for teaching me DIABLO and guiding me to a turbulent ocean. I also would like to acknowledge my colleagues, Veronica Ruiz Xomchuk, Dr. Tingting Zu, Dr. Kristen Thyng, Dr. Daijiro Kobashi, and Arthur Ramos, for their help and support.

Chapter 2 is based on an article submitted to the Journal of Physical Oceanography, co-authored by Professor Robert Hetland.

Chapter 3 is based on a manuscript in preparation, co-authored by Professors Robert Hetland and Leif Thomas.

Chapter 4 is based on an article published in the Journal of Geophysical Research - Oceans, co-authored by Professor Robert Hetland.

CONTRIBUTORS AND FUNDING SOURCES

Contributors

This work was supported by a dissertation committee consisting of Professors Robert Hetland (advisor) and Steven DiMarco of the Department of Oceanography, Professor Xiaopei Lin at the Ocean University of China, and Professor Scott Socolofsky of the Department of Civil Engineering.

The numerical simulation framework used in Chapter 2 was developed by Professor Robert Hetland. The hydrographic data used in Chapter 3 was provided by Professor Steven DiMarco. The numerical method used in Chapter 3 was developed by Dr. Daniel Whitt at the National Center for Atmospheric Research. The realistic model used in Chapter 3 is maintained by the lab of Professor Robert Hetland. Constructive suggestions are from Professor Leif Thomas and Dr. Jacob Wenegrat at Stanford University and Professor John Taylor at the University of Cambridge when preparing the manuscripts.

All other work conducted for the dissertation was completed by the student independently.

Funding Sources

Graduate study was supported by a scholarship from China Scholarship Council, the grant 18-132-000-A673 from Texas General Land Office, the grant 2018SP-S-Qu-GIA from Texas Sea Grant, and the scholarships/fellowships from the Department of Oceanography.

NOMENCLATURE

Ri	Richardson Number
Ri_b	Bulk Richardson Number
Ro	Rossby Number
R_d	Rossby Deformation Radius
Bu	Burger Number
S	Slope Burger Number
S_H	Horizontal Slope Burger Number
S_r	Slope-relative Burger Number
δ	Slope Parameter
δ_r	Slope-relative Parameter
α	Bottom Slope
M^2	Horizontal Buoyancy Gradient
N^2	Vertical Buoyancy Gradient
f	Coriolis Paramter / Inertial Frequency
f_{eff}	Effective Inertial Frequency
f^*_{eff}	Modified Effective Inertial Frequency
ζ_s	Shearing Vorticity
ζ_c	Curvature Vorticity
ADCP	Acoustic Doppler Current Profiler
CTD	Conductivity-Temperature-Depth
FFT	Fast Fourier Transform
GCM	General Circulation Model

HYCOM	Hybrid Coordinate Ocean Model
MCH	Mechanisms Controlling Hypoxia
NDBC	National Data Buoy Center
NG	Non-Geostrophic
NIW	Near-Inertial Wave
QG	Quasi-Geostrophic
ROMS	Regional Ocean Modeling System
RMS	Root-Mean-Square
STD	Standard Deviation
TABS	Texas Automated Buoy System
WKB	Wentzel-Kramers-Brillouin

TABLE OF CONTENTS

Page

LIST OF FIGURES

FIGURE Page

LIST OF TABLES

TABLE Page

1. INTRODUCTION

As an important ocean energy reservoir, ocean eddies carry substantial kinetic energy at the sub-inertial frequencies (Ferrari and Wunsch, 2009); these spinning features are ubiquitous but are especially energetic near ocean fronts at all scales. Ocean eddies can be mesoscale within large-scale, geostrophic fronts, or submesoscale within ocean mixed layers (Boccaletti et al., 2007; Shcherbina et al., 2013) and along fronts of mesoscale eddies (Callies et al., 2015; Brannigan et al., 2017). Ocean mesoscale eddies have been extensively investigated in the last decades from both the theoretical and observational perspectives, whereas the submesoscale eddies have not been well understood. The generation mechanism of the submesoscales is still a debate in the oceanography community with two proposed mechanisms – the non-geostrophic baroclinic instabilities and the mesoscale-driven surface frontogenesis (Lapeyre and Klein, 2006; Boccaletti et al., 2007; Callies et al., 2016).

The classical non-geostrophic baroclinic instability theory interprets submesoscales by describing the dimension and growth rate of instability modes, based on an assumption of flat topography (Stone, 1966, 1970, 1971; Fox-Kemper et al., 2008). This assumption is valid for the mixed layer instabilities but seems not reasonable for the baroclinic instabilities in coastal buoyancy-driven flows that are often over continental shelves. Although the classical non-geostrophic theory does not include the topographic effect, there are still several modified theories accounting for slopping topography. Blumsack and Gierasch (1972) adapted the classical Eady's problem (Eady, 1949) into the scenario with a sloping bottom; but the theory is in the quasi-geostrophic (QG) regime and hence not applicable to the energetic submesoscales where QG might not be a reasonable assumption (Hetland, 2017). By rotating coordinates, Wenegrat et al. (2018) adapted the classical Stone's problem (Stone, 1970) into the scenario with a sloping surface and a sloping bottom to study submesoscales at bottom boundary layers; although this theory is in the non-geostrophic regime, the assumption of the parallel, sloping surface and bottom seems not reasonable for coastal buoyancy-driven flows that are usually with flat surfaces. Unfortunately, a non-geostrophic baroclinic insta-

bility theory for coastal buoyancy-driven flows has not been established, which is very challenging. To better understand the fundamental physics of the submesoscales in coastal buoyancy-driven flows, we will turn to seek the limit within which the existing theories can be approximately applicable, and then use them to explore the controlling mechanism of the instability suppression which is a unique feature of the submesoscales in coastal buoyancy-driven flows.

As another important ocean energy reservoir, near-inertial waves (NIWs) dominate oceanic kinetic energy at the frequencies near the local Coriolis parameter (Ferrari and Wunsch, 2009). NIWs are the internal gravity waves with the nearly inertial frequencies and they are ubiquitous in the ocean (Alford et al., 2016). One outstanding feature of the internal gravity waves is that the wave motions are associated with strong velocity shear. This feature can induce wave breaking such that NIWs can make a significant contribution to the mixing in the ocean interior (Wunsch and Ferrari, 2004). NIWs are most intense at the major large-scale ocean fronts, such as the Antarctic Circumpolar Current, Kuroshio Current, and Gulf Stream. These regions underlie the westerlies where the storm tracks pass, and hence the NIWs can be sufficiently stimulated and energized (Alford, 2003). Whalen et al. (2012) estimated the global dissipation rate and diffusivity in the upper ocean based on the ARGO float data – the hotspots of dissipation and diffusivity match the locations of the major ocean fronts. High dissipation rate implies that the kinetic energy is energetically transferred to the small-scale turbulence, and high diffusivity indicates that the vertical mixing is also enhanced during the energy transfer. The correspondence between the NIWs and the mixing hotspots indicates that NIWs can propagate the energy towards the ocean interior and transfer the energy to the internal waves with higher frequencies and eventually to small-scale turbulence, which causes significant mixing and dissipation (Ferrari and Wunsch, 2009).

Because of the correspondence between the NIWs and the large-scale fronts, it has been hypothesized that the NIW-front interactions could damp the large-scale circulation and energize the internal wave continuum and hence could be important for closing the kinetic energy budgets of both types of motion (Polzin and Lvov, 2011; Nagai et al., 2015; Wagner and Young, 2016). The NIW-front interaction is related to the fact that the properties of NIWs can be significantly modi-

fied by the vorticity of an ocean front. An anti-cyclonic jet can reduce the minimum (allowable) frequency to the effective inertial frequency (which is less than the inertial frequency in the case of the anti-cyclonic front) such that the waves with the inertial frequency can vertically propagate. This modification leads to the trapping of NIWs at anti-cyclonic fronts, where the consequent wave breaking and mixing can occur. There are substantial observations showing that the enhanced dissipation in the ocean interior are highly related to the negative vorticity (Perkins, 1976; Kunze and Sanford, 1984; Kunze et al., 1995). This process ensures an efficient transfer of energy through the ocean thermocline, which is referred to as the near-inertial chimney effect (Lee and Niiler, 1998). To vertically propagate, NIWs must require potential energy and hence extract kinetic energy from the balanced flow (Xie and Vanneste, 2015). This process is referred to as the stimulated generation; it means that NIWs are firstly generated by the energy injection from stimulating forcing and subsequently gain additional energy through the wave-front interaction. The wave-front interaction can also energize the internal wave continuum by triggering wave-wave interactions and hence facilitate the energy transfer from NIWs to higher frequency modes (Wagner and Young, 2016).

In addition to the vorticity of fronts, the lateral density gradients can also modify the properties of NIWs to cause the energy cascade and transfer across the motions with a range of spatial scales (Thomas, 2017). Beyond the vorticity, the baroclinity of a front can further reduce the minimum (allowable) frequency so that NIWs can be unstable to the parametric subharmonic instabilities (Thomas and Taylor, 2014). The parametric subharmonic instabilities can extract kinetic energy from the NIWs and transfer the energy to secondary instabilities and eventually to potential energy (by turbulent mixing) and heat (by molecular dissipation). Furthermore, the baroclinity can cause the four characteristics of NIWs to be symmetric with respect to the isopycnal slope. Particularly, the waves with the effective inertial frequency can either propagate vertically or horizontally; this leads to the focusing reflection of the wave characteristics at the surface, which can facilitate the energy transfer from the NIWs to small-scale turbulence and hence enhance the viscous dissipation and turbulent mixing (Grisouard and Thomas, 2015, 2016).

However, most of the previous studies focused on the modifications of NIWs at straight, jet-like

fronts (Mooers, 1975; Kunze, 1985; Whitt and Thomas, 2013; Thomas, 2017; Whitt et al., 2018), whereas only a few have focused on curved, vortex-like fronts (Kunze and Boss, 1998; Joyce et al., 2013). In coastal zones, NIWs and vortex-like fronts can coexist under certain conditions and interact with each other. Submesoscale eddies can be quite energetic in some coastal zones because of the baroclinic instabilities in buoyancy-driven flows. For example, recent studies have highlighted the enhanced variability over the Texas-Louisiana shelf in the northern Gulf of Mexico (Marta-Almeida et al., 2013) due to the baroclinic instabilities along the Mississippi/Atchafalaya River plume front (Hetland, 2017). On the other hand, near-inertial motions over the Texas-Louisiana shelf are significantly energetic, because they are resonantly forced by the land-sea breeze that is with the frequency close to the local Coriolis parameter (DiMarco et al., 2000b; Zhang et al., 2009, 2010). However, the modifications of NIWs by a strongly curved, baroclinic front are simply not well understood. It is hoped that this study will improve the understanding of the modifications at vortex-like fronts, which could be helpful for further exploring the NIW-front interactions and hence the energy transfers across scales and regimes.

As a typical buoyancy-driven flow in coastal zones, river plumes are of the central importance of understanding coastal ecosystems and environments (Horner-Devine et al., 2015). As a primary forcing agent for coastal buoyancy-driven flows, wind plays an important role in controlling the position and evolution of a river plume. River plumes move onshore and offshore in response to downwelling and upwelling winds, respectively. An upwelling wind can pull a river plume offshore and reduce the along-shore freshwater transport (Masse and Murthy, 1990; Kourafalou et al., 1996). Under upwelling conditions, motions at the seaward front of a plume are dominated by the Ekman physics (Fong et al., 1997). A downwelling wind can shrink the surface expression of a river plume, vertically tilt the isopycnals, and increase the along-coast transport of freshwater (Moffat and Lentz, 2012). In this sense, wind stress affects freshwater distribution asymmetrically, because freshwater is moving onshore and downcoast during downwelling and moving offshore during upwelling (Hetland and Hsu, 2013). Consequently, the temporal history of wind forcing and the associated accuracy are highly important for accurately simulating the spatial extent and

structure of a river plume.

Another wind effect on river plumes is wind-induced mixing (Masse and Murthy, 1992). In the near-field region of a river plume, shear instabilities are dominant due to the inertia and shoaling of the estuarine jet. After freshwater leaves the near-field region, the shear mixing is suppressed, and the wind mixing becomes dominant (Hetland, 2010). Fong and Geyer (2001) constructed a conceptual model to describe the far-field mixing during an upwelling wind event. As the upwelling winds spread the plume offshore, the plume is stretched wider, and, because of the conservation of buoyancy, the plume must also become thinner. This shoaling increases the depth-averaged Ekman flow confined to the plume, and shear instabilities may be induced. Entrainment at the interface thickens the upper layer until the bulk Richardson number is again above the critical value, 0.25. The vertical spatial scale characterizing this mixing effect is referred to as the critical depth (Lentz, 2004; Hetland, 2005). The critical depth suggests that the portion of the plume with layer thickness larger than the critical depth is protected from the wind-induced mixing. Wind-induced mixing in a river plume has a significant impact on the material transport such as larvae, sediments, and pollutants, and is an essential mechanism in the terrestrial-oceanic water cycle (Epifanio and Garvine, 2001; Chant, 2012). Therefore, the temporal history of wind forcing and the associated accuracy are very important for accurately simulating the density structure of a river plume.

To our knowledge, the simulation errors caused by temporally subsampling of winds have not been investigated quantitatively in the scenario of coastal buoyancy-driven flows, and hence we simply do not have a rationale for selecting wind forcing for river plume simulations. One goal of this study is to quantify the temporal resolution of wind forcing required for river plume simulations. It is hoped that this study could provide general guidance on properly selecting wind forcing and improve our ability on simulating coastal buoyancy-driven flows.

This dissertation is organized as follows. Chapter 2 will focus on the submesoscale baroclinic instabilities in coastal buoyancy-driven flows; particularly, it will exhibit the instability suppression in coastal buoyancy-driven flows and demonstrate the mechanism controlling the instability suppression. Chapter 3 will focus on the NIWs in a coastal buoyancy-driven flow; particularly,

it will present the modifications of NIWs by a baroclinic vortex and demonstrate the curvature effect of a vortex on modifying NIWs. Chapter 4 will focus on the numerical simulation of coastal buoyancy-driven flows; particularly, it will quantify the simulation errors caused by temporally subsampling of winds and provide suggestions on properly selecting wind forcing for river plume simulations.

2. NON-GEOSTROPHIC BAROCLINIC INSTABILITY IN BUOYANCY-DRIVEN FLOW OVER SLOPING BATHYMETRY

2.1 Introduction

Baroclinic instabilities release potential energy stored in horizontal density gradients, creating unsteady and evolving motions in the flow at approximately the first baroclinic deformation radius. As such, the Burger number, Bu, associated with baroclinicly unstable flow is $Bu = R_d L^{-1} = RoRi^{1/2} \sim 1$ (Eady, 1949; Stone, 1966, 1970). Beyond this, there are two general categories of baroclinic instabilities associated with the Rossby number, Ro, of the flow: mesoscale instabilities within the large-scale, geostrophic fronts with $Ro \ll 1$ and $Ri \gg 1$, and submesoscale instabilities with $Ro \sim 1$ and $Ri \sim 1$ (Boccaletti et al., 2007). Examples of the submesoscale instabilities include instabilities within the ocean mixed layer (Boccaletti et al., 2007; Shcherbina et al., 2013), along the fronts of mesoscale eddies (Callies et al., 2015; Brannigan et al., 2017), and, rarely, in certain coastal buoyancy-driven flows (Hetland, 2017).

Coastal buoyancy-driven flows are often associated with stronger lateral density gradients than open ocean fronts, but are seldom observed to be associated with instabilities; in particular, baroclinic instabilities are seldom observed in river plumes, even though lateral buoyancy gradients within the fronts are strong (Horner-Devine et al., 2015). External forcing agents, such as winds and tides, could suppress baroclinic instabilities through mixing processes. However, it has been demonstrated that a rotating plume without the external forcing can be very stable over many rotational periods (Fong and Geyer, 2002; Lentz and Helfrich, 2002; Hetland, 2005; Horner-Devine et al., 2006; Hetland, 2017); this implies that the suppression can be due to the intrinsic inhibiting effects of the front. Hetland (2017) examined the suppression of baroclinic instabilities in a coastal buoyancy flow using numerical model results and quasi-geostrophic (QG) theory of buoyancy driven flow over a sloping bottom. However, the QG assumption may not be reasonable in energetic coastal fronts.

This paper explores the non-geostrophic baroclinic instability theory adapted to the scenario with a sloping bathymetry. Both layered and continuously stratified models are used to demonstrate the suppression of instabilities in buoyancy-driven flow over a sloping bottom, which is not revealed in the classical QG theory (Blumsack and Gierasch, 1972). In particular, this paper attempts to seek a non-dimensional parameter for predicting the instability suppression and the underlying mechanism controlling the suppression in the buoyant flow regime.

2.2 Theory

2.2.1 Layered Model of Non-Geostrophic Baroclinic Instability

Phillips (1954) transformed the continuously stratified fluid to a two-layer system and constructed the layered model of QG baroclinic instabilities. Sakai (1989) investigated the ageostrophic instabilities using an ageostrophic version of Phillips model. We adapt Sakai model to the scenario with sloping bottom and surface (hereinafter referred to as the adapted Sakai model). The schematics of Sakai model and the adapted Sakai model are shown in Fig. 2.1. The adapted Sakai model is a rotating two-layer channel with the sloping topography and mean flow in the thermal wind balance. Considering the time scale as f^{-1}, the horizontal length scale as the Rossby deformation radius $R_d = \frac{\sqrt{\frac{1}{2}g'H_0}}{f}$, and the vertical length scale as H_0 (see the scale analysis in Appendix A), the dimensionless form of the equations governing the perturbations is

$$
\begin{aligned}
\frac{\partial u_1}{\partial t} + Ri_b^{-1/2}\frac{\partial u_1}{\partial x} - v_1 &= -\frac{\partial p_1}{\partial x}\ , \\
\frac{\partial v_1}{\partial t} + Ri_b^{-1/2}\frac{\partial v_1}{\partial x} + u_1 &= -\frac{\partial p_1}{\partial y}\ , \\
\frac{\partial u_2}{\partial t} - Ri_b^{-1/2}\frac{\partial u_2}{\partial x} - v_2 &= -\frac{\partial p_2}{\partial x}\ , \\
\frac{\partial v_2}{\partial t} - Ri_b^{-1/2}\frac{\partial v_2}{\partial x} + u_2 &= -\frac{\partial p_2}{\partial y}\ , \\
\frac{\partial p_2 - p_1}{\partial t} + Ri_b^{-1/2}\frac{\partial p_2 - p_1}{\partial x} &= 2H_1\frac{\partial u_1}{\partial x} + 2\frac{\partial H_1 v_1}{\partial y}\ , \\
\frac{\partial p_2 - p_1}{\partial t} - Ri_b^{-1/2}\frac{\partial p_2 - p_1}{\partial x} &= -2H_2\frac{\partial u_2}{\partial x} - 2\frac{\partial H_2 v_2}{\partial y}\ ,
\end{aligned}
\tag{2.1}
$$

subject to

$$v_1|_{y=\pm Y_{max}} = 0,$$
$$v_2|_{y=\pm Y_{max}} = 0, \tag{2.2}$$

where the subscript 1 (2) denotes the variables in the upper (lower) layer, u is the along-slope velocity, v is the across-slope velocity, p is the pressure, $\pm Y_{max}$ are the across-slope boundaries, $H_1 = 1 - (\delta + 1)Ri_b^{-1/2}y$ is the thickness of the upper layer, and $H_2 = 1 + (\delta + 1)Ri_b^{-1/2}y$ for the lower layer. $Ri_b = \frac{g^{'}H_0}{2U_0^2}$ is the bulk Richardson number, where g' is the reduced gravity, H_0 is the dimensional average thickness, and U_0 is the dimensional mean flow (U_0 in the upper layer and $-U_0$ in the lower layer). $Y_{max} \equiv \frac{\Delta H}{(\delta+1)Ri_b^{-1/2}}$ insures that the total change of the layer thickness is ΔH ($\Delta H = 0.5$ is used in this study). $\delta = \frac{\alpha g^{'}}{2U_0 f}$ is the slope parameter, the ratio of the bottom slope α and the isopycnal slope $\frac{2U_0 f}{g^{'}}$. Here, δ has an opposite sign convention compared to the original one in the study of Blumsack and Gierasch (1972), such that in this work positive δ represents the common case of buoyancy-driven flow over a continental shelf, where the isopycnal and bathymetric slopes are opposite. In this study, we will only focus on the scenarios with positive δ, which is referred to as the buoyant flow regime.

Assume a wave-like solution $\phi = \widetilde{\phi}(y)e^{i(kx-\sigma t)}$, where $k = k^* R_d$ is the dimensionless along-slope wavenumber and $\sigma = f^{-1}\sigma^*$ is the dimensionless wave frequency. Substituting it into Eq. (2.1) and (2.2) yields an eigenvalue problem (see Appendix A). The growth rate of instabilities $\sigma_i = Imag[\sigma]$ is obtained by numerically conducting the linear stability analysis. DEDALUS is used in stability analysis, which is a PDE solver that uses spectral methods (Burns et al., 2016). Fig. 2.1 shows the normalized growth rate in the flat-bottom case ($\delta = 0$) and the sloping-bottom case ($\delta = 0.5$); more discussion is in Section 2.3.1.

2.2.2 Continuously Stratified Model of Non-Geostrophic Baroclinic Instability

Eady (1949) built a continuously stratified QG framework for study the baroclinic instabilities. Blumsack and Gierasch (1972) adapted Eady model to the scenario with a sloping bottom (hereinafter referred to as the QG model). Stone (1966, 1970, 1971) extended Eady model (Eady, 1949) to the non-geostrophic limit and constructed the continuously stratified model of non-geostrophic

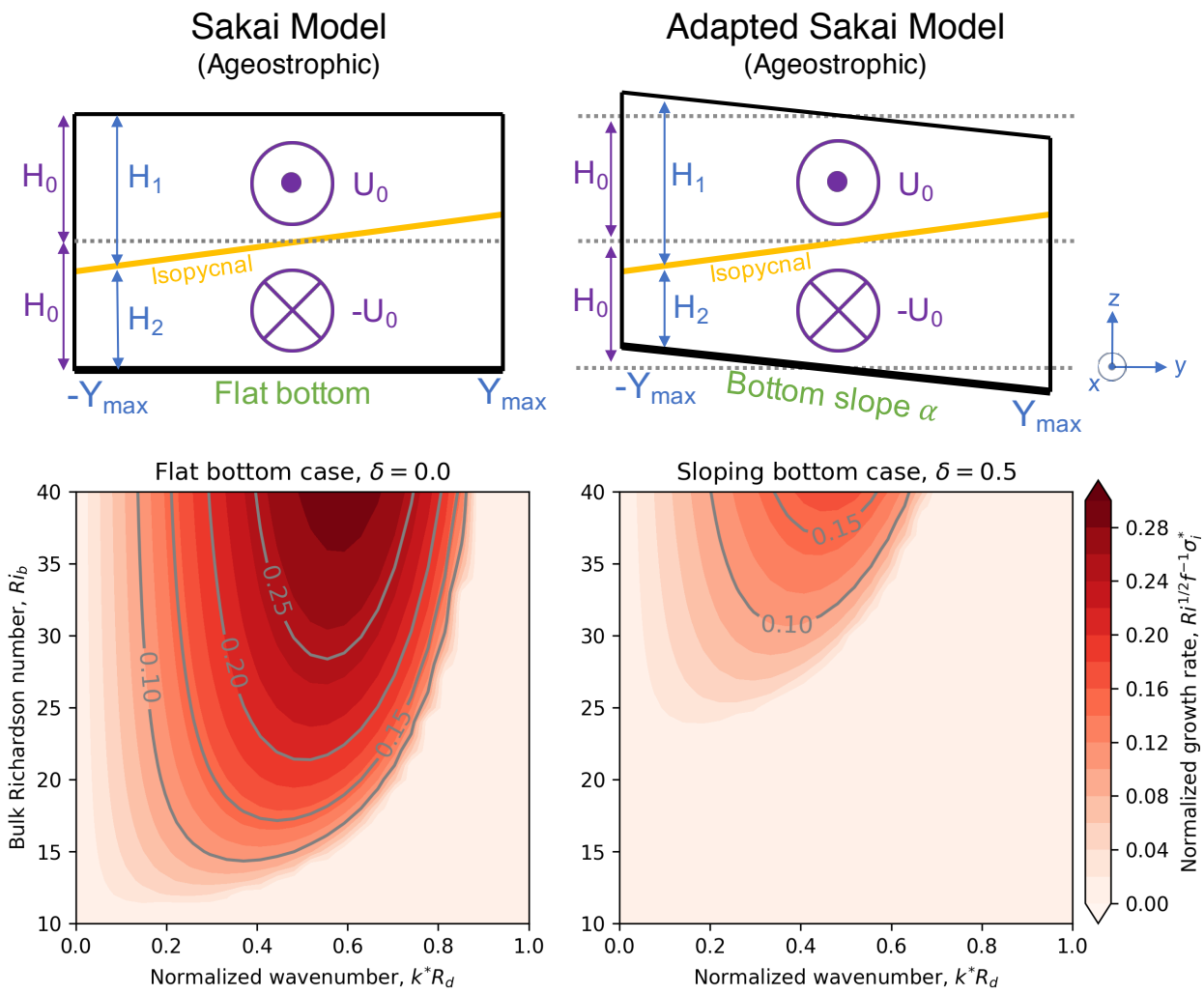

Figure 2.1: Normalized growth rate ($\hat{\sigma}_i = Ri_b^{1/2}\sigma_i = Ri_b^{1/2}f^{-1}\sigma_i^*$) as a function of normalized wavenumber ($\hat{k} = k^*R_d$) and bulk Richardson number ($Ri_b = \frac{g'H_0}{2U_0^2}$) based on Sakai model ($\delta = 0.0$) and the adapted Sakai model ($\delta = 0.5$).

baroclinic instabilities. We use the modified model (Wenegrat et al., 2018), which adapts Stone model to the scenario with sloping bottom and surface (hereinafter referred to as the adapted Stone model). The schematic of the QG and adapted Stone models are shown in Fig. 2.2. In the adapted Stone model, the coordinates are rotated to align with the sloping bottom. The background buoyancy has a constant vertical gradient N^2 and a constant horizontal gradient M^2, and the background flow is constrained by the thermal wind relation. Considering the time scale as f^{-1}, the horizontal length scale as U/f, and the vertical length scale as H (see the scale analysis in Appendix B), the dimensionless form of the equations governing the perturbations in the rotated coordinates is

$$\begin{aligned}
\frac{\partial u}{\partial t} + u_0\frac{\partial u}{\partial x} + w\frac{\partial u_0}{\partial z} - v\ cos\theta - \epsilon\ w\ sin\theta &= -\mathrm{Ri}\ \frac{\partial p}{\partial x}\ , \\
\frac{\partial v}{\partial t} + u_0\frac{\partial v}{\partial x} + u\ cos\theta &= -\mathrm{Ri}\ \frac{\partial p}{\partial y} - \delta\ b\ cos\theta\ , \\
\epsilon^2\frac{\partial w}{\partial t} + \epsilon^2 u_0\frac{\partial w}{\partial x} + \epsilon\ u\ sin\ \theta &= -\mathrm{Ri}\ \frac{\partial p}{\partial z} + \mathrm{Ri}\ b\ cos\theta\ , \\
\frac{\partial b}{\partial t} + u_0\frac{\partial b}{\partial x} + v\frac{\partial b_0}{\partial y} + w\frac{\partial b_0}{\partial z} &= 0\ , \\
\frac{\partial u}{\partial x} + \frac{\partial v}{\partial y} + \frac{\partial w}{\partial z} &= 0\ ,
\end{aligned} \tag{2.3}$$

subject to

$$\begin{aligned}
w|_{z=0} &= 0, \\
w|_{z=1} &= 0,
\end{aligned} \tag{2.4}$$

where u is the along-shore velocity, v is the across-shore velocity, and w is the vertical velocity, p is the pressure, b is the buoyancy, θ is the bottom slope angle, $u_0 = \frac{z}{cos\theta}$ is the mean along-shore velocity, $b_0 = (cos\theta - \epsilon Ri^{-1} sin\theta)z - (\delta+1)Ri^{-1}cos\theta\ y$ is the mean buoyancy, and z=0 (z=1) is the sloping bottom (surface). $\mathrm{Ri} = N^2H^2U^{-2} = N^2f^2M^{-4}$ is the Richardson number. $\delta = \alpha N^2 M^{-2}$ is the slope parameter, the ratio of the bottom slope α and the isopycnal slope $\frac{M^2}{N^2}$. $\epsilon = fHU^{-1} = f^2M^{-2}$ is the non-hydrostatic parameter (Stone, 1971).

Noting that the surface is also assumed to be tilted, the adapted Stone model is intrinsically suitable for the baroclinic instabilities in a tilted bottom boundary layer, but seems not directly applicable to the situation with a flat surface that is not parallel with the tilted bottom. One way is to

adapt Stone model to the scenario with a flat surface, but this presents two challenges for theoretical approaches: first, making the uniform depth assumption like Eq. (2.4) is theoretically invalid; second and subsequently, an ansatz with the wave form in the across-slope direction becomes theoretically invalid. Consequently, instead of adapting Stone model to the flat-surface scenario, we will address the feasibility of the adapted Stone model (Wenegrat et al., 2018) in the flat-surface cases, e.g., baroclinic instabilities in a coastal buoyancy-driven flow over a continental shelf.

Assume a wave-like solution $\phi = \widetilde{\phi}(z)e^{i(kx+\lambda y-\sigma t)}$, where $k = \frac{f}{U}k^*$ is the dimensionless along-slope wavenumber, $\lambda = \frac{f}{U}\lambda^*$ is the dimensionless along-slope wavenumber, and $\sigma = f^{-1}\sigma^*$ is the dimensionless wave frequency. Substituting it into Eq. (2.3) and (2.4) yields the eigenvalue problem of the adapted Stone model (see Appendix B). DEDALUS is also employed to calculate the growth rate of instabilities $\sigma_i = Imag[\sigma]$. Fig. 2.2 shows the normalized growth rate based on the QG model ($Ri \gg 1$) and the adapted Stone model ($Ri = 2.0$); more discussion is in Section 2.3.2. To keep consistent with the normalization in the QG model (Blumsack and Gierasch, 1972), the dimensionless variables σ_i and k are converted to the normalized variables $\hat{\sigma}_i$ and $\hat{k}$. The normalized wavenumber $\hat{k}$ is defined by the normalization of the dimensional wavenumber k^* by the Rossby deformation radius $R_d = \frac{NH}{f}$; that is, according to the scaling relations,

$$\hat{k} \equiv R_d k^* = (\frac{1}{L})(\frac{NH}{f})k = (\frac{1}{Uf^{-1}})(\frac{NH}{f})k = NHU^{-1}k = Ri^{1/2}k \, . \tag{2.5}$$

The normalized growth rate $\hat{\sigma}_i$ is defined by the normalization of the dimensional growth rate σ_i^* by the advection time scale R_d/U,

$$\hat{\sigma}_i \equiv \frac{R_d}{U}\sigma_i^* = (NHU^{-1})f^{-1}\sigma_i^* = Ri^{1/2}\sigma_i^* f^{-1} = Ri^{1/2}\sigma_i \, . \tag{2.6}$$

With regard to the normalization in the adapted Sakai model, the wavenumber k^* is normalized by R_d, so $\hat{k} \equiv R_d k^*$ is equivalent to the k in the adapted Sakai model, while the dimensionless $\sigma_i \equiv \sigma_i^* f^{-1}$ still needs to be converted as Eq. (2.6). For the rest of this paper, we will use the normalized variables ($\hat{\sigma}_i$ and $\hat{k}$) to describe the properties of baroclinic instabilities.

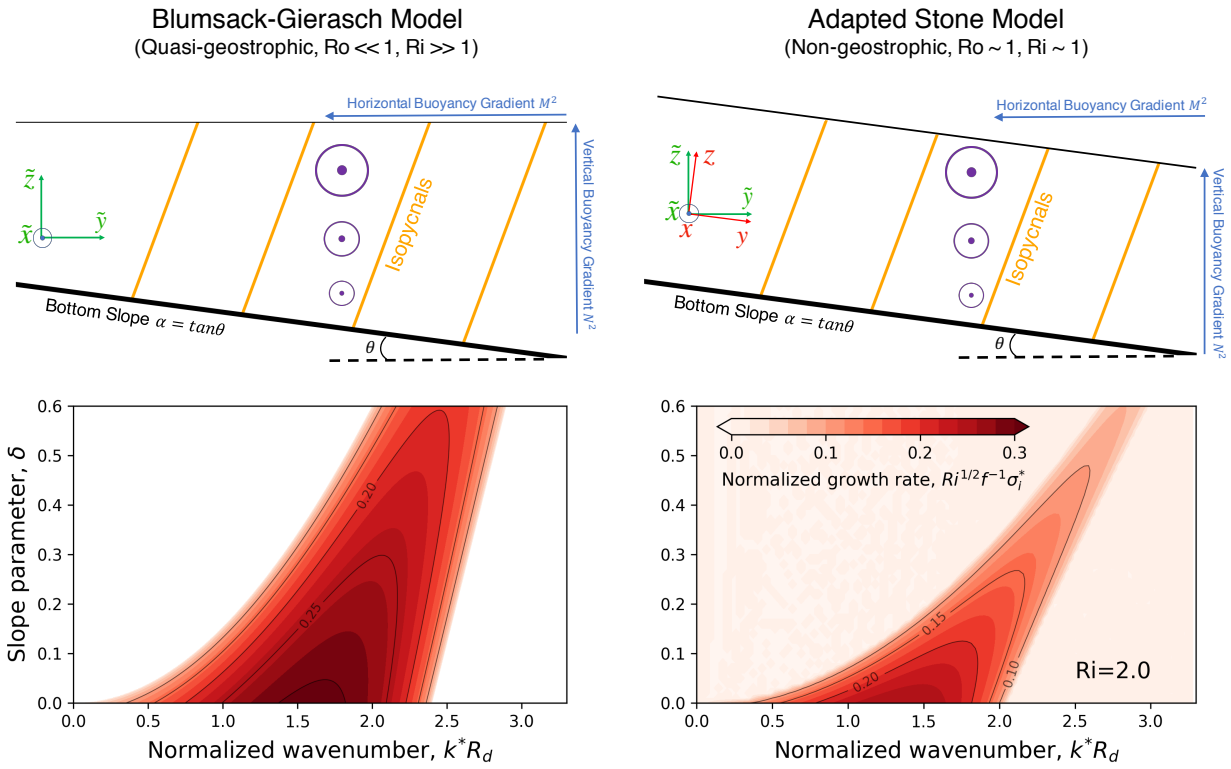

Figure 2.2: Normalized growth rate ($\hat{\sigma}_i = Ri^{1/2}\sigma_i^* f^{-1}$) as a function of normalized wavenumber ($\hat{k} = k^* R_d$) and slope parameter $\delta = \alpha N^2 M^{-2}$ based on Blumsack-Gierasch model ($Ro \ll 1$, $Ri \gg 1$) and the adapted Stone model ($Ro \sim 1$, $Ri \sim 1$). $Ri = 2.0$ is used in the adapted Stone model.

2.3 Results

Suppression of baroclinic instabilities over sloping bathymetry, in terms of the amplitude of the instabilities, occurs when the horizontal slope Burger number $S_H = M^2 f^{-2} \alpha \gtrsim 0.2$ (Hetland, 2017). S_H can be written as a ratio of the inertial length scale to the front width; the criterion implies that instabilities can be suppressed when the front is too narrow to fit the vortices. In this study, we will also address the suppression of instabilities but from the temporal perspective - the growth rate of instabilities.

2.3.1 Suppression of Instabilities in the Layered Model

Based on the adapted Sakai model, baroclinic instabilities start to be suppressed, meaning the growth rate of the instabilities is reduced, when the bottom slope increases (see Fig. 2.1). Also, instabilities are found to be suppressed with decreasing bulk Richardson number Ri_b. Fig. 2.3 shows the transition of the normalized grow rate $\hat{\sigma}_i = Ri^{1/2} \sigma_i^* f^{-1}$ if Ri_b shifts from 40 to 20 - instabilities are significantly inhibited in the $Ri_b = 20$ case and can be completely suppressed if the slope parameter δ is sufficiently large.

As noted above, the suppression of instabilities has opposite dependencies on Ri_b and δ. To further demonstrate it, the maximum grow rate as a function of Ri_b and δ is calculated. The maximum normalized growth rate $\hat{\sigma}_{i,max}$ is defined as the maximum of the normalized growth rate across all wavenumbers $\hat{k} = k^* R_d$ for given Ri_b and δ. Fig. 2.4 shows the $\hat{\sigma}_{i,max}$ in the parameter space of Ri_b and δ. $\hat{\sigma}_{i,max}$ also exhibits opposite dependencies on Ri_b and δ, with the suppression as Ri_b decreases and δ increases. Baroclinic instabilities are completely suppressed at low Ri_b and high δ. To understand the suppression of baroclinic instabilities, we will identify the primary coefficient linked with the suppression and explore the controlling mechanism.

A new parameter, slope-relative Burger number $S_r = \frac{N}{f}(\alpha + \frac{M^2}{N^2})$, is considered as the coefficient controlling the suppression of instabilities in the non-geostrophic case. Compared to the conventional slope Burger number $S = \frac{N}{f}\alpha$, the slope-relative Burger number S_r uses a bottom slope relative to the isopycnal slope, $\frac{M^2}{N^2}$. Thus, if the slopes are aligned, with the bottom par-

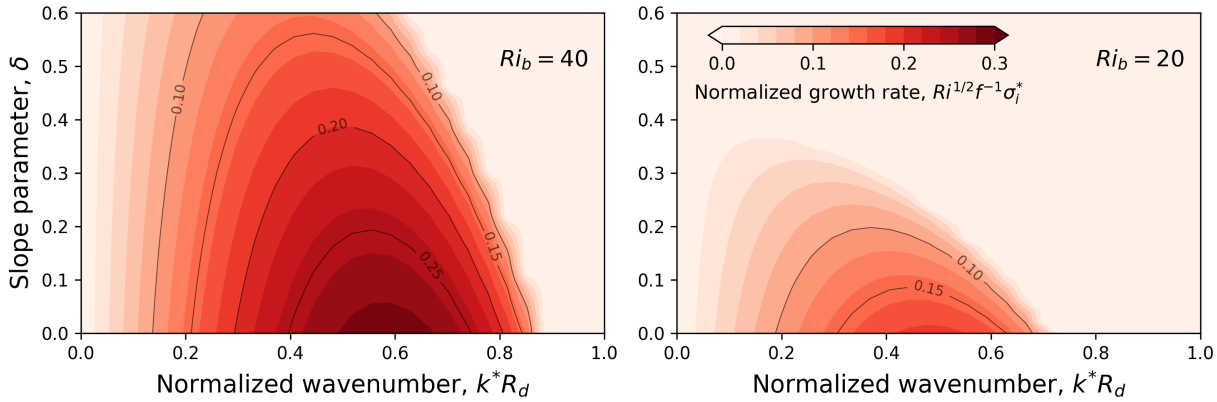

Figure 2.3: Normalized growth rate ($\hat{\sigma}_i = Ri^{1/2}\sigma_i^* f^{-1}$) in the cases with Richardson number $Ri_b = 40$ (left) and $Ri_b = 20$ (right). $\hat{\sigma}_i$ is shown as a function of normalized wavenumber ($\hat{k} = k^* R_d$) and slope parameter ($\delta = \frac{\alpha g'}{2U_0 f}$).

allel to the isopycnals, then $S_r = 0$. The slope-relative Burger number is based on the Burger number using the layer thicknesses in the adapted Sakai model; $H_1^* = H_0 - (\alpha + \frac{M^2}{N^2})y^*$ and $H_2^* = H_0 + (\alpha + \frac{M^2}{N^2})y^*$ may be used to write a Burger number as $Bu = \frac{NH}{fL} = \frac{N}{f}(\alpha + \frac{M^2}{N^2})$. Noticing that the dimensionless layer thickness is $H_1 = 1 - S_r y$ and $H_2 = 1 + S_r y$ (see Appendix A), the physical meaning of the slope-relative Burger number is that S_r represents the gradient of potential vorticity supplemented by topographic effects.

The slope-relative Burger number can be written in terms of the Richardson number Ri and the slope parameter δ as

$$S_r = \frac{N}{f}(\alpha + \frac{M^2}{N^2}) = (\alpha N^2 M^{-2} + 1)(N^2 f^2 M^{-4})^{-1/2} = (\delta + 1)Ri^{-1/2} = \delta_r Ri^{-1/2}\,. \qquad (2.7)$$

where $\delta_r = 1 + \delta = \frac{\alpha + M^2/N^2}{M^2/N^2}$ is the slope-relative parameter, with an interpretation similar to the slope-relative Burger number S_r. For clarity, hereafter $1 + \delta$ will be written as δ_r. The distribution of S_r^2 in $Ri_b - \delta$ space (middle panel of Fig. 2.4) is proportional to the maximum normalized growth rate $\hat{\sigma}_{i,max}$ (right panel of Fig. 2.4). In addition, instabilities are completed suppressed for $S_r^2 \gtrsim 0.1$. The linear relation between S_r^2 and $\hat{\sigma}_{i,max}$ does not hold in the QG limit (e.g., $Ri_b \sim O(100)$), so suppression of instabilities proportional to S_r only applies in the non-geostrophic limit.

A strength of the Sakai model is to interpret instabilities in the framework of wave resonance based on the physical wave coordinates (Sakai, 1989). For instance, Kelvin-Helmholtz instabilities are interpreted as the resonance of interacting gravity waves. In this study, we will only focus on the interactions between Rossby waves to interpret the suppression of baroclinic instabilities. The physical wave coordinates, then, only consist of the Rossby waves; since the Rossby wave coordinates are the Fourier basis (see Appendix C), the projection onto the physical wave coordinates is equivalent to conducting the Fourier transform (Pedlosky, 2013). The details of the Rossby wave resonance in the adapted Sakai model can be found in Appendix C. The resonance rate R^* in the adapted Sakai model is, then,

$$R^* = Imag[\, k^* U_0 \sqrt{\frac{(1-2\delta_r \epsilon_n^*)^2 - \epsilon_n^{*2}}{1-\epsilon_n^{*2}}}\,] \tag{2.8}$$

where $\epsilon_n = \frac{1}{2R_d^2(k^{*2}+l_n^{*2})+1}$ is the interaction coefficient, k^* is the dimensional along-slope wavenumber, and $l_n^* = \frac{n\pi}{2Y_{max}^*}$ $(n = 1, 2, 3, ...)$ is the dimensional across-slope wavenumber. If $\delta_r = 1$ (the flat-bottom case), Eq. (2.8) is reduced to $R^* = Imag[\, k^* U_0 \sqrt{1 - \frac{2}{R_d^2(k^{*2}+l_n^{*2})+1}}\,]$, which reproduces Eq. (28) in Sakai (1989). Fig. 2.5 shows the comparison between the non-zero $\hat{\sigma}_{i,max}$ (shown in Fig. 2.4) and the normalized resonance rate $Ri_b^{1/2} f^{-1} R^*$, where R^* is calculated by only considering the resonance of the lowest mode ($n = 1$) and using the k^* corresponding to the maximum growth rate. The resonance rate closely follows the growth rate, especially at high growth rates (presumably, the discrepancy at low growth rates is due to the only consideration of the resonance of the lowest mode). This implies that the maximum growth of instabilities is highly related to the resonance of the lowest mode of Rossby waves.

Basically, in the adapted Sakai model, the sloping bottom and surface modify the phase speed of Rossby waves and hence alter the Rossby wave resonance from the flat-bottom case. According

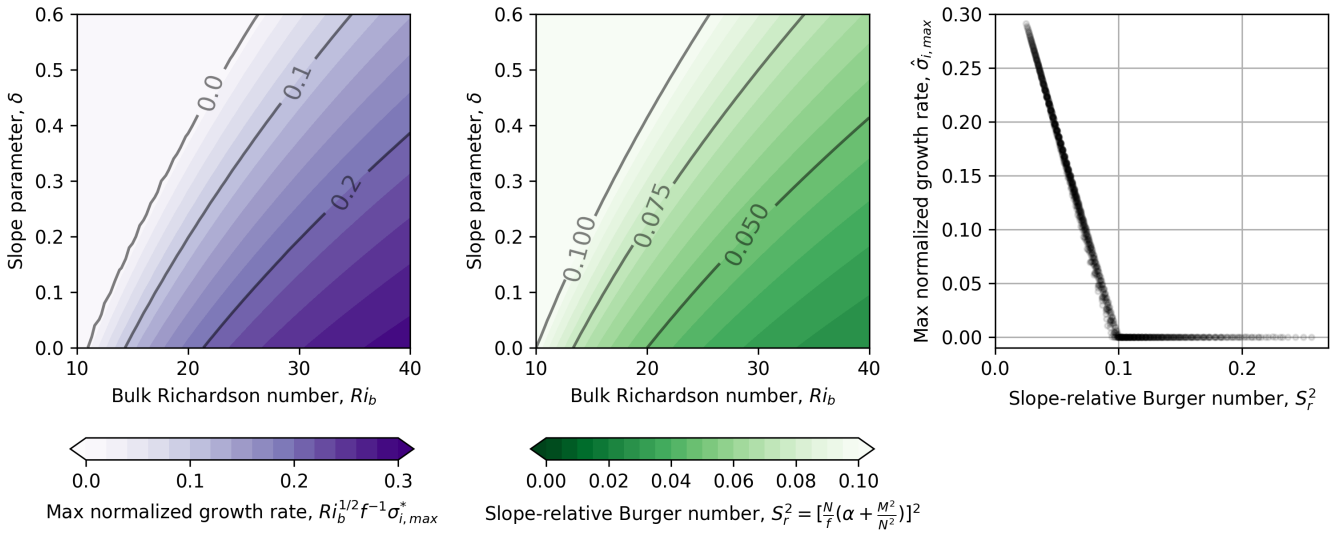

Figure 2.4: (left) Maximum normalized growth rate $\hat{\sigma}_{i,max}$ and (middle) slope-relative Burger number $S_r^2 = [(1+\delta)Ri_b^{-1/2}]^2$ as functions of bulk Richardson number $Ri_b = \frac{g'H_0}{2U_0^2}$ and slope parameter $\delta = \frac{\alpha g'}{2U_0 f}$ based on the adapted Sakai model. Comparison of S_r^2 and $\hat{\sigma}_{i,max}$ is shown in the right panel.

to Appendix C, the dimensionless form of the phase speed of the Rossby waves in both layers is

$$\begin{aligned}\sigma_1/k &= -\frac{2}{2(k^2+l_n^2)+1}S_r,\\ \sigma_2/k &= \frac{2}{2(k^2+l_n^2)+1}S_r.\end{aligned} \tag{2.9}$$

Where $\sigma_{1,2}$ are the dimensionless wave frequencies, k is the dimensionless along-slope wavenumber, and $l_n \equiv \frac{n\pi}{2Y_{max}} = \frac{n\pi}{2\Delta H}S_r$ $(n = 1, 2, 3, ...)$ is the dimensionless across-slope wavenumber. If only considering the resonance of the lowest mode $(n = 1)$ and using the k corresponding to the non-zero $\hat{\sigma}_{i,max}$, the dimensionless phase speed σ/k is a function of Ri_b and δ, which is shown in the left panel of Fig. 2.6. The correlation between σ/k and $Ri_b^m\delta_r^n$ is shown in the middle panel of Fig. 2.6. The highest correlation coefficients are at $m = -\frac{n}{2}$ where $S_r^n = [Ri_b^{-1/2}\delta_r]^n$ locates; it means that the phase speed of the Rossby waves is significantly proportional to the slope-relative Burger number S_r. Presumably, this is due to that S_r represents the gradient of potential vorticity, and larger gradient leads to the faster wave speed. Once the wave speed is increased by the sloping bathymetry, the Doppler-shifted frequencies of the waves would be altered from the resonant frequency in the corresponding flat-bottom case. Consequently, the wave resonance would be weaker, and hence the growth rate of instabilities would be smaller. The right panel of Fig. 2.6 shows that the resonance rate linearly decreases with the increasing S_r^2, and they are highly correlated $(r^2 = -0.99, p = 0.0)$. In sum, S_r controls the growth of instabilities by altering the Rossby wave resonance.

2.3.2 Suppression of Instabilities in the Continuously Stratified Model

The suppression of instabilities through the reduction of instability growth rate is also found in the adapted Stone model. Particularly, the suppression is significant when the regime shifts from QG to non-geostrophic. To demonstrate the suppression, the QG model is briefly reviewed here. In the QG model, the mean state consists of a density field with constant vertical and horizontal buoyancy gradients and a velocity field constrained by the thermal wind relation. By assuming that the Rossby number $Ro = \frac{U}{fL} \ll 1$ and Burger number $Bu = \frac{NH}{fL} \sim 1$ (leading to the Richardson

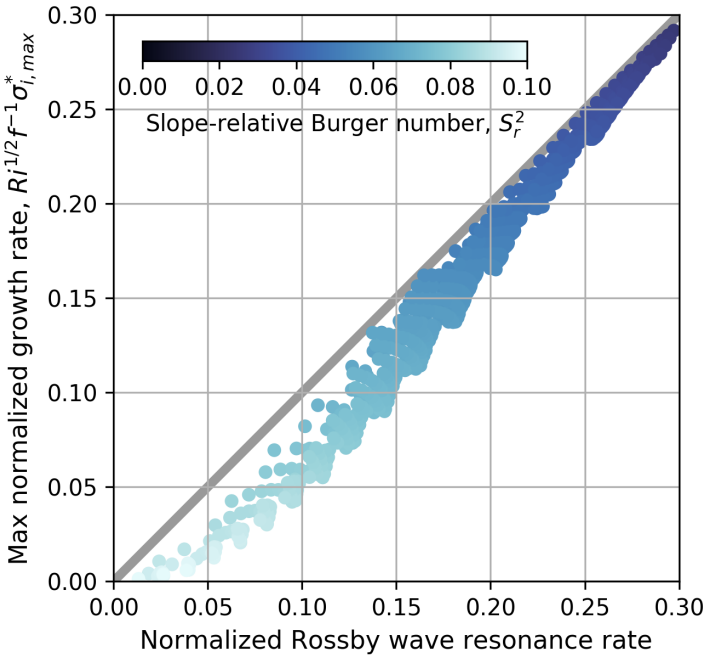

Figure 2.5: Comparison of the normalized Rossby wave resonance rate $Ri_b^{1/2} f^{-1} R^*$ and the non-zero maximum normalized growth rate $\hat{\sigma}_{i,max}$ (based on the adapted Sakai model) in the parameter space of $10 \leq Ri_b \leq 40$ and $0 \leq \delta \leq 0.6$. Color represents slope-relative Burger number S_r^2, and grey line is the 1:1 line.

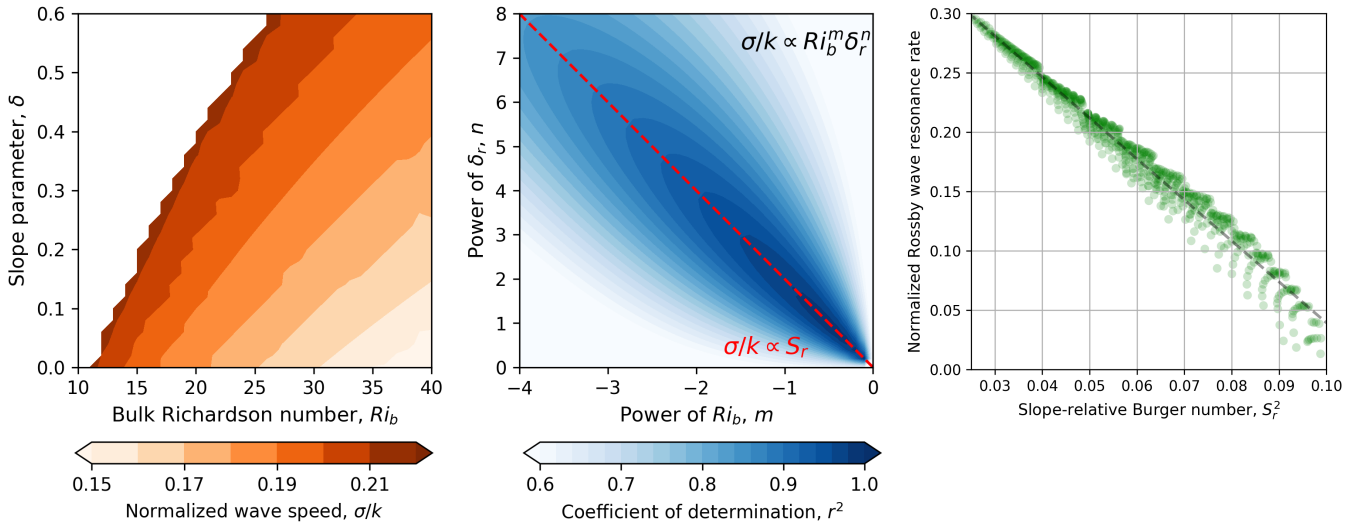

Figure 2.6: (left) Dimensionless Rossby wave speed σ/k as a function of bulk Richardson number $Ri_b = \frac{g'H_0}{2U_0^2}$ and slope parameter $\delta = \alpha N^2 M^{-2}$. (middle) Correlation coefficient between σ/k and $Ri_b^m \delta_r^n$ (using different powers of bulk Richardson number Ri_b and slope-relative parameter δ_r). The red dashed line marks $Ri_b^{-n/2}\delta_r^n$ representing slope-relative Burger number $S_r^n = [\delta_r Ri_b^{-1/2}]^n$. (right) Comparison of the slope-relative Burger number S_r^2 and the Rossby wave resonance rate. Grey dashed line is the linear regression ($r^2 = -0.99, p = 0.0$).

number $Ri = Bu^2 Ro^{-2} \gg 1$), the equations governing perturbations can be linearized and hence reduced to a single PDE about the QG potential vorticity. Then, the growth rate of the instabilities is analytically obtained by solving the associated eigenvalue problem; the normalized growth rate is, then,

$$\hat{\sigma}_i = \{[\frac{\hat{k}}{tanh(\hat{k})} - 1](1+\delta) - \frac{1}{4}[\frac{\delta}{tanh(\hat{k})} + \hat{k}]^2\}^{1/2}, \tag{2.10}$$

where $\hat{\sigma}_i = Ri^{1/2}\sigma_i^* f^{-1}$ is the normalized growth rate, $\hat{k} = k^* R_d$ is the normalized wavenumber, and δ is the slope parameter. Fig. 2.2 shows $\hat{\sigma}_i$ in the QG model and the adapted Stone model. The adapted Stone model exhibits a significant reduction of the tail and predicts lower growth rates than the QG model. For instance, the tail enclosed by the contours of 0.2 is significantly smaller in the adapted stone model than the QG model.

Maximum growth rates predicted by the QG and adapted stone models have different dependencies on the Richardson number Ri. The maximum normalized growth rate, $\hat{\sigma}_{i,max}$, is defined as the maximum of the normalized growth rate across all wavenumbers, $\hat{k}$, for a given Ri and δ. The maximum normalized growth rate, $\hat{\sigma}_{i,max}$, for the adapted stone model is denoted as $\hat{\sigma}_{NG}$, $\hat{\sigma}_{QG}$ for the QG model. Fig. 2.7 shows the $\hat{\sigma}_{NG}$ and $\hat{\sigma}_{QG}$ in the parameter space of Richardson number, Ri, and slope parameter, δ. Here we implicitly associate QG theory to high Ri conditions, because it is unknown how well QG theory describes flow at low Ri conditions. The QG maximum growth rate, $\hat{\sigma}_{QG}$, decreases with δ, but does not vary with Ri, since the QG normalized growth rate $\hat{\sigma}_i$ is independent of Ri (see Eq. (2.10)). In contrast, $\hat{\sigma}_{NG}$ exhibits a clear dependency on Ri, decreasing as Ri decreases.

A dimensionless number is also sought for indicating the suppression of instabilities in the adapted Stone model. We will seek the form of the dimensionless number according to the dimensionless numbers controlling the instability growth in the QG limit (Blumsack and Gierasch, 1972) and the non-geostrophic limit with flat bathymetry (Stone, 1970). In other words, the new number should be able to reduce to the numbers in the QG limit (as $Ri \to \infty$) and the non-geostrophic limit with flat bathymetry (as $\delta \to 0$).

Based on the discussion of the adapted Sakai model, above, S_r and δ_r are obvious choices

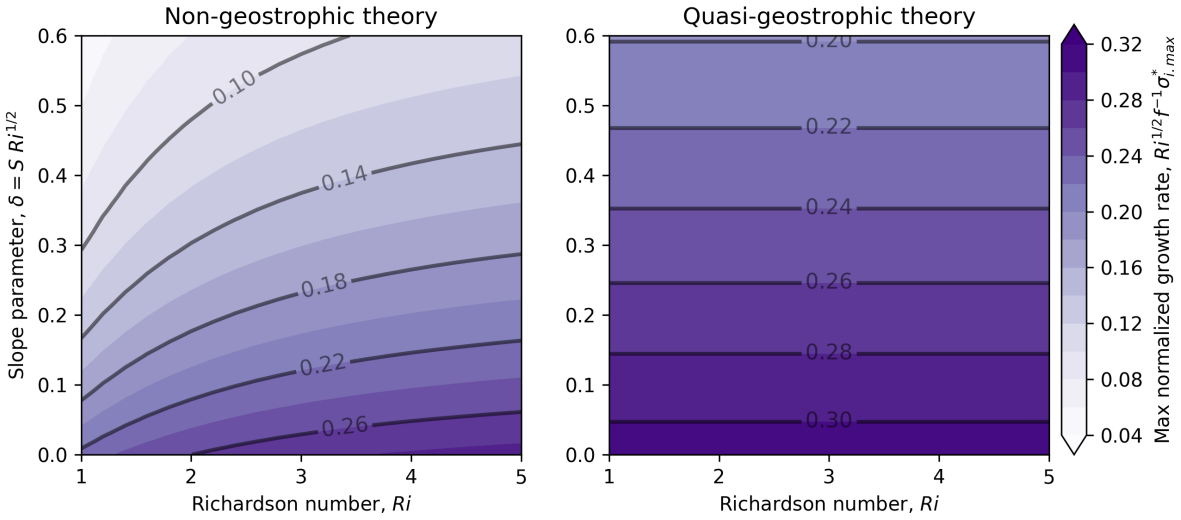

Figure 2.7: Maximum normalized growth rates $\hat{\sigma}_{NG}$ (left) and $\hat{\sigma}_{QG}$ (right) as functions of Richardson number $Ri = N^2 f^2 M^{-4}$ and slope parameter $\delta = \alpha N^2 M^{-2}$ based on the adapted Stone model and the QG model.

to consider. The following discussion will demonstrate the dimensionless numbers δ_r^{-1} and $(1 + Ri^{-1})^{-1/2}$ control the instability growth in the QG limit and non-geostrophic limit with flat bathymetry, respectively. First, as demonstrated in Pedlosky (2016), the slope-relative parameter δ_r is the only dimensionless number appearing at the bottom boundary condition of the Eady problem (Pedlosky, 2016, Eq.(5b)); it involves the vertical shear of the mean flow that is supplemented by the topographic production of vertical vorticity by the perturbed across-slope flow. Fig. 2.8 (left) shows the comparison between the maximum normalized QG growth rate $\hat{\sigma}_{QG}$ and δ_r^{-1}; δ_r^{-1} has a robust relation with $\hat{\sigma}_{QG}$ ($r^2 = 0.997, p = 3 \times 10^{-66}$) – δ_r^{-1} is the controlling number in the QG limit. Second, as demonstrated in Fox-Kemper et al. (2008), the maximum normalized non-geostrophic growth rate in the flat-bottom case is a linear function of $(1 + Ri^{-1})^{-1/2}$,

$$\hat{\sigma}_{NG}^{Asym} = \sqrt{\frac{5}{54}}(1 + Ri^{-1})^{-1/2}, \tag{2.11}$$

which is obtained based on the asymptotic solution of Stone (1970). Fig. 2.8 (right) shows the comparison between the numerical $\hat{\sigma}_{NG}|_{\delta=0}$ and $(1+Ri^{-1})^{-1/2}$; $(1+Ri^{-1})^{-1/2}$ has a robust relation

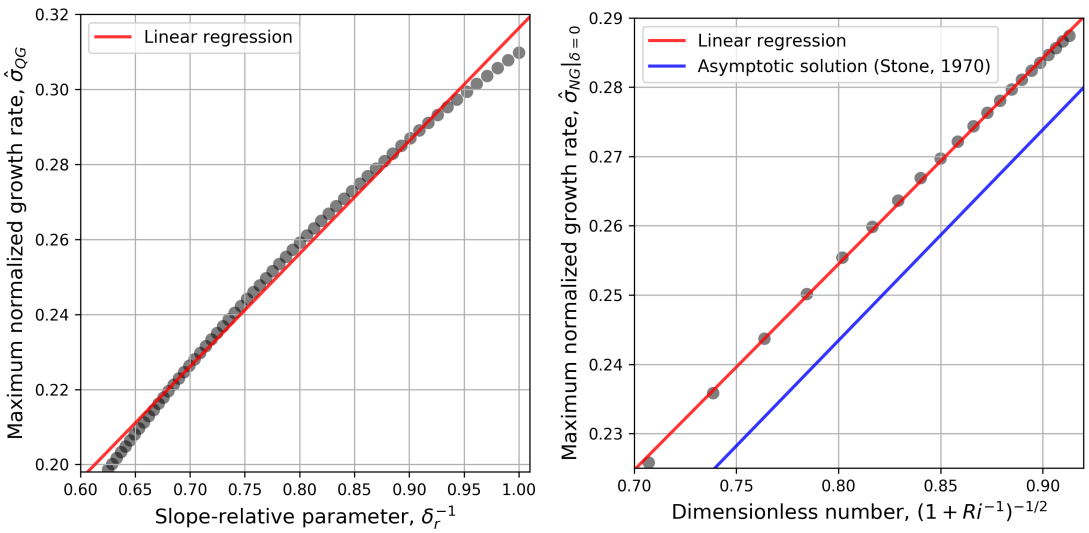

Figure 2.8: (left) Comparison of the slope-relative parameter δ_r^{-1} and the maximum normalized QG growth rate $\hat{\sigma}_{QG}$. Red line is the linear regression ($r^2 = 0.997$, $p = 3 \times 10^{-66}$). (right) Comparison of the dimensionless number $(1+Ri^{-1})^{-1/2}$ and the maximum normalized non-geostrophic growth rate in the flat bottom case $\hat{\sigma}_{NG}|_{\delta=0}$. Red line is the linear regression ($r^2 = 1.000$, $p = 2 \times 10^{-32}$). Blue line is the analytical relation between $(1 + Ri^{-1})^{-1/2}$ and $\hat{\sigma}_{NG}|_{\delta=0}$ based on the asymptotic solution of Stone (1970).

with $\hat{\sigma}_{NG}|_{\delta=0}$ ($r^2 = 1.000, p = 2 \times 10^{-32}$). The analytical $\hat{\sigma}_{NG}^{Asym}$ as a function of $(1+Ri^{-1})^{-1/2}$ is shown in Fig. 2.8 (right); the offset between the numerical $\hat{\sigma}_{NG}|_{\delta=0}$ and the analytical $\hat{\sigma}_{NG}^{Asym}$ is due to the underestimate of the asymptotic solution of Stone (1970). Both the analytical and numerical solutions suggest that $(1 + Ri^{-1})^{-1/2}$ is the controlling number in the non-geostrophic limit with flat bathymetry. Recalling the inhibiting effect of the slope-relative Burger number $S_r = \delta_r Ri^{-1/2}$ in the non-geostrophic limit, the dimensionless number $(1+Ri^{-1})^{-1/2}$ could be the representation of the $(1 + S_r^2)^{-1/2}$ in the flat-bottom case because of $(1 + S_r^2)^{-1/2}|_{\delta=0} = (1 + Ri^{-1})^{-1/2}$.

The multiplication of δ_r^{-1} (representing the QG effect) and $(1 + S_r^2)^{-1/2}$ (representing the non-geostrophic effect) would be a physically intuitive form of the dimensionless number in the adapted Stone model, because it can simply reduce to δ_r^{-1} as $Ri \to \infty$ (the QG limit) and $(1+Ri^{-1})^{-1/2}$ as $\delta \to 0$ (the non-geostrophic limit with flat bathymetry). The dimensionless number $\delta_r^{-1}(1+S_r^2)^{-1/2}$ in the $Ri - \delta$ space is shown in Fig. 2.9, which has a similar distribution as the $\hat{\sigma}_{NG}$ (shown in Fig. 2.7 left). Fig. 2.9 also shows the comparison between $\delta_r^{-1}(1 + S_r^2)^{-1/2}$ and $\hat{\sigma}_{NG}$; $\hat{\sigma}_{NG}$ is

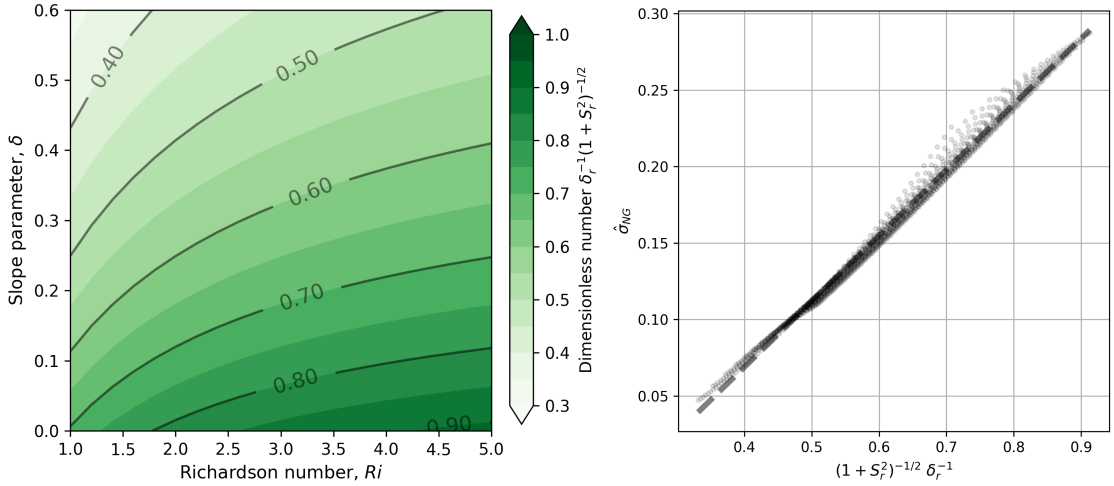

Figure 2.9: (left) The dimensionless number $\delta_r^{-1}(1+S_r^2)^{-1/2}$ as a function of Richardson number Ri and slope parameter δ, where $S_r = \frac{N}{f}(\alpha + M^2N^{-2})$ is slope-relative Burger number and $\delta_r = (\alpha + M^2N^{-2})N^2M^{-2}$ is slope-relative parameter. (right) Comparison of the dimensionless number $\delta_r^{-1}(1+S_r^2)^{-1/2}$ and the maximum normalized non-geostrophic growth rate $\hat{\sigma}_{NG}$. Red line is the linear regression, $y = 0.430x - 0.103$, with $r^2 = 0.997$ and $p = 0.0$.

highly related to $\delta_r^{-1}(1+S_r^2)^{-1/2}$ indicated by a robust linear regression ($r^2 = 0.997$ and $p = 0.0$). The selection of this dimensionless number is empirical but with strong physical meaning - the modification of $(1+S_r^2)^{-1/2}$ on δ_r^{-1} stands for the suppression of instabilities occurring when the regime shifts from QG to non-geostrophic (as shown in Fig. 2.7). In other words, the instabilities are suppressed with increasing slope-relative Burger number S_r.

2.4 Discussion

The suppression of instabilities demonstrated in Section 2.3 seems to be related to the fact that baroclinic instabilities are seldom observed in coastal fronts over sloping topography, such as river plumes, even when strong lateral buoyancy gradients are present. In this section, we will discuss the applicability of the adapted Stone model to the baroclinic instabilities in coastal buoyancy-driven flow over sloping bathymetry.

2.4.1 Scale Analysis

The adapted Stone model is intrinsically applicable to baroclinic instabilities in a bottom boundary layer (Wenegrat et al., 2018), where both the bottom and surface can be assumed to be tilted and parallel, while it may not seem directly applicable to surface-intensified baroclinic instabilities that are usually associated with flat surfaces. However, the following scale analysis demonstrates that the adapted Stone model can be used as an approximation of the flat surface case so long as the slope Burger number $S \lesssim O(10^{-1})$ and the horizontal slope Burger number $S_H \lesssim O(10^{-1})$. The scaling relations in Appendix B will be used in the scale analysis. In the rotated coordinates, a flat surface in the dimensional form can be written as $z^* = H + \alpha(y^* - y_c^*)$ is the depth, H is the depth at the center of the front y_c^*, and α is a constant bottom slope. Considering the motions within the length scale of baroclinic instabilities that is on the order of the Rossby deformation radius $R_d = \frac{NH}{f}$ (Eady, 1949; Stone, 1966, 1970), the dimensional flat surface can be scaled as

$$z = \frac{z^*}{H} \sim 1 \pm \alpha \frac{Rd}{H} = -1 \pm S, \tag{2.12}$$

where $S = \frac{N}{f}\alpha$ is the slope Burger number. For the situations characterized by $\delta \sim O(10^{-1})$ and $Ri \sim O(1)$ (which are the cases in this study), the slope Burger number $S = \delta Ri^{-1/2}$ is on the order of $O(10^{-1})$ so that the uniform fluid depth $z = 1$ will be a reasonable assumption. In other words, if $S \sim O(10^{-1})$, motions with lateral displacements $O(Rd)$ will span a depth range of $H \pm 0.1H$, and hence the uniform fluid depth will be a first-order approximation.

With the uniform fluid depth approximation, the rigid-lid boundary condition at the flat surface in the rotated coordinates is

$$w^*|_{z^*=H} = \alpha v^* \ . \tag{2.13}$$

The dimensionless form is, then,

$$w|_{z=1} = \alpha U (Hf)^{-1} v = \alpha M^2 f^{-2} v = S_H v, \tag{2.14}$$

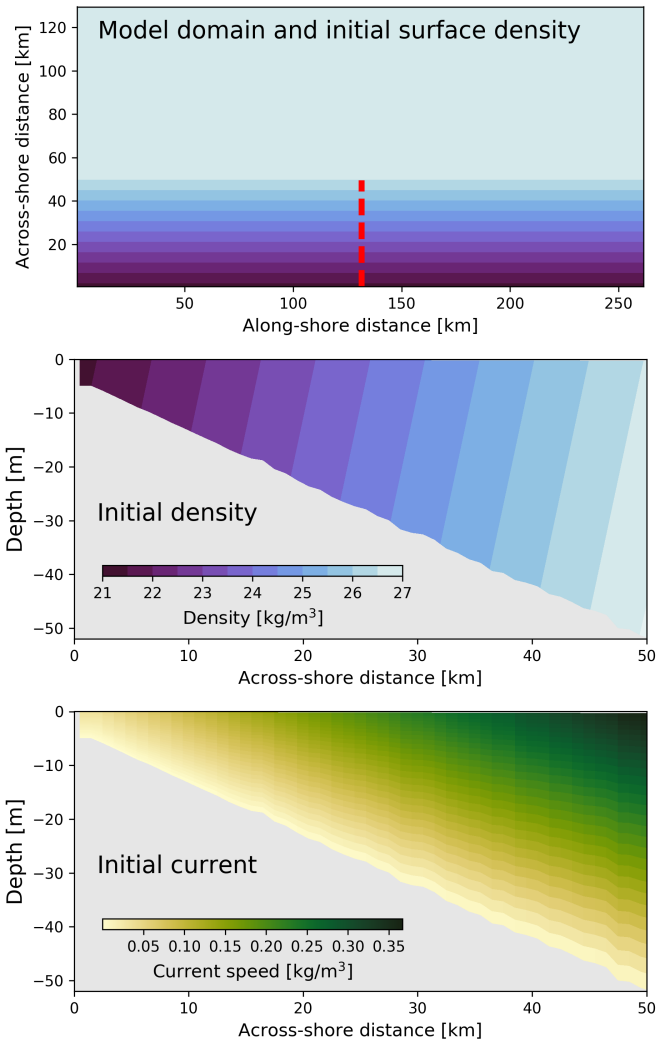

Figure 2.10: (top) Model domain and the initial surface density. (middle and bottom) Cross sections of the initial density and currents (along the red dashed line in the top panel).

where $S_H = \alpha M^2 f^{-2}$ is the horizontal slope Burger number (Hetland, 2017). For the situations characterized by $\delta \sim O(10^{-1})$ and $Ri \sim O(1)$ (which are the cases in this study), the horizontal slope Burger number $S = \delta Ri^{-1}$ is on the order of $O(10^{-1})$ so that the no-flow boundary condition $w|_{z=1} = 0$ will be an acceptable approximation. In summary, if a front over a sloping bottom satisfied $S \lesssim O(10^{-1})$ and $S \lesssim O(10^{-1})$, the assumptions of the uniform fluid depth and the no-flow boundary condition will be first-order accurate, and hence the adapted Stone model can be used to represent the surface-intensified baroclinic instabilities formed within the front.

2.4.2 Numerical Simulations

A series of existing idealized numerical simulations, first analyzed by Hetland (2017), are used to examine the feasibility of the adapted Stone model. The idealized model domain is a 260 km (along-slope) $\times$ 128 km (across-slope) continental shelf with the uniform bathymetric slope $\alpha = 10^{-3}$ across all simulations. The depth increases from 5 m onshore to 133 m offshore. The model grid has 1-km uniform horizontal resolution and 30 layers in the vertical direction. The boundary conditions are periodic along-slope, open (with a sponge layer) offshore, and closed (no-slip) at the coast. $k - \epsilon$ turbulence closure scheme is used to calculate the vertical mixing, and bottom friction is defined using a specified bottom roughness and a log-layer approximation. The model is unforced and run as an initial-value problem. The initial density field is a coastal buoyant front with a constant vertical stratification N^2 over the whole shelf and a constant lateral buoyancy gradient M^2 within the offshore distance of $W = 50$ km. The initial current field is configured in the thermal wind balance with the density field. The initial density and current fields of the base case ($Ri = 2.0$ and $\delta = 0.1$) are shown in Fig. 2.10. Initial fields are varied among simulations to cover a range of situations of instability formation.

The idealized simulations were configured in the parameter space of the Richardson number Ri and the slope parameter δ, and all the simulations used in this study are listed in Tab. 2.1. All the simulations were run with same stratification N^2 and same bottom slope α, but with different lateral buoyancy gradients M^2 and Coriolis parameters f that are determined by each combination of Ri and δ. Note that the simulations listed in Tab.1 are part of the simulations conducted in Hetland (2017); simulations with the Richardson number $Ri = 1$ or $Ri = 10$ or the slope parameter $\delta > 0.5$ or the horizontal slope Burger number $S_H > 0.2$ were excluded. $Ri = 1$ is around the boundary between baroclinic instabilities and symmetric instabilities (Haine and Marshall, 1998; Boccaletti et al., 2007), so the simulations with $Ri = 1$ are excluded to ensure only baroclinic instabilities can form. The simulations with $Ri = 10$ are excluded to ensure the non-geostrophic regime, and to minimize the influence of bottom friction in these simulations with long instability growth rates. The instability formations in the simulations with $\delta > 0.5$ are excluded because they are

Table 2.1: Simulations in the parameter space of Ri and δ. All simulations were run with $N^2 = 1.00 \times 10^{-4}\ s^{-1}$ and $\alpha = 1.00 \times 10^{-3}$. Slope Burger number is determined by $S = \delta \mathrm{Ri}^{-1/2}$, Coriolis parameter is then determined by $f = N\alpha/S$, and horizontal buoyancy gradient is lastly determined by $M^2 = Nf\mathrm{Ri}^{-1/2}$. σ^*_{NG} and σ^*_{QG} are the maximum dimensional growth rates in units of day^{-1}, based on the adapted stone model and QG model, respectively. σ^*_R is the regressed dimensional growth rate in units of day^{-1}. T_{reg} is the time scale (in units of days) to truncate a EKE series for the regression.

M^2	f	Ri	δ	S	S_H	σ^*_{NG}	σ^*_{QG}	σ^*_R	T_{reg}
1.00e-06	1.41e-04	2.0	0.10	0.07	0.05	1.817	2.505	1.727	4.6
1.00e-06	1.73e-04	3.0	0.10	0.06	0.03	1.971	2.505	1.939	4.4
1.00e-06	2.24e-04	5.0	0.10	0.04	0.02	2.108	2.505	2.264	3.9
7.07e-07	1.00e-04	2.0	0.14	0.10	0.07	1.182	1.720	0.716	8.5
5.77e-07	1.00e-04	3.0	0.17	0.10	0.06	0.996	1.372	0.680	9.6
5.00e-07	7.07e-05	2.0	0.20	0.14	0.10	0.742	1.166	0.391	14.4
5.00e-07	8.66e-05	3.0	0.20	0.12	0.07	0.823	1.166	0.507	12.9
5.00e-07	1.12e-04	5.0	0.20	0.09	0.04	0.896	1.166	0.699	10.6
4.47e-07	1.00e-04	5.0	0.22	0.10	0.04	0.770	1.024	0.481	13.5
3.54e-07	5.00e-05	2.0	0.28	0.20	0.14	0.445	0.776	0.275	25.1
3.33e-07	4.71e-05	2.0	0.30	0.21	0.15	0.405	0.720	0.137	39.9
3.33e-07	5.77e-05	3.0	0.30	0.17	0.10	0.459	0.720	0.235	29.9
3.33e-07	7.45e-05	5.0	0.30	0.13	0.06	0.507	0.720	0.334	23.5
2.89e-07	5.00e-05	3.0	0.35	0.20	0.12	0.367	0.604	0.208	33.9
2.24e-07	5.00e-05	5.0	0.45	0.20	0.09	0.270	0.433	0.229	45.8
2.00e-07	4.47e-05	5.0	0.50	0.22	0.10	0.222	0.371	0.200	62.1

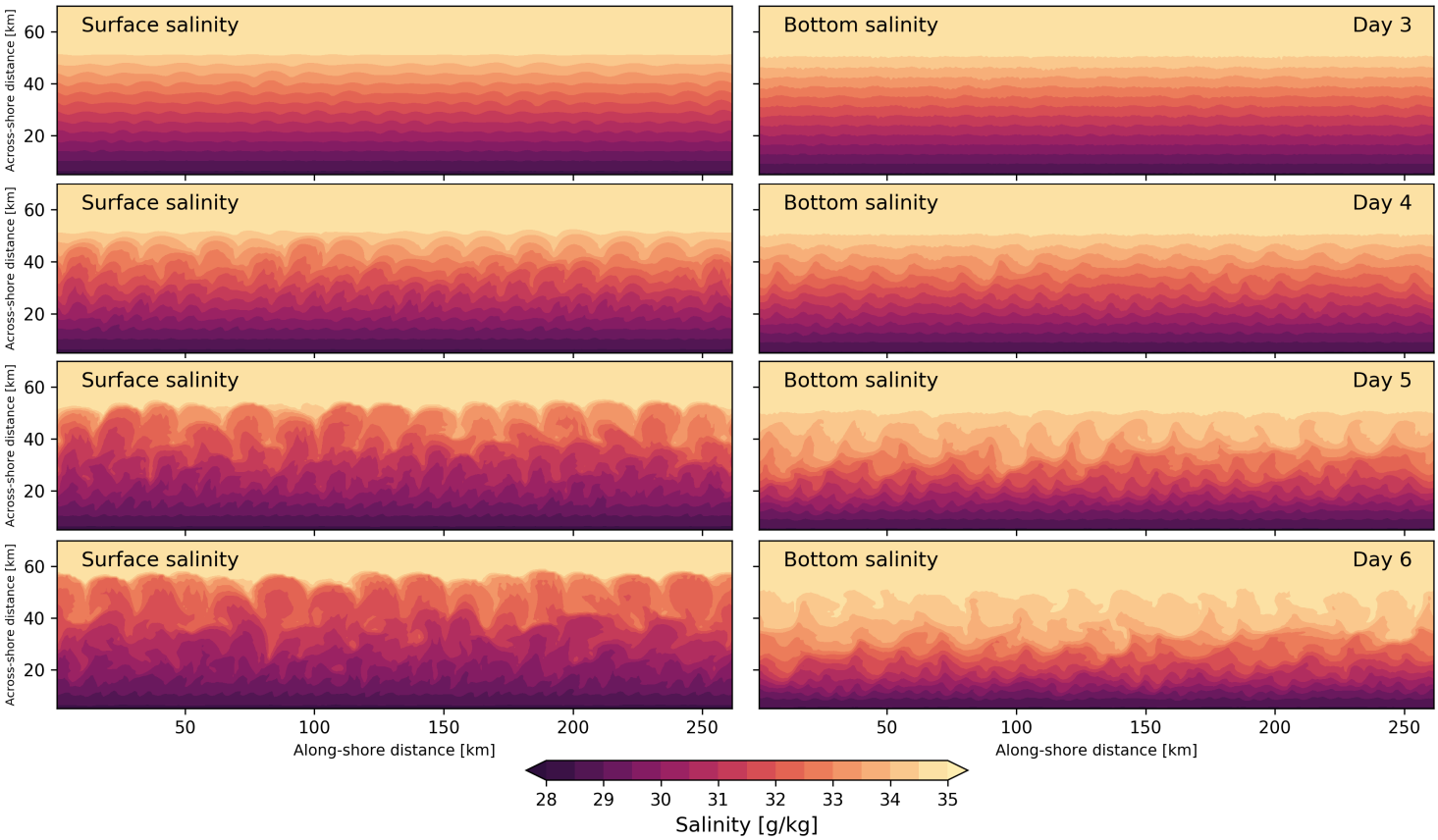

Figure 2.11: Development of instabilities of the base case ($Ri = 2.0$ and $\delta = 0.1$) at the surface (left columns) and bottom (right columns).

generally weak and also strongly influenced by bottom friction. The simulations with $S_H > 0.2$ are excluded to ensure $S_H \lesssim O(10^{-1})$ and $S \lesssim O(10^{-1})$ so that the adapted Stone can be applied to the flat-surface case. One example of the development of instabilities in the base run is shown in Fig. 2.11.

The growth rate of instabilities is estimated in each simulation and then compared to the QG model and the adapted stone model. Note that the spatial scale of the instabilities increases in the offshore direction (see Fig. 2.11) because of the increase of the deformation radius $Rd = \frac{NH}{f}$. We only focus on the growth of the largest instabilities at ~ 50 km offshore with the depth $H \sim 50$ m, because they are the most energetic and dispersive components (Thyng and Hetland, 2017, 2018). This also makes the comparison between the numerical and theoretical results feasible: the theo-

retical configuration has the fixed depth scale and infinite front, while the numerical configuration has the varying depth scale and finite front; the comparison is valid only if the depth scale and front region are unified in the numerical and theoretical configurations.

Eddy kinetic energy (EKE) is used to quantify growth rates of instabilities. Given that the domain is periodic in the along-slope direction, the velocity field associated with the instability eddies is calculated by subtracting the along-slope mean velocity from the original velocity field. So, EKE is dominated by the largest eddies. Then, the EKE can be determined by integrating the kinetic energy of the eddy flow field over the whole domain. Last, the EKE is normalized by the initial domain-integrated mean kinetic energy $MKE_{Initial}$. Fig. 2.12a shows the normalized EKE, $\frac{EKE}{MKE_{Initial}}$, of all the simulations listed in Tab. 2.1.

The EKE in each case appears to increase exponentially from the start (Fig. 2.12a), but eventually the rapid increase is retarded by friction. In order to isolate our results from these frictional effects and compare our results more directly with the theories that do not consider the influence of friction, we truncate EKE time series where it reaches the half of the maximum, removing the later part that is potentially influenced by friction. The truncated timescale for each simulation is listed in Tab.1, and the truncated EKE time series are shown in Fig. 2.12b. We take the base case ($Ri = 2.0, \delta = 0.1$) as an example to show the comparison between the simulated growth rate and the theoretical predictions. The truncated EKE time series of the base run is shown in Fig. 2.12c, and the best exponential function to fit it has a growth rate of $1.73\ day^{-1}$ ($r^2 = 0.996$). On the other hand, based on the adapted stone and QG models, we can calculate the maximum dimensional growth rates for the base case, which are $\sigma^*_{NG} = 1.82\ day^{-1}$ and $\sigma^*_{QG} = 2.50\ day^{-1}$. The non-geostrophic and QG predictions as exponential functions with growth rates of σ^*_{NG} and σ^*_{QG} are shown in Fig2.12c; as expected from the growth rate estimates, the non-geostrophic prediction tracks the simulated increase in EKE closer than the QG prediction.

A regressed estimate of simulated EKE growth rate, σ^*_R, is calculated for each simulation listed in Tab.1, in order to compare with σ^*_{NG} and σ^*_{QG}. The calculated values of σ^*_R, σ^*_{NG}, and σ^*_{QG} for each simulation are listed in Tab.1. Fig. 2.13a and 2.13b show the comparison between the

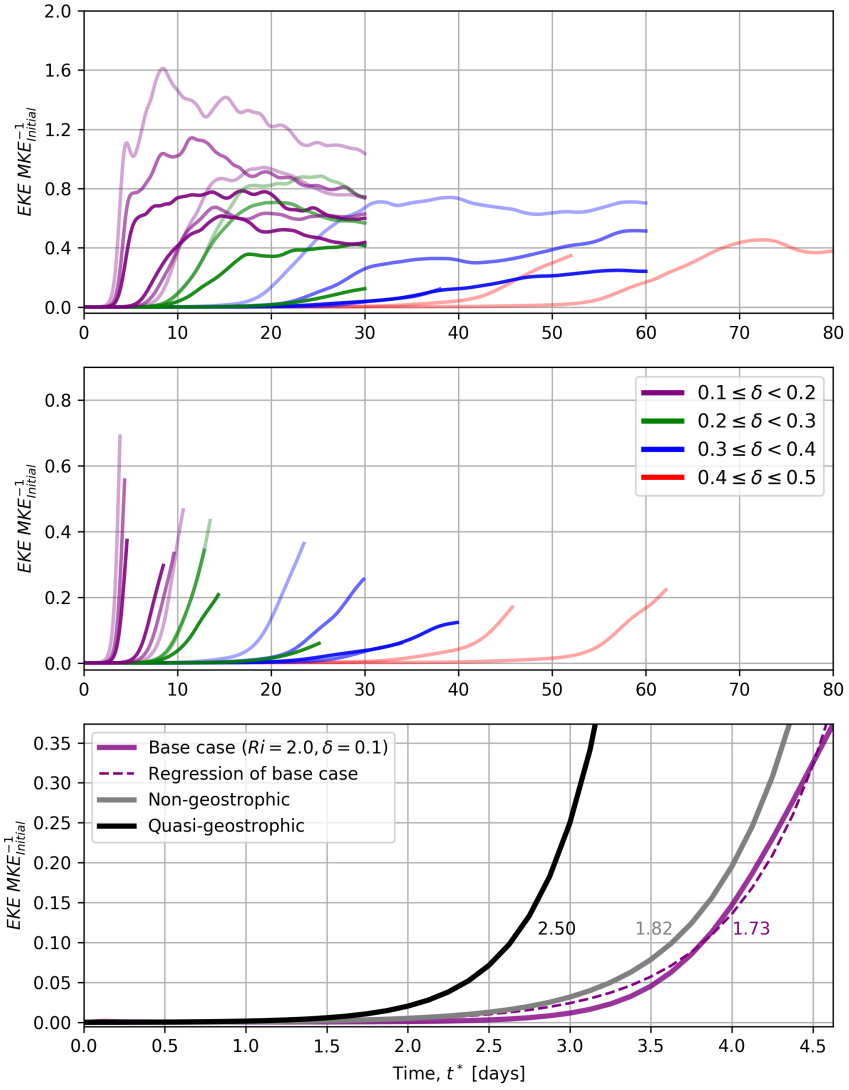

Figure 2.12: (a) Normalized EKE time series of the simulations of Tab.1. (b) Truncated normalized EKE time series. Each series is truncated at where the EKE reaches 50% of its maximum. Colors of the lines denote δ, and darker colors represent lower Ri. (c) Normalized EKE time series of the base case ($\mathrm{Ri} = 2.0, \delta = 0.1$) is compared to the theoretical estimates. The best exponential function fitting the base case has a growth rate of 1.73 day^{-1} ($r^2 = 0.996$), and the theoretical estimates are 1.82 day^{-1} (non-geostrophic) and 2.50 day^{-1} (QG).

regressed growth rates and the theoretical predictions. We can see that σ^*_{NG} better follow σ^*_R than σ^*_{QG}. Two-sided T test is conducted to test if the calculated and predicted growth rates are statistically equivalent. The two-tailed p-value for the non-geostrophic theory comparison is $p = 0.42$, and for the QG theory $p = 0.04$. Thus, if based on the p-value threshold of 5%, we cannot reject the null hypothesis in the test for the non-geostrophic theory, indicating the calculated and predicted growth rate distributions are indistinguishable. However, we can reject the null hypothesis in the test for the QG theory; the calculated and predicted distributions are distinct, as apparent from the offset from the 1:1 line in Fig 2.13b. Moreover, Fig. 2.13c and 2.13d show the distribution of growth rate errors in the $Ri - \delta$ space. Compared to the adapted Stone model, the QG model has higher growth rate errors, particularly on the low Richardson number cases ($Ri = 2.0 \; and \; 3.0$); this implies that the QG theory is not able to accurately describe the development of the submesoscale baroclinic instability eddies under energetic flow situations. However, under the conditions of $S_H \lesssim O(10^{-1})$ and $S \lesssim O(10^{-1})$, the adapted Stone model accurately predicts the growth rate of the instabilities in the energetic flow situations. Consequently, the numerical simulations complement the scale analysis in Section 2.4.1 and validate the applicability (under certain conditions) of the adapted Stone model to the flat-surface situations.

2.5 Conclusions

Layered and continuously stratified models of non-geostrophic baroclinic instability over sloping topography are explored in the buoyant flow regime. The primary finding of this study is that non-geostrophic baroclinic instabilities ($Ri \sim 1, Ro \sim 1$) are suppressed in terms of a reduced instability growth rate compared to QG baroclinic instabilities ($Ri \gg 1, Ro \ll 1$). This finding is consistent with the fact that baroclinic instabilities are seldom observed in energetic fronts in the coastal ocean, such as buoyancy-driven coastal currents associated with river plumes. A new parameter, the slope-relative Burger number $S_r = \frac{N}{f}(\alpha + \frac{M^2}{N^2})$ is an important dimensionless parameter for predicting the suppression of instabilities in the non-geostrophic limit. Both the layered model (i.e., the adapted Sakai model) and the continuously stratified model (i.e., the adapted Stone model) show that the growth of instabilities is inhibited with increasing S_r.

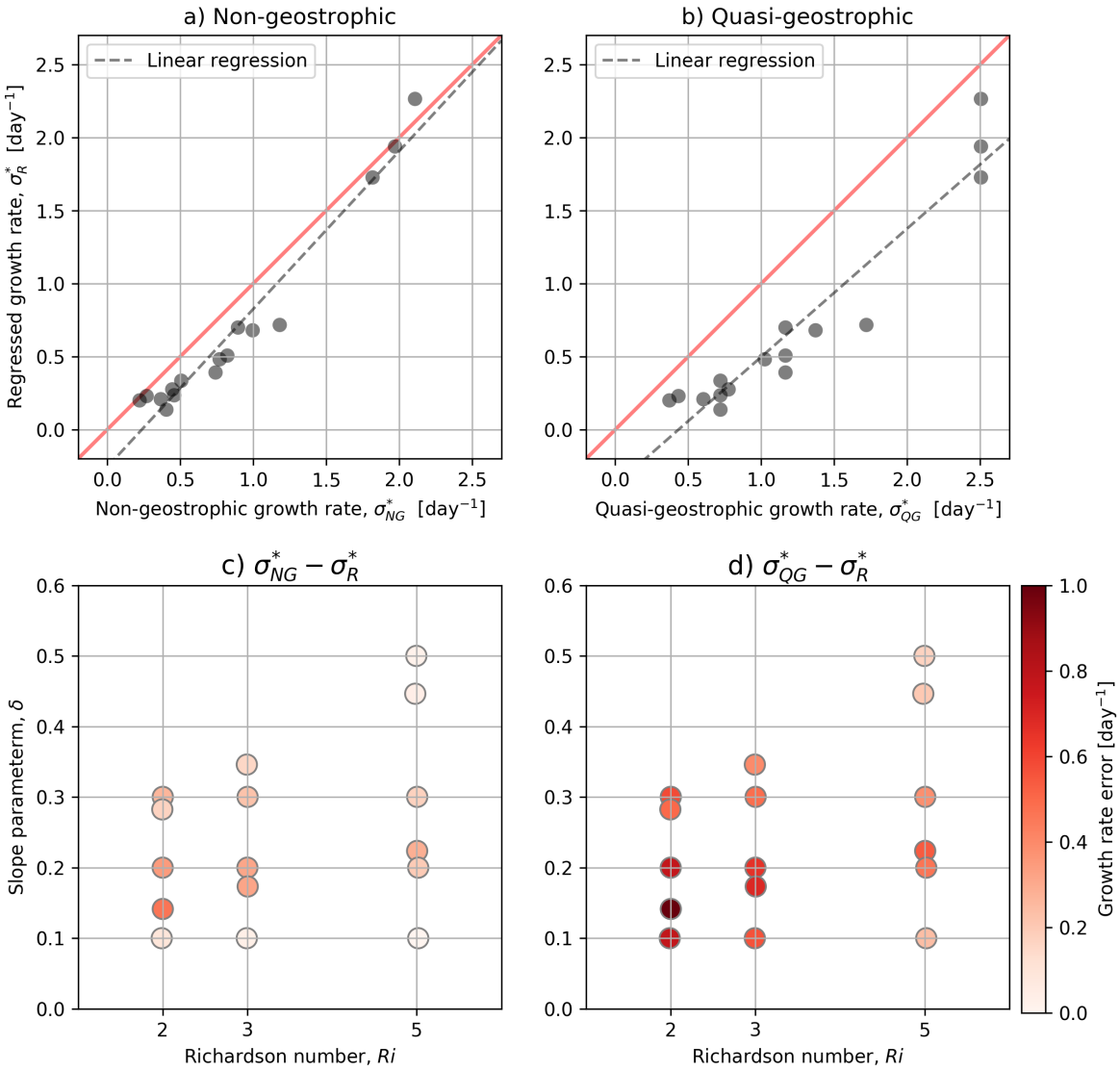

Figure 2.13: Regressed growth rates σ_R^* versus maximum dimensional (a) non-geostrophic growth rates σ_{NG}^* and (b) QG growth rates σ_{QG}^* for the simulations in Tab. 1. Dashed grey lines are the linear regressions. Growth rate errors of the (c) non-geostrophic and (d) QG theories.

The physical mechanism behind S_r is explored based on the wave resonance theory (Sakai, 1989). In the physical wave coordinates consisting of the Rossby waves, baroclinic instabilities are interpreted as the Rossby wave resonance; supported by the adapted Sakai model, the maximum normalized growth rate of instabilities is found to be nearly 1:1 to the resonance rate of the Rossby waves. Since S_r represents the gradient of potential vorticity supplemented by topographic effect, it modifies the phase speed of the Rossby waves, alters the wave resonance, and hence influences the growth of instabilities.

One limitation of the adapted Stone model is the sloping-surface assumption. Idealized numerical simulations of coastal buoyancy-driven flow are used to test the feasibility of the adapted Stone model in flat-surface situations. The comparison of the numerical results and theoretical predictions indicates that the limitation is not prohibitive if the slope Burger number $S = \frac{N}{f}\alpha \lesssim O(10^{-1})$ and the horizontal slope Burger number $S_H = \frac{M^2}{f^2}\alpha \lesssim O(10^{-1})$, which complements the scale analysis. The results also show that the QG model (Blumsack and Gierasch, 1972) can not accurately describe the growth of the submesoscale baroclinic instabilities especially when the flow is energetic (low Ri), which was not previously explained (Hetland, 2017). The numerical simulations validate the feasibility of the adapted Stone model in the flat-surface situations, and hence the inhibiting mechanism provided by the non-geostrophic theories can be used to interpret the suppression of instabilities in buoyancy-driven flow of coastal zones.

2.6 Acknowledgments

This chapter is based on an article submitted to the Journal of Physical Oceanography co-authored by Professor Robert Hetland. The support of Dr. Jacob Wenegrat and Professor Leif Thomas at Stanford University, grant 18-132-000-A673 from Texas General Land Office, grant 2018SP-S-Qu-GIA from Texas Sea Grant, and a scholarship from China Scholarship Council is gratefully acknowledged.

3. NEAR-INERTIAL WAVES IN A BAROCLINIC VORTEX

3.1 Introduction

NIWs dominate oceanic kinetic energy at the frequencies near the local Coriolis parameter. NIWs generated at the surface can propagate downward, transfer kinetic energy to the internal waves with higher frequencies, and trigger the diapycnal mixing in the ocean interior via wave breaking (Ferrari and Wunsch, 2009). In the open ocean, the energy input to NIWs from the winds is most intense under the mid-latitude storm tracks where large-scale ocean fronts, such as the Kuroshio Current, Gulf Stream, and Antarctic Circumpolar Current, are found (Chaigneau et al., 2008; Simmons and Alford, 2012). Because of the correspondence between NIWs and strong oceanic fronts, it has been hypothesized that the NIW-mean flow interactions play an important role in damping the large-scale circulation and energizing the internal wave continuum and hence could be important for closing the kinetic energy budget for both types of flows (Polzin and Lvov, 2011; Thomas, 2012; Nagai et al., 2015; Wagner and Young, 2016; Thomas, 2017).

An ocean front can significantly modify the allowable frequency and propagation properties of a NIW. Most of the previous studies focused on the modifications of NIWs at straight, jet-like fronts; the results show that, at the front with anti-cyclonic vorticity, subinertial waves can exist, be trapped, transfer the wave kinetic energy to small-scale turbulence, and hence enhance the interior mixing (Mooers, 1975; Kunze, 1985; Kunze et al., 1995; Whitt and Thomas, 2013; Thomas, 2017; Whitt et al., 2018). However, only a few have focused on curved, vortex-like fronts. Kunze and Boss (1998) constructed a model to explain the intense inertial motions observed within a vortex cap over the Fieberling Seamount, but the model is barotropic. Joyce et al. (2013) included the effects of a baroclinic vortex in the Richardson number and generalized the vertical vorticity dependence to explain an observed near-inertial mode in a Gulf Stream warm-core ring. Beyond that, a systematic, theoretical framework of the modifications of NIWs in a baroclinic vortex has yet to be well established.

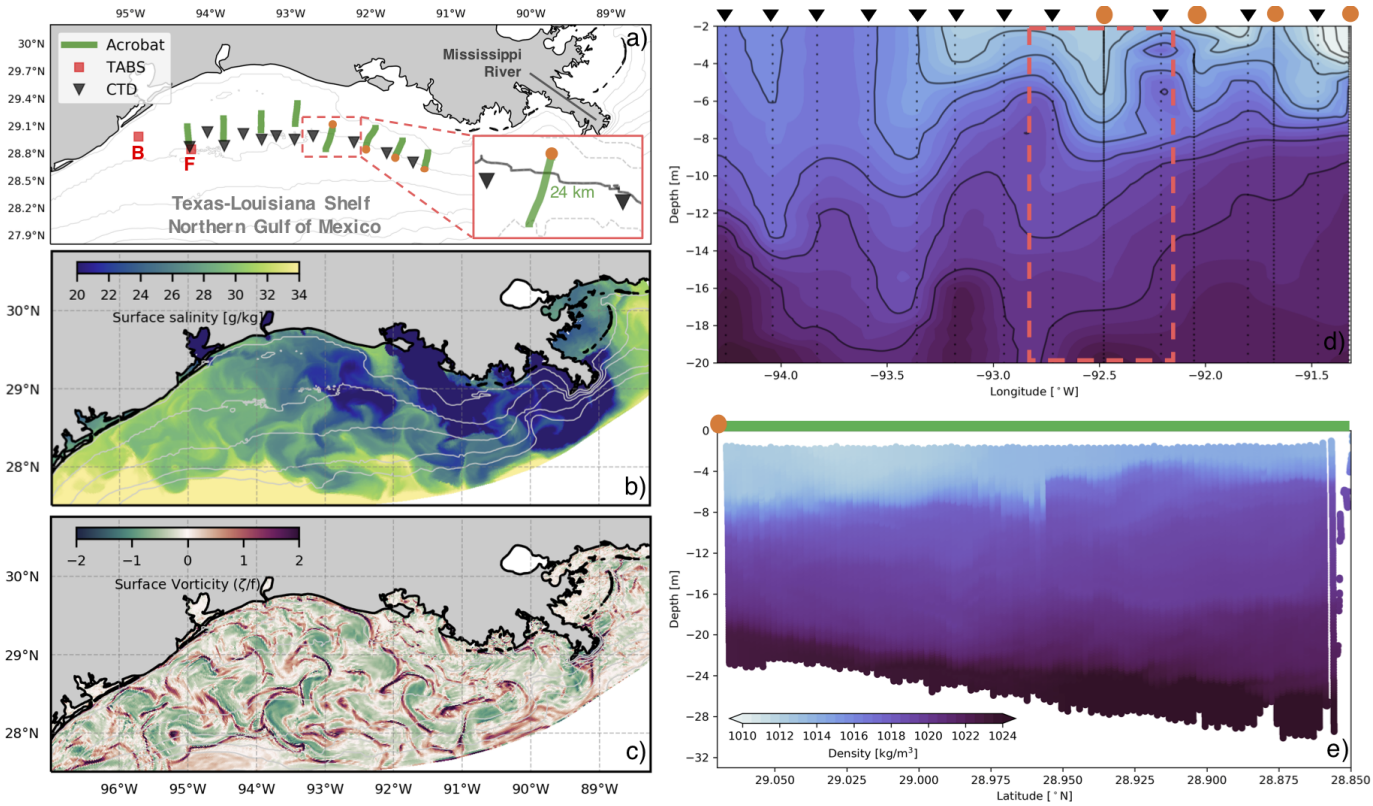

Figure 3.1: (a) MCH acrobat transects, MCH CTD stations, and TABS buoys in the northern Gulf of Mexico. MCH data were collected on Aug. 4-7, 2010. (b) Surface salinity and (c) normalized vorticity on Aug. 10, 2010, based on the TXLA model. (d) Density section along the 25m isobath with the isopycnals every 1.5 kg/m^3. Black triangles mark the CTD locations, orange circles indicate the north/south ends of the Acrobat paths, black dots mark the sampling depth, and pink box marks an vortex-like front observed at the zoomed-in field in a). (e) Across-shore density section along the Acrobat path at the zoomed-in field. Isobath contours are 10, 25, 50, 100, and 200m in a) and b) and 15, 20, 25, and 30m at the zoomed-in field.

Understanding the modifications of NIWs at vortex-like fronts is essential to predict the trapping of the NIWs, a process that may enhance mixing within ocean eddies. Recent theoretical advances indicate that the strong vorticity, strain, and lateral density gradients within submesoscale structures could facilitate the energy transfers between the waves and eddies (Taylor and Straub, 2016; Barkan et al., 2017c; Thomas, 2017; Rocha et al., 2018). So, better understanding the modifications at vortex-like fronts is helpful for further investigating the energy transfers across scales and regimes.

The Texas-Louisiana shelf in the northern Gulf of Mexico is an ideal geophysical lab to study

NIWs in a baroclinic vortex. It is a broad, shallow shelf characterized by large inputs of fresh water from the Mississippi/Atchafalaya River (Morey et al., 2003; Zhang et al., 2012, 2014). With weak winds during the summertime and relatively weak tides, submesoscale vortices along the river plume front are prevalent over the shelf due to the baroclinic instabilities in buoyancy-driven flows (DiMarco and Reid, 1998; DiMarco et al., 2000a; Hetland, 2017). Fig. 3.1 shows the simulation and observation of the vortices over the shelf. The observational data are from the hydrographic survey of the Mechanisms of Controlling Hypoxia (MCH) project in August 2010 (Zimmerle and DiMarco, 2017). The along-shore density field (Fig. 3.1d) exhibits a lot of vortex-like structures. The across-shore density of one structure (Fig. 3.1e) indicates a half of an eddy with the radius around of 20 km. This is consistent with the realistic simulation in this region, TXLA model (Zhang et al., 2012), which shows that the energetic freshwater eddies have scales of 10-50 km (see Fig. 3.1b and 3.1c). In addition, storms are infrequent in the summertime, and winds are generally mild with a notable land-sea breeze that is nearly resonant with the local inertial frequency (DiMarco et al., 2000b; Zhang et al., 2009, 2010). Fig. 3.2 shows the time series of winds and currents observed at the Texas Automated Buoy System (TABS) buoys and the associated FFT spectra. The winds are generally calm with a pronounced diurnal (near-inertial) land-sea breeze, and the near-inertial surface currents are resonantly generated by the land-sea breeze, which is conformed by the peak coincidence near the local inertial frequency in the spectra.

Some recent studies have focused on the submesoscale dynamics in the northern Gulf of Mexico based on the numerical simulations (Luo et al., 2016; Barkan et al., 2017a,b) and observations (Mariano et al., 2016; Poje et al., 2017; Haza et al., 2018). However, these studies do not examine the internal mixing caused by the vertical radiation of NIWs in this vigorous field of submesoscale vortices. Since the freshwater influence from the Mississippi/Atchafalaya River suppresses the ventilation to the subsurface and bottom water, bottom hypoxia is a significant ecological feature over the Texas-Louisiana shelf (Bianchi et al., 2010; Hetland and DiMarco, 2008). Potentially, the internal mixing can provide ventilation for the bottom water (O'Donnell et al., 2008) and hence modulate the bottom oxygen patterns, e.g., the patchiness in the seasonally hypoxic bottom wa-

ter over the shelf. One outcome of this study will be the linkage between NIWs and mixing in a coastal environment where both NIWs and ocean eddies are prevalent; it would be helpful for better understanding the biogeochemistry in coastal zones.

This chapter generalizes the NIW theory at a baroclinic jet (Whitt and Thomas, 2013) to the scenario of a baroclinic vortex and explores the difference between two modifications of NIWs. In particular, this chapter attempts to demonstrate that the curvature effect of a vortex can alter the trapping depth of NIWs and hence the mixing positions, as compared to the NIWs at a baroclinic jet.

3.2 Theory

In cylindrical coordinates, the equations governing the motion of an adiabatic inviscid fluid in a rotating system with the Boussinesq and hydrostatic approximations are

$$\begin{aligned}
\frac{\partial v_r}{\partial t} + v_r\frac{\partial v_r}{\partial r} + \frac{v_\theta}{r}\frac{\partial v_r}{\partial \theta} + w\frac{\partial v_r}{\partial z} - \frac{v_\theta^2}{r} - fv_\theta &= -\frac{1}{\rho_0}\frac{\partial p}{\partial r},\\
\frac{\partial v_\theta}{\partial t} + v_r\frac{\partial v_\theta}{\partial r} + \frac{v_\theta}{r}\frac{\partial v_\theta}{\partial \theta} + w\frac{\partial v_\theta}{\partial z} + \frac{v_r v_\theta}{r} + fv_r &= -\frac{1}{\rho_0}\frac{1}{r}\frac{\partial p}{\partial \theta},\\
-b &= -\frac{1}{\rho_0}\frac{\partial p}{\partial z},\\
\frac{\partial b}{\partial t} + v_r\frac{\partial b}{\partial r} + \frac{v_\theta}{r}\frac{\partial b}{\partial \theta} + w\frac{\partial b}{\partial z} &= 0,\\
\frac{1}{r}\frac{\partial (rv_r)}{\partial r} + \frac{1}{r}\frac{\partial v_\theta}{\partial \theta} + \frac{\partial w}{\partial z} &= 0,
\end{aligned} \tag{3.1}$$

where r is the radial distance, θ is the azimuth, z is the depth, v_r is the radial velocity (outward is positive), v_θ is the azimuthal velocity (counter-clockwise is positive), w is the vertical velocity (upward is positive), f is the Coriolis parameter, ρ_0 is the reference density, p is the pressure, and $b = g(\rho_0 - \rho)\rho_0^{-1}$ is the buoyancy. The background field is a stationary baroclinic vortex where the flow is in the thermal wind balance with the density field. The center of the cylindrical coordinates coincides with the vortex center. The background flow, then, only has the azimuthal component $V_\theta(r, z)$ which is invariant in the azimuthal direction. The momentum equations of the background

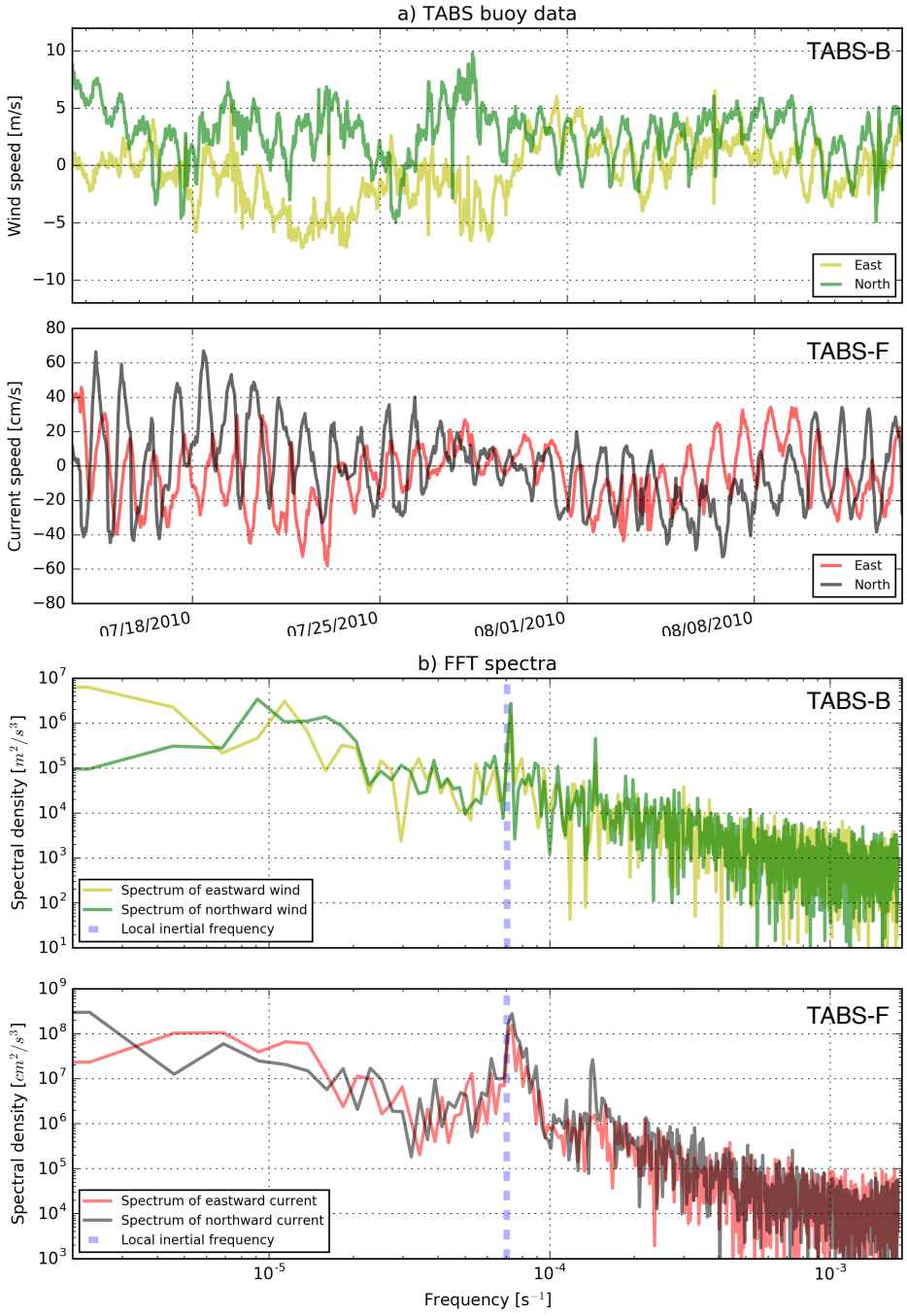

Figure 3.2: (a) Time series of the winds and surface currents at the TABS buoys (marked in Fig. 3.1). (b) FFT spectra of the wind and current data. Blue dashed lines represent the local Coriolis parameter.

sate are

$$-\frac{V_\theta^2}{r} - fV_\theta = -\frac{1}{\rho_0}\frac{\partial P}{\partial r}, \qquad -B = -\frac{1}{\rho_0}\frac{\partial P}{\partial z}, \tag{3.2}$$

where $B(r,z)$ is the background buoyancy and $P(r,z)$ is the background pressure; it says that the residual between the Coriolis force and the pressure gradient force provides the centripetal forcing in the radial direction, and the vertical direction is in the hydrostatic balance. Note that the centrifugal force V_θ^2/r modifies the classical geostrophic balance so that V_θ varies in a different way compared to the classical thermal wind relation.

The ratio between the centrifugal force and the the Coriolis force is the curvature vorticity Rossby number $Ro = \frac{\zeta_c}{f}$ corresponding to the curvature vorticity $\zeta_c = V_\theta/r$. If the flow is significantly curved ($Ro \sim 1$), the centrifugal force cannot be neglected and hence modifies the geostrophic balance. Consequently, the thermal wind relation is modified in the curved flow regime; by eliminating P in Eq. (3.2), the modified thermal wind relation can be obtained as

$$-(f + 2\zeta_c)\frac{\partial V_\theta}{\partial z} = -\frac{\partial B}{\partial r}. \tag{3.3}$$

Compared to the classical thermal wind relation, the modified relation reveals that the velocity shear is not only related to the lateral buoyancy gradient but also the curvature of the flow.

Consider a perturbed field (primed) superimposing on the background vortex (capitalized):

$$v_r = v_r^{'}, \qquad v_\theta = V_\theta + v_\theta^{'}, \qquad w = w^{'}, \qquad b = B + b^{'}, \qquad p = P + p^{'}. \tag{3.4}$$

Substituting Eq. (3.4) into Eq. (3.1) and assuming small-amplitude perturbations yields the gov-

erning equations for the perturbations:

$$\begin{aligned}
\frac{\partial v_r^{'}}{\partial t} - (f + \frac{2V_\theta}{r})v_\theta^{'} &= -\frac{1}{\rho_0}\frac{\partial p^{'}}{\partial r}, \\
\frac{\partial v_\theta^{'}}{\partial t} + v_r^{'}\frac{\partial V_\theta}{\partial r} + w^{'}\frac{\partial V_\theta}{\partial z} + (f + \frac{V_\theta}{r})v_r^{'} &= 0, \\
-b^{'} &= -\frac{1}{\rho_0}\frac{\partial p^{'}}{\partial z}, \\
\frac{\partial b^{'}}{\partial t} + v_r^{'}\frac{\partial B}{\partial r} + w^{'}\frac{\partial B}{\partial z} &= 0, \\
\frac{\partial r v_r^{'}}{\partial r} + \frac{\partial r w^{'}}{\partial z} &= 0.
\end{aligned} \tag{3.5}$$

Note that, since we are focusing on the propagation of the perturbations in the radial direction, the perturbations are assumed to be invariant in the azimuthal direction. To satisfy the continuity equation above, we can introduce a streamfunction Φ such that

$$v_r^{'} = \frac{1}{r}\frac{\partial \Phi}{\partial z} \quad and \quad w^{'} = -\frac{1}{r}\frac{\partial \Phi}{\partial r}. \tag{3.6}$$

Following the derivation in Appendix D, a partial differential equation (PDE) for Φ can be obtained as

$$\frac{1}{r}\frac{\partial^4 \Phi}{\partial t^2 \partial z^2} + \frac{\partial}{\partial r}(\frac{N^2}{r}\frac{\partial \Phi}{\partial r} + \frac{M^2}{r}\frac{\partial \Phi}{\partial z}) + \frac{\partial}{\partial z}(\frac{M^2}{r}\frac{\partial \Phi}{\partial r} + \frac{{f_{eff}^*}^2}{r}\frac{\partial \Phi}{\partial z}) = 0, \tag{3.7}$$

where $f_{eff}^* = \sqrt{(f + 2\zeta_c)(f + \zeta_c + \zeta_s)}$ is the modified effective inertial frequency in the curved flow case, $\zeta_s = \frac{\partial V_\theta}{\partial r}$ is the shearing vorticity, $\zeta_c = V_\theta / r$ is the curvature vorticity, $M^2 = -\frac{\partial B}{\partial r}$ is the background lateral density gradient, and $N^2 = \frac{\partial B}{\partial z}$ is the background stratification; this shifts the Eliassen-Sawyer equation (Eliassen, 1951; Sawyer, 1956; Eliassen, 1962) to a time-dependent form which describes the propagation of NIWs within a baroclinic vortex. The physical meaning of f_{eff}^* will be discussed in Section 3.3.2.

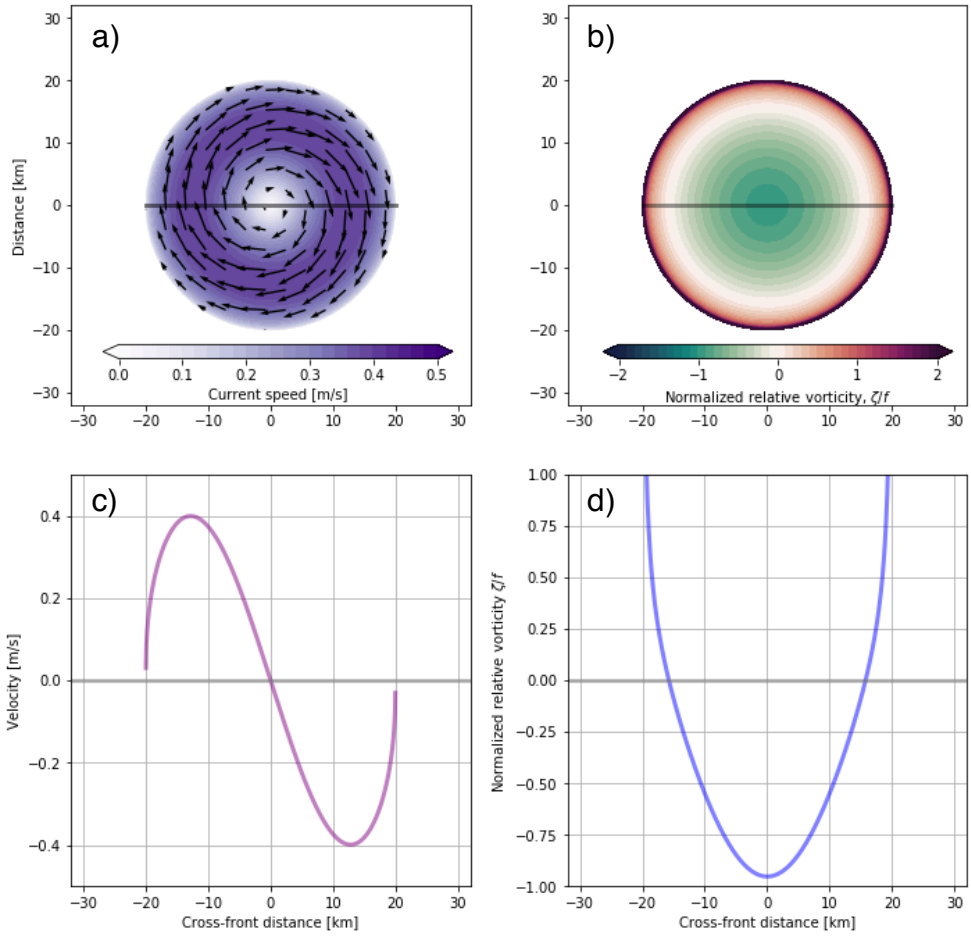

Figure 3.3: Surface (a) velocity and (b) relative vorticity of the idealized anti-cyclonic vortex. Profiles of (c) velocity and (d) relative vorticity along the gray lines marked in (a) and (b). Relative vorticity is normalized by $f = 10^{-4}\ s^{-1}$.

3.3 Propagation of Near-Inertial Waves in a Baroclinic Vortex

3.3.1 Idealized Baroclinic Vortex

To demonstrate the modifications of NIWs in a baroclinic vortex, an idealized vortex is constructed to mimic the observed vortex shown in Fig. 3.1. The velocity structure of the vortex is as follows (see Fig. 3.4b)

$$V_\theta(r,z) = -c_1\, cos^n(\frac{\pi r}{2R})\, sin^m(\frac{\pi r}{2R})\, [1 + tanh(c_2\frac{z}{H} + c_3)], \tag{3.8}$$

where $R = 20\ km$ is the radius, $H = 23\ m$ is the thickness, and $n = 0.4$, $m = 1.0$, $c_1 = 0.47\ m/s$, $c_2 = 3$, $c_3 = 0.3$ are the tuning constants. The surface velocity field and the associated vorticity field are shown in Fig. 3.3 – the vortex is an anti-cyclone and the flow is both curved and sheared. The radius of the vortex is comparable to the observed vortex-like front over the Texas-Louisiana shelf (see the lower panel of Fig. 3.1). The vorticity of the vortex has the similar features as revealed in the realistic simulation over the shelf (Zhang et al., 2012) – the vortices have negative vorticity in the cores with positive vorticity around (see the upper panel of Fig. 3.9).

The density structure of the vortex is calculated by integrating the modified thermal wind relation Eq. (3.3). First, we use the density profile at the north end of the observed vortex-like front as a reference to create an idealized density profile at the center of the idealized vortex (see Fig. 3.4a). Second, we integrate Eq. (3.3) from the center to the edge by making use of the velocity structure Eq. (3.8). The integrated density field is shown in Fig. 3.4c – the constructed vortex is similar to the observed vortex-like front.

3.3.2 Dispersion Relation and Minimum Frequency

To obtain the dispersion relation of the NIWs in a baroclinic vortex, we apply the Wentzel-Kramers-Brillouin (WKB) approximation and hence assume that the variables in Eq. (3.5) have the wave form $\phi(r,z,t) = \widetilde{\phi}e^{i(k_r r + k_z z - \sigma t)}$. This linearization approximation is only valid when the background field does not significantly change within the scale of the wavelength. We will crudely

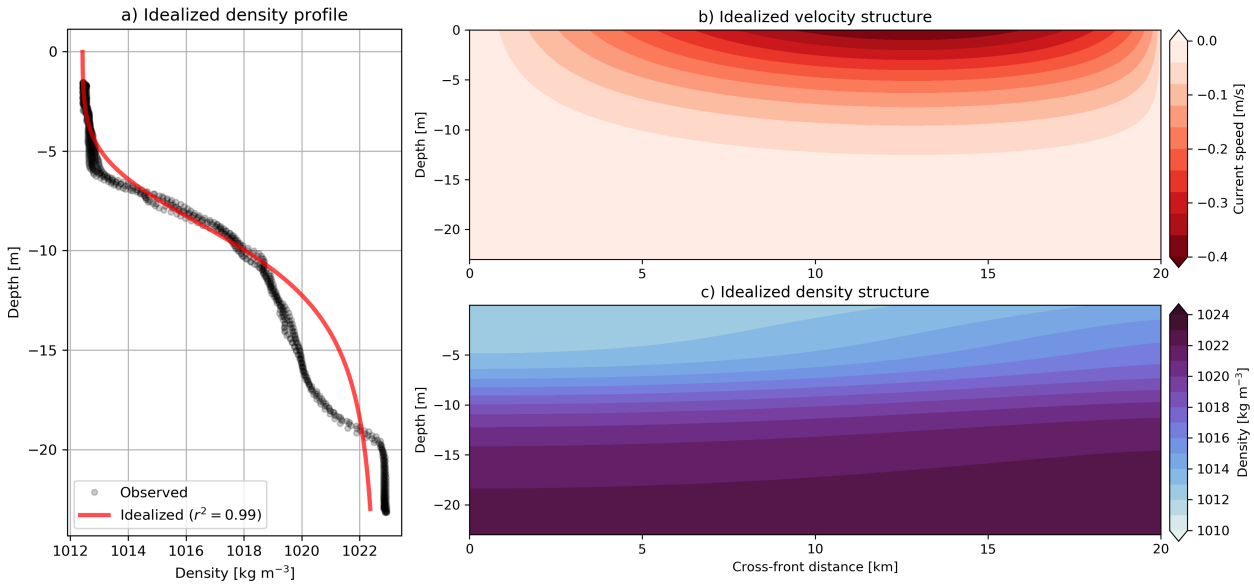

Figure 3.4: (a) Idealized and observed density profiles at the vortex center. Radial sections of (b) velocity and (c) density within the idealized vortex.

accept this approximation at first and then validate this approximation by numerically solving the Eliassen-Sawyer equation that does not assume the spatial scale separation. Substituting the wave forms into Eq. (3.5) and letting the determinant to be zero yield the dispersion relation,

$$\sigma = \sqrt{{f^*_{eff}}^2 + 2M^2\frac{k_r}{k_z} + N^2(\frac{k_r}{k_z})^2}, \tag{3.9}$$

where $f^*_{eff} = \sqrt{(f + 2\zeta_c)(f + \zeta_c + \zeta_s)}$ is the modified effective inertial frequency, σ is the wave frequency, and k_r and k_z are the wavenumbers in the radial and vertical directions, respectively.

To interpret the physical meaning of f^*_{eff}, we need to analogize it to $f_{eff} = \sqrt{f(f + \zeta_s)}$, which is the effective inertial frequency in the jet-like front case (Mooers, 1975; Whitt and Thomas, 2013; Thomas, 2017). For near-inertial oscillations (purely horizontal motions), the oscillating frequency is equal to f_{eff} in the jet-like front case and f^*_{eff} in the vortex-like front case. The latter one is obtained by setting $k_r = 0$ in Eq. (3.9). Contrasting f^*_{eff} to f_{eff}, we can see that f^*_{eff} is not only related to the shear of the flow but also the curvature. The schematic in Fig. 3.5 illustrates the shear and curvature of a flow. A flow can be decomposed into a sheared flow without curvature

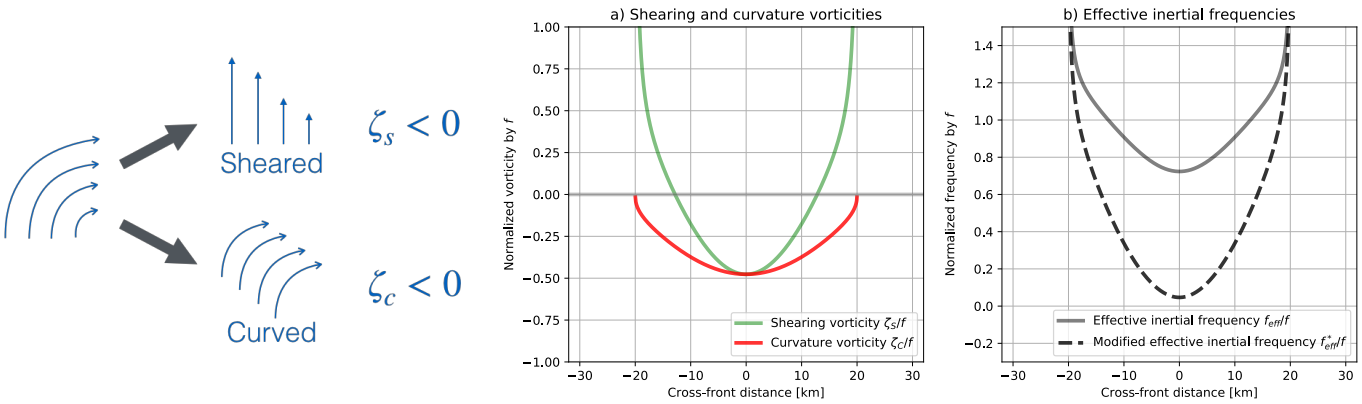

Figure 3.5: Schematic illustrating the shearing vorticity ζ_s and curvature vorticity ζ_c of an anti-cyclonic flow. (a) Radial profiles of the shearing vorticity ζ_s and curvature vorticity ζ_c at the surface of the idealized vortex. (b) Radial profiles of the effective inertial frequency f_{eff} and the modified effective inertial frequency f^*_{eff} at the surface of the idealized vortex.

and a curved flow without shear. The curvature vorticity ζ_c and shearing vorticity ζ_s represent the vorticity of those two different types of flow components. The total vorticity of the flow is the sum of ζ_c and ζ_s. Consequently, f^*_{eff} is not only modified by the total vorticity $\zeta_c + \zeta_s$ that alters the net spin of the fluid, but also modified by the curvature vorticity ζ_s that alters the net spin of the rotating framework. If the background flow field is an anti-cyclone, ζ_c is negative, and hence $f^*_{eff} < f_{eff}$. Fig. 3.5a shows the surface curvature vorticity ζ_c and shearing vorticity ζ_s of the idealized anti-cyclone. ζ_c and ζ_s are both negative in the core and at similar magnitudes. The curvature of the flow (represented by ζ_c) causes a significant reduction on the effective inertial frequency (see the contrast shown in Fig. 3.5b).

According to the dispersion relation Eq. (3.9), the minimum frequency of NIWs in a baroclinic vortex is

$$\sigma_{min} = \sqrt{{f^*_{eff}}^2 - M^4/N^2} = f\sqrt{(1+2\frac{\zeta_c}{f})(1+Ro) - (1+2\frac{\zeta_c}{f})^2 Ri^{-1}}, \tag{3.10}$$

where $Ro = (\zeta_c + \zeta_s)f^{-1}$ is the vorticity Rossby number and $Ri = N^2(\frac{\partial V_\theta}{\partial z})^{-2} = N^2M^{-4}(f + 2\zeta_c)^2$ is the Richardson number. $\sigma_{min} = \sqrt{{f^*_{eff}}^2 - M^4/N^2}$ is identical to the expression (B9) of

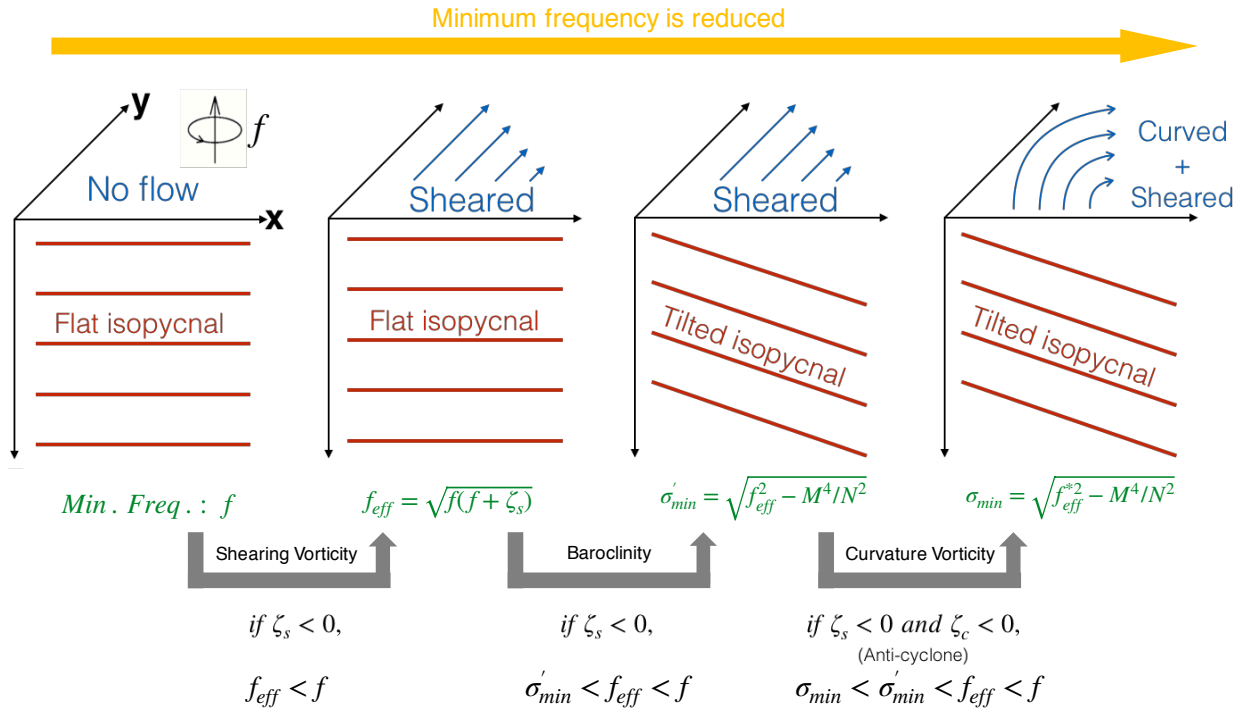

Figure 3.6: Schematic illustrating the modification cascade of the minimum frequency by the shearing vorticity, frontal baroclinity, and curvature vorticity.

Joyce et al. (2013). If the front is with negligible curvature ($\zeta_c \ll f$), σ_{min} reduces to $\sigma'_{min} = \sqrt{f_{eff}^2 - M^4/N^2} = f\sqrt{1 + Ro - Ri^{-1}}$ (Whitt and Thomas, 2013). Whitt and Thomas (2013) shows that, at a baroclinic jet with anti-cyclonic vorticity, the minimum frequency of NIWs is reduced down from f_{eff} to σ'_{min} because of the baroclinity. Our study shows that, in a baroclinic anti-cyclone, the minimum frequency is further reduced down from σ'_{min} to σ_{min} because of the curvature effect of the vortex (the curvature shifts f_{eff} down to f^*_{eff}). The modification cascade of the minimum frequency by the shearing vorticity, frontal baroclinity, and curvature vorticity are illustrated in Fig.3.6.

Fig. 3.7a and 3.7b show the comparison of f_{eff} and f^*_{eff} based on the idealized vortex – the curvature of the vortex significantly reduces the effective frequency. Fig. 3.7c shows several separatrices within the idealized vortex, where the minimum frequencies of various scenarios (f_{eff}, σ'_{min}, and σ_{min}) are equal to the wave frequencies ($\sigma = 0.95f$ and $\sigma = 0.98f$). Inside of a separatrix, the wave frequency is larger than the minimum frequency such that the wave can be supported.

On a separatrix, the group speed of the wave is equal to zero. Outside of a separatrix, the wave frequency is smaller than the minimum frequency so that the wave can not be supported. In other words, the region enclosed by a separatrix is the allowable area where the wave with the corresponding frequency can exist and propagate, and the wave can not escape outside. Consistent with Whitt and Thomas (2013), the baroclinity extends the propagation area; the curvature effect further extends the propagation area beyond the baroclinity – this implies that NIWs within a vortex can propagate wider and deeper than previously predicted.

3.3.3 Wave Propagation and Ray Tracing

According to the dispersion relation Eq. (3.9), the slope of the wave energy propagation (slope of wave group velocity with respect to horizontal) S_E is a function of the wave frequency σ,

$$S_E^{+,-} \equiv \frac{C_{gz}}{C_{gr}} = S_\rho \pm \sqrt{\frac{\sigma^2 - \sigma_{min}^2}{N^2}}, \tag{3.11}$$

where $S_\rho = M^2/N^2$ is the isopycnal slope, $\pm$ represent the two wave characteristics, and C_{gr} and C_{gz} are the group velocity components in the radial and vertical directions, respectively. This relation is similar to the result in the case of the baroclinic jet but with σ_{min} replacing $\sigma_{min}^{'}$ (Thomas, 2017). If $\sigma = \sigma_{min}$, $S_E = S_\rho$; the wave energy propagation is along the isopycnal, but, in fact, there is no energy propagating out because $\vec{C_g} = 0$ if $\sigma = \sigma_{min}$. Consequently, $\sigma = \sigma_{min}$ is the necessary condition of wave trapping or reflection at a turning point.

Left panels of Fig. 3.8 show the comparison of $S_E^{+,-}$ in the idealized vortex and in the jet-like front where the curvature is neglected by simply setting ζ_c to zero. Eq. (3.11) is valid only inside of the separatrix, where $\sigma_{min} < \sigma$. $S_E^{+,-}$ in the vortex not only span a larger region than in the jet, but also have larger values; this implies that the curvature effect facilitates the vertical radiation of the NIWs.

In addition, ray tracing is conducted in both fronts, which is shown in the right panels of Fig. 3.8. The procedure of ray tracing can be found in Whitt and Thomas (2013) and Whitt et al. (2018) but is briefly described here. The heading of a wave ray is determined by S_E. As the wave

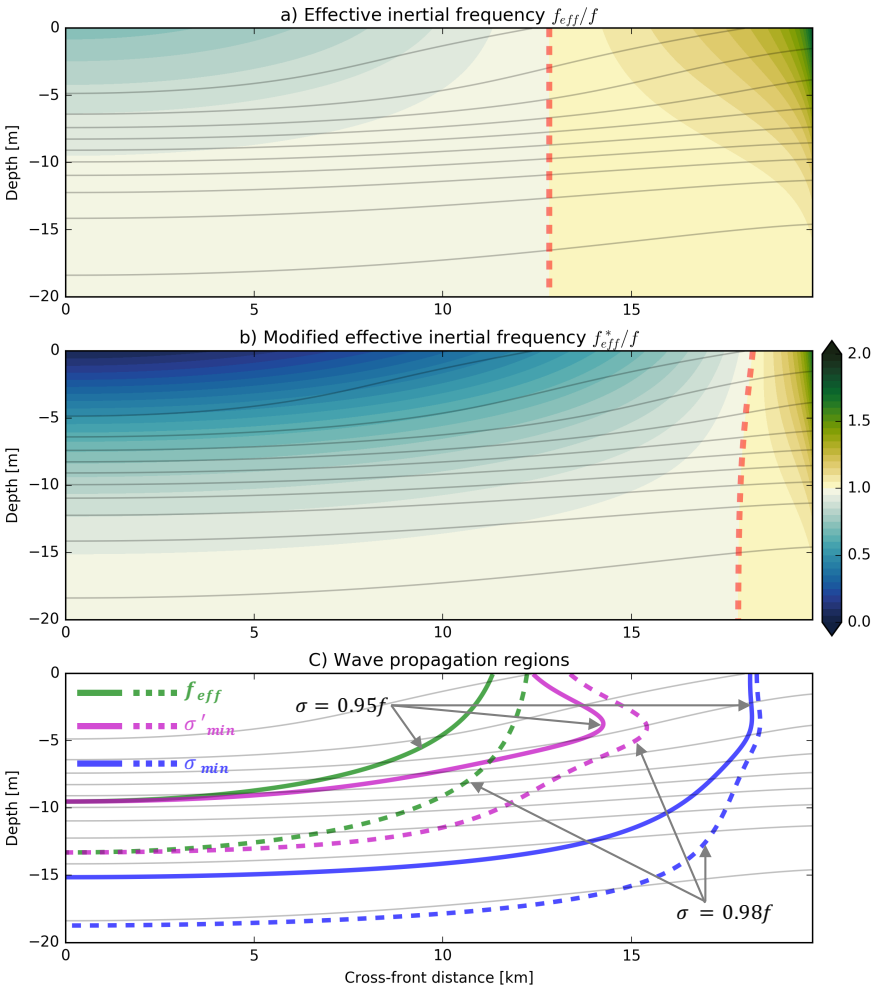

Figure 3.7: Across-front sections of f_{eff} (a) and f^*_{eff} (b). Red dashed lines represents $f_{eff} = f$ and $f^*_{eff} = f$. (c) Propagation regions of the waves with the frequencies of $\sigma = 0.95f$ (solid lines) and $\sigma = 0.98f$ (dashed lines). The propagation boundaries are marked by the separatrices of $f_{eff} = \sigma$ (green lines), $\sigma'_{min} = \sigma$ (magenta lines), and $\sigma_{min} = \sigma$ (blue lines). $\sigma'_{min} = \sqrt{f^2_{eff} - M^4/N^2}$ (Eq. (19) of Whitt and Thomas (2013)) and $\sigma_{min} = \sqrt{{f^*_{eff}}^2 - M^4/N^2}$ (Eq. (3.10)). Isopycnals are marked by the gray lines every 1 kg/m^3.

proceeds, S_E is updated to determine the heading, and C_g is updated to determine the speed of the waveguide. S_E switches signs at the separatrix to create reflections. In this study, S_E is also set to switch signs at the core of a vortex. The ray tracing results shown in Fig. 3.8 indicate that the waves in the vortex propagate wider and deeper than in the jet, and the wave rays are trapped at the base of the vortex where the group speed is near to zero. Thus, the wave trapping condition can be concluded as follows: the trapping must occur at the locations where $S_E = S_\rho$ (for $\vec{C_g} = 0$) and the slope of the separatrix is also equal to S_ρ (for creating an infinite reflection zone). Based on the ray tracing results, it can be inferred that the curvature effect of an anti-cyclone can cause deeper trapping and hence deeper mixing than previously predicted.

3.4 Energetics of Near-Inertial Waves in a Baroclinic Vortex

The energetics of NIWs in a baroclinic vortex is investigated via a parcel argument (the parcel argument is demonstrated in Appendix E). The parcel argument links the wave energy density to the stream function so that the wave energy can be obtained by numerically solving the Eliassen-Sawyer equation derived in Section 3.2. The numerical calculation of the wave energy density will be also used to test the WKB approximation made for the dispersion relation and the consequent theoretical analysis in Section 3.3.

3.4.1 Formulating Wave Energy Density

The following derivation is to formulate the energy density of the NIWs in a baroclinic vortex as a function of the stream function. First, we link the wave energy density to the displacement of the parcel argument. According to Appendix E, the perturbed variables can be expressed by the displacement $\vec{\delta} = R\vec{i} + Z\vec{k}$ as follows

$$v_r^{'} = \frac{\partial R}{\partial t},\ v_\theta^{'}(t) = -(f + \zeta_c + \zeta_s)R - \frac{\partial V_\theta}{\partial z}Z,\ and\ b^{'}(t) = M^2R - N^2Z. \tag{3.12}$$

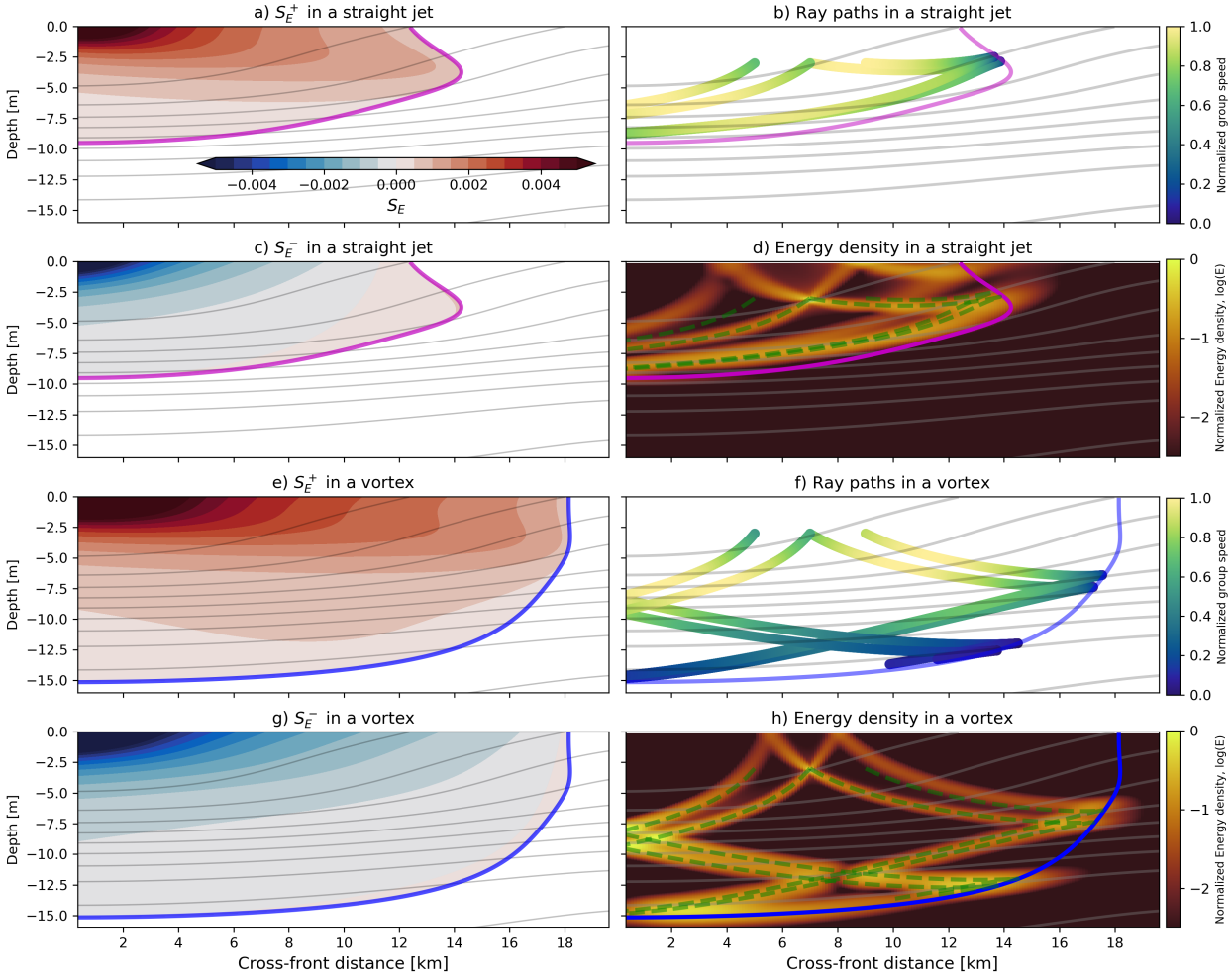

Figure 3.8: Slope of energy propagation S_E (a and c), ray tracing (b) and energy density (d) of the NIWs with $\sigma = 0.95f$ in the jet-like front where the curvature vorticity of the idealized vortex is ignored. Same properties are calculated in the idealized vortex (e, f, g, and h). Three point sources are set at ($r = 5, 7, 9\ km,\ z = -3\ m$) for the ray tracing calculations, and one point source at ($r = 7\ km,\ z = -3\ m$) for the energy density calculations. Group speed is normalized by the maximum and colored on the rays. Energy density is also normalized by the maximum. Wave rays are overlaid on the energy density plots. $\sigma'_{min} = 0.95f$ and $\sigma_{min} = 0.95f$ are marked by the magenta and blue lines, respectively. Isopycnals are marked every 1 kg/m^3 by the gray lines.

Substituting these relations to the radial and vertical momentum equations of Eq. (3.5) and applying the modified thermal wind relation Eq. (3.3), we can get

$$\frac{\partial^2 R}{\partial t^2} + {f^*_{eff}}^2 R - M^2 Z = -\frac{1}{\rho_0}\frac{\partial p^{'}}{\partial r}, \tag{3.13}$$

$$-M^2 R + N^2 Z = -\frac{1}{\rho_0}\frac{\partial p^{'}}{\partial z}. \tag{3.14}$$

Multiply Eq. (3.13) by $r\hat{v_r^{'}}$ and Eq. (3.14) by $r\hat{w^{'}}$ ($<\hat{\cdot}>$ means the complex conjugate) and add them together to get

$$\frac{\rho_0}{2}\frac{\partial}{\partial t}[|\frac{\partial R}{\partial t}|^2 + {f^*_{eff}}^2|R|^2 - 2M^2 R\hat{Z} + N^2|Z|^2] = -\frac{1}{r}[\frac{\partial p^{'}}{\partial r}(r\hat{v_r^{'}}) + \frac{\partial p^{'}}{\partial z}(r\hat{w^{'}})]. \tag{3.15}$$

Making use of the continuity equation in Eq. (3.5) and the divergence operator in cylindrical coordinates $\nabla \cdot \vec{a} \equiv \frac{1}{r}\frac{\partial r a_r}{\partial r} + \frac{1}{r}\frac{\partial a_\theta}{\partial \theta} + \frac{\partial a_z}{\partial z}$, the right-hand side of Eq. (3.15) can be rewritten as

$$-\frac{1}{r}[\frac{\partial p^{'}}{\partial r}(r\hat{v_r^{'}}) + \frac{\partial p^{'}}{\partial z}(r\hat{w^{'}})] = -\frac{1}{r}[\frac{\partial p^{'}(r\hat{v_r^{'}})}{\partial r} + \frac{\partial p^{'}(r\hat{w^{'}})}{\partial z}] = -\nabla \cdot (p^{'}\vec{\hat{v}}) \tag{3.16}$$

where $\vec{\hat{v}} = (\hat{v_r^{'}}, \hat{w^{'}})$; this implies that the right-hand side of Eq. (3.15) is the convergence of the pressure work. Thus, the left-hand side of Eq. (3.15) must be the changing rate of the energy density (the wave energy per unit volume); the energy density, E, as a function of the displacement $\delta = (R, Z)$ can be expressed as

$$E = \frac{\rho_0}{2}[|\frac{\partial R}{\partial t}|^2 + {f^*_{eff}}^2|R|^2 - 2M^2 R\hat{Z} + N^2|Z|^2]. \tag{3.17}$$

Second, we link the energy density E to the stream function Φ. Assuming that the displacement δ has the form of $(Re^{-i\sigma t}, Ze^{-i\sigma t})$, we can obtain $v_r^{'} \equiv \frac{\partial R}{\partial t} = -i\sigma R$ and $w^{'} \equiv \frac{\partial Z}{\partial t} = -i\sigma Z$. Given

$v_r' = \frac{1}{r}\frac{\partial \Phi}{\partial z}$ and $w' = -\frac{1}{r}\frac{\partial \Phi}{\partial r}$, we can get

$$\begin{aligned} R &= \frac{1}{r}\frac{i}{\sigma}\frac{\partial \Phi}{\partial z}, \\ \hat{Z} &= \frac{1}{r}\frac{i}{\sigma}\frac{\partial \hat{\Phi}}{\partial y}. \end{aligned} \tag{3.18}$$

Substituting Eq. (3.18) into Eq. (3.17) to eliminate R and $\hat{Z}$, Eq. (3.17) can be rewritten as

$$E = \frac{1}{r^2}\frac{\rho_0}{2\sigma^2}[({f^*_{eff}}^2 + \sigma^2)|\Phi_z|^2 + 2M^2\Phi_z\hat{\Phi}_r + N^2|\Phi_r|^2]. \tag{3.19}$$

Assuming that $\Phi(r, z, t) = \phi(r, z)e^{-i\sigma t}$, the time-averaged (averaged in a period) wave energy density $\bar{E}$ can be expressed as

$$\bar{E} = \frac{1}{r^2}\frac{\rho_0}{4\sigma^2}[({f^*_{eff}}^2 + \sigma^2)|\phi_z|^2 + 2M^2\phi_z\hat{\phi}_r + N^2|\phi_r|^2]. \tag{3.20}$$

3.4.2 Numerical Calculation of Wave Energy Density

In this section, we will calculate the wave energy density based on Eq. (3.20) by numerically solving the Eliassen-Sawyer equation Eq. (3.7). The WKB approximation will be tested by comparing the energy distribution with the ray tracing results of Section 3.3.3.

The Eliassen-Sawyer equation Eq. (3.7) is numerically solved with the idealized vortex as the background field. The velocity and density fields of the vortex are shown in Fig. 3.4. The method of images is used to solve for the Green's function of the Eliassen-Sawyer equation – a mirror image of the idealized vortex is attached at $r = 0$. The boundary condition $\phi = 0$ is applied at all four walls of the extended domain. Given an oscillating wave maker, the stream function $\phi(r, z)$ can be, then, obtained by numerically solving the Eliassen-Sawyer equation, and hence the energy density $\bar{E}$ can be calculated according to Eq. (3.20). The details of the numerical method can be found in Section 5.b of Whitt and Thomas (2013). Fig. 3.8h shows an example of the energy density of the NIWs that are forced by the wave maker at $r = 7km$ and $z = -3m$.

The wave energy density is also calculated in the jet-like front case where the curvature of the

idealized vortex is neglected by simply setting ζ_c to zero. As demonstrated in Whitt and Thomas (2013), the stream function Ψ of the NIWs at a baroclinic jet is governed by

$$(f_{eff}^2 + \frac{\partial^2}{\partial t^2})\frac{\partial^2 \Psi}{\partial z^2} + 2M^2 \frac{\partial^2 \Psi}{\partial z \partial y} + N^2 \frac{\partial^2 \Psi}{\partial y^2} = 0, \tag{3.21}$$

where y represents the across-front direction; it is the Eliassen-Sawyer equation in Cartesian coordinates. Assuming $\Psi(y, z, t) = \psi(y, z)e^{-i\sigma t}$, the time-averaged wave energy density $\bar{E}$ is expressed as

$$\bar{E} = \frac{\rho_0}{4\sigma^2}[({f_{eff}}^2 + \sigma^2)|\psi_z|^2 + 2M^2 \psi_z \hat{\psi_y} + N^2 |\psi_y|^2]. \tag{3.22}$$

$\bar{E}$ can be calculated by numerically solving Eq. (3.21) for ψ. Fig. 3.8d shows the energy density of the NIWs that are forced by the same wave maker but at the jet-like front.

In both cases, the ray tracing results (under the WKB assumption) are consistent with the numerical calculations of wave energy density (based on the Eliassen-Sawyer equations); it implies that the WKB approximation is valid. Furthermore, in the vortex case, there are two hotspots of high energy at the base corresponding to the trapping locations revealed by the ray tracing. The curvature effect causes the waves to propagate deeper and also cause the wave energy to be accumulated deeper. Potentially, the internal wave continuum can be energized there; eventually, the energy will be transferred to the small-scale turbulence which can significantly enhance the mixing at the wave trapping locations.

3.5 Numerical Simulations of Near-Inertial Waves in a Baroclinic Vortex

3.5.1 Idealized Simulation

Hydrodynamic model employed in this study is the Regional Ocean Modeling System (ROMS), which is a free-surface, hydrostatic, primitive equation ocean model using the S-coordinate in the vertical direction (Shchepetkin and McWilliams, 2005). The idealized model domain is an $80\ km \times 80\ km$ domain with the uniform depth of 23 m. The horizontal resolution is $200\ m \times 200\ m$ and there are 30 layers in the vertical direction. The boundary conditions are set to be periodic at

all four open boundaries. The initial condition is based on the idealized vortex shown in Fig. 3.4. The temperature is uniformly set to $25°C$, and hence the density is determined by the salinity. Equation of state of seawater is a linear equation,

$$\rho = 1027.0[1.0 + 7.6 \times 10^{-4}(salinity - 35.0)]; \tag{3.23}$$

the salinity field is calculated by solving the equation above with the density field specified in Fig. 3.4c. The vortex is located at the middle of the domain; the velocity and salinity outside the vortex are set to be the values at the vortex edge. The wind forcing is an oscillating wind in the y-direction with an amplitude of $3\ m/s$; the oscillating frequency is set to be 0.95f ($f = 10^{-4}\ s^{-1}$), which is equivalent to an oscillating period of 18.4 hours. The simulation runs for 20 oscillating periods. MPDATA scheme is used for the tracer advection (Smolarkiewicz and Margolin, 1998). $k - \epsilon$ turbulence closure scheme is used to calculate the vertical mixing, and Canuto A stability function formulation is applied (Umlauf and Burchard, 2003; Canuto et al., 2001).

NIWs are resonantly forced by the oscillating wind, and the vortex is advected by the near-inertial motions (not shown). The "jiggling" of this idealized vortex under the oscillating forcing is similar to the behaviors of the anti-cyclones in the TXLA model (see animations on the TABS website, Thyng and Marta-Almeida (2017)). Fig. 3.9 shows the vertical shear of the unbalanced, azimuthal flow at the section crossing the vortex center. The unbalance flow is the flow deviating the initial, balanced flow and hence can represent the NIWs. The vertical shear of the unbalanced flow is, then, an effective metric to indicate the intensity of the NIWs. Fig. 3.9 indicates that the separatrix of $\sigma'_{min} = 0.95f$ can not enclose the propagation region – the NIWs propagate wider and deeper than in the jet case. However, the separatrix of $\sigma_{min} = 0.95f$ better predicts the propagation boundary of the NIWs. This contrast reveals that the curvature effect is an important agent for the propagation and trapping of the NIWs in a baroclinic vortex, and the fully non-linear simulation further validates and supports the theoretical analysis in Section 3.3.

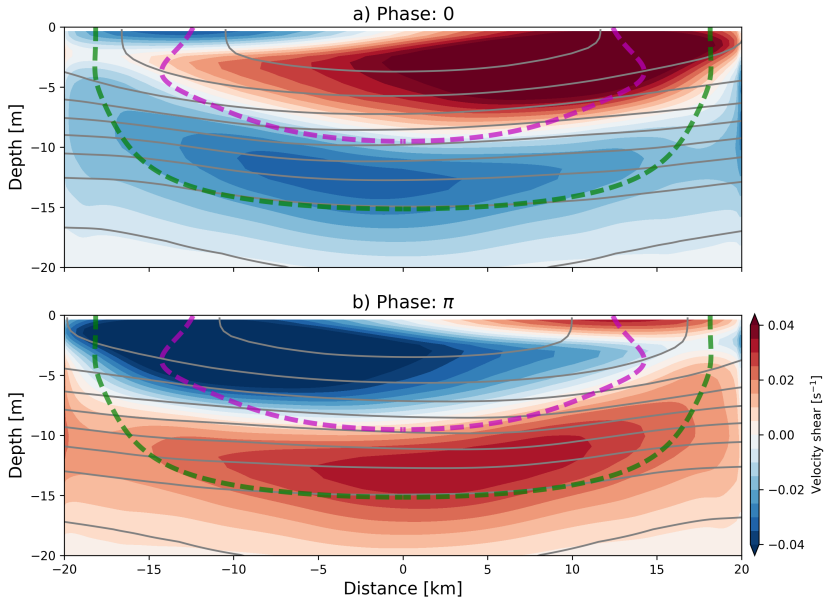

Figure 3.9: Velocity shear of the unbalanced flow along the section across the vortex center, based on the idealized ROMS simulation. Two phases (0 and π) in one inertial period are selected. $\sigma^{'}_{min} = 0.95f$ and $\sigma_{min} = 0.95f$ are marked by the magenta and green lines, respectively. Isopycnals are marked by the gray lines every 1 kg/m^3.

3.5.2 Realistic Simulation

An existing, realistic simulation in the northern Gulf of Mexico, TXLA model (Zhang et al., 2012; Hetland and DiMarco, 2012b), is used to illustrate the features of the NIWs within a baroclinic vortex. The model is implemented based on the ROMS and has a horizontal resolution of about 1 km in the region of the Texas-Louisiana shelf with 30 layers in the vertical. The model uses the 3-hourly atmospheric forcing to resolve the diurnal land-sea breeze and the daily river discharge of the Mississippi/Atchafalaya river to reproduce the river plume. The model is nested within the HYCOM model. MPDATA is used for the tracer advection, and $k-\epsilon$ turbulent closure for the vertical mixing.

Top panels of Fig 3.10 show the model snapshots of the surface salinity and the normalized vertical vorticity ζ/f, illustrating the eddies along the Mississippi/Atchafalaya river plume front. The eddies have scales of 10-50 km. The eddies are often with negative vorticity in the cores and surrounded by the fronts with significant positive vorticity (the magnitude often exceeds the planetary vorticity f). Middle panels of Fig 3.10 show a pronounced diurnal land-sea breeze (indicated by the wind stress) and the resonantly forced oscillating currents with the velocity vector tracing the ellipses. The near-inertial oscillations are persistent even when the winds are weak. Presumably, the surface oscillating motions can trigger the vertically radiating NIWs, because the NIWs could be modified by the front and hence radiate downward (see Fig. 3.8). Bottom panels of Fig 3.10 show the vorticity and turbulent kinetic energy (TKE) dissipation rate along a transect through an anti-cyclone. The negative vorticity is evident in the core of the anti-cyclone. The TKE dissipation rate is inferred from the $k-\epsilon$ model and can be used to indicate the intensity of mixing. The enhanced mixing (approaching 1×10^{-5} W/kg) is not only found within the outcropping surface front but also in the stratified interior at the base of the anti-cyclone.

The enhanced mixing in the stratified interior is speculated to be caused by the downward radiation of NIWs and the consequent trapping of the NIWs. To conform this, the ray tracing of NIWs is conducted with the consideration of the curvature effect of the anti-cyclone. The waves are forced by the wave makers with the frequency of f, and the wave rays are initiated

at the subsurface. The bottom panel of Fig 3.10 shows the ray tracing result. Two sets of the wave rays converge in the stratified interior; the positions of the convergence are corresponding to the locations where the interior mixing is strongest. Presumably, the wave trapping and the consequent wave amplification can create strong shear to trigger secondary instabilities, small-scale turbulence, and hence the enhanced mixing. Furthermore, the convergence of wave rays near the bottom seems to be related to the bottom critical reflection of NIWs – the wave rays are parallel with the bottom and experiencing the focusing reflection; this mirrors the surface critical reflection of NIWs revealed by Grisouard and Thomas (2015, 2016).

3.6 Discussion and Conclusions

The restoring mechanism of the NIWs in a baroclinic vortex relies on the conservation of absolute angular momentum. The absolute angular momentum of a fluid parcel with unit mass in a rotating system is defined as $\vec{L} = r^2\vec{\omega} + r^2\vec{\Omega}$, where r^2 represents the moment of inertia of the parcel, $\vec{\omega} = \frac{\vec{r}\times\vec{v}}{r^2}$ is the relative angular velocity of the parcel, and $\vec{\Omega} = \frac{f}{2}\vec{k}$ is the angular velocity of the rotating system. Given that the vertical component of $\vec{\omega}$ is $\omega = \frac{v_\theta}{r}$, the vertical component of $\vec{L}$ is, then,

$$L = rv_\theta + \frac{1}{2}fr^2. \tag{3.24}$$

On the other hand, the azimuthal momentum equation in Eq. (3.1) can be expressed as

$$\frac{dv_\theta}{dt} + \frac{v_r v_\theta}{r} + fv_r = 0, \tag{3.25}$$

where $\frac{d}{dt} \equiv \frac{\partial}{\partial t} + v_r\frac{\partial}{\partial r} + \frac{v_\theta}{r}\frac{\partial}{\partial \theta} + w\frac{\partial}{\partial z}$ is the material derivative. Multiplying both sides of Eq. (3.25) by r and applying $v_r \equiv \frac{dr}{dt}$, Eq. (3.25) can be rewritten as

$$\frac{d(rv_\theta + \frac{1}{2}fr^2)}{dt} \equiv \frac{dL}{dt} = 0; \tag{3.26}$$

it implies that the absolute angular momentum L is conserved following a fluid parcel if the flow is azimuthally symmetric and there are no torques in the rotating system. This conservation principle

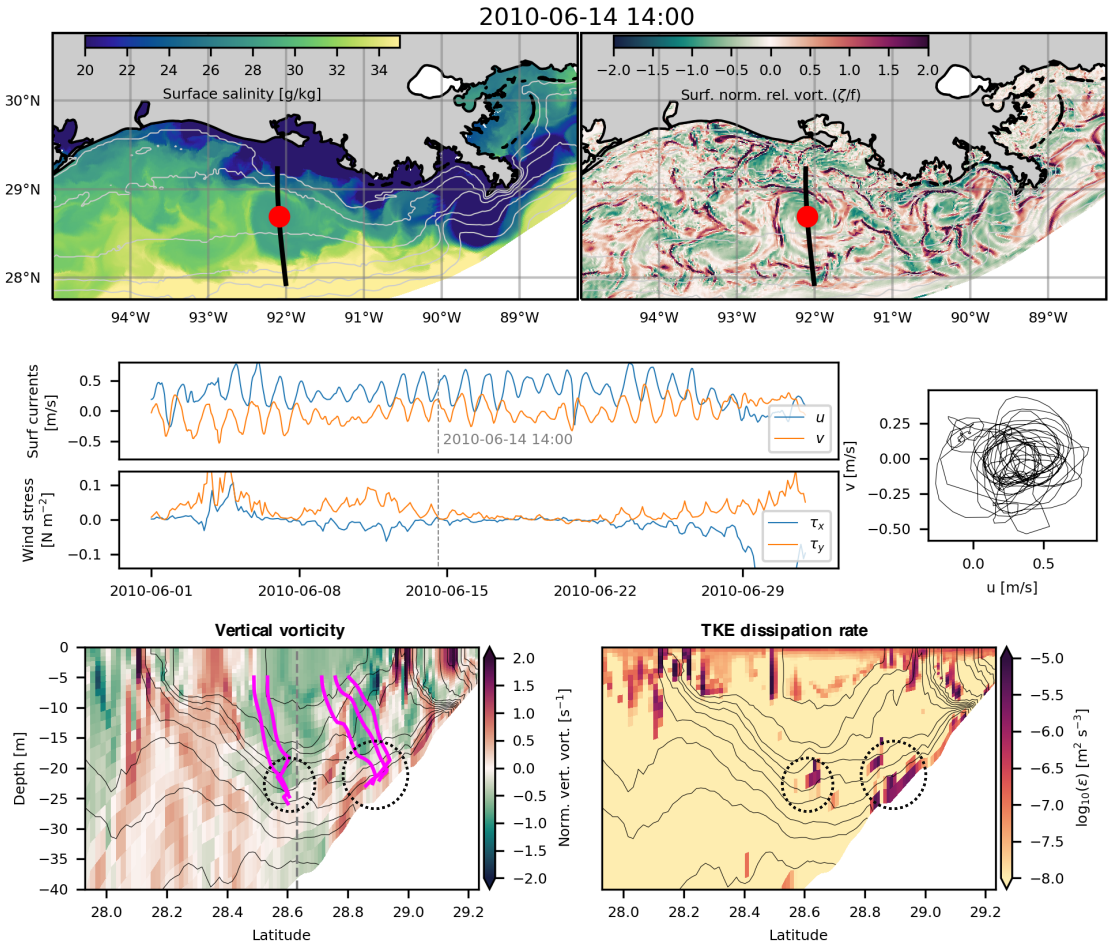

Figure 3.10: (top) An example of the surface salinity and surface vorticity in 2010 summer, based on the TXLA model. (middle) Time series of the surface currents and surface wind stress (at the red dot) with a hodograph of the currents to the right. (bottom) Eddy transects of the vorticity and TKE dissipation rate (along the black line) with density contours every 1 kg m^{-3}. Vortex center marked by the gray dashed line. NIW rays (magenta lines) with the frequency of f are initiated at $z = -5\ m$. Ray tracing results show that the waves propagate downward in the anti-cyclone, and the rays converge where the interior dissipation is strongest (marked by the black dashed circles).

yields the restoring mechanism of the NIWs within a baroclinic vortex (see Appendix E).

According to the parcel argument in Appendix E, the oscillating frequency σ of a displaced parcel is equal to

$$\sigma = \sqrt{{f^*_{eff}}^2 - 2M^2 S_\delta + N^2 S_\delta^2} = \sqrt{M^2(S_\rho^{-1} S_\delta^2 - 2S_\delta + S_L)}, \tag{3.27}$$

where $S_L \equiv -\frac{\frac{\partial L_b}{\partial r}}{\frac{\partial L_b}{\partial z}} = \frac{{f^*_{eff}}^2}{M^2}$ is the slope of the background absolute angular momentum ($L_b = rV_\theta + \frac{1}{2}fr^2$), $S_\rho = M^2/N^2$ is the isopycnal slope, and S_δ is the slope of the displacement. Fig. 3.11 shows σ as a function of S_δ. σ decreases with increasing S_δ when $S_\delta < S_\rho$ and increases when $S_\delta > S_\rho$. σ reaches the minimum if $S_\delta = S_\rho$, which is

$$\sigma_{min} = \sqrt{M^2(S_L - S_\rho)}; \tag{3.28}$$

σ_{min} depends on the difference between S_L and S_ρ. Moreover, the displacements with $S_\delta = 0$ and $S_\delta = 2S_\rho$ have the same frequency as f^*_{eff} – the motions with the frequency of f^*_{eff} can be purely horizontal oscillations or vertically propagating waves. These results are analogous to the case of the baroclinic jet (Thomas, 2017).

The primary finding of this study is that the curvature effect of a baroclinic vortex can influence the vertical radiation of NIWs and hence alter the trapping depth of the NIWs; particularly, in a baroclinic anti-cyclone, NIWs can be trapped deeper and hence could cause a deeper mixing, compared to the NIWs at a baroclinic jet with anti-cyclonic vorticity.

The effective inertial frequency is modified from $f_{eff} = \sqrt{f(f + \zeta_s)}$ at a baroclinic jet to $f^*_{eff} = \sqrt{(f + 2\zeta_c)(f + \zeta_c + \zeta_s)}$ in a baroclinic vortex. f^*_{eff} contains two modifications: the modification by the total vorticity $\zeta_c + \zeta_s$ altering the net spin of the fluid, and the modification by the curvature vorticity ζ_s altering the net spin of the rotating framework. The minimum frequency of NIWs is modified from $\sigma'_{min} = \sqrt{f_{eff}^2 - M^4/N^2}$ at a baroclinic jet to $\sigma_{min} = \sqrt{{f^*_{eff}}^2 - M^4/N^2}$ in a baroclinic vortex due to the curvature effect. In particular, if the vortex is an anti-cyclone ($\zeta_c < 0$), σ_{min} will be less than σ'_{min} – the minimum frequency of the NIWs is reduced by the

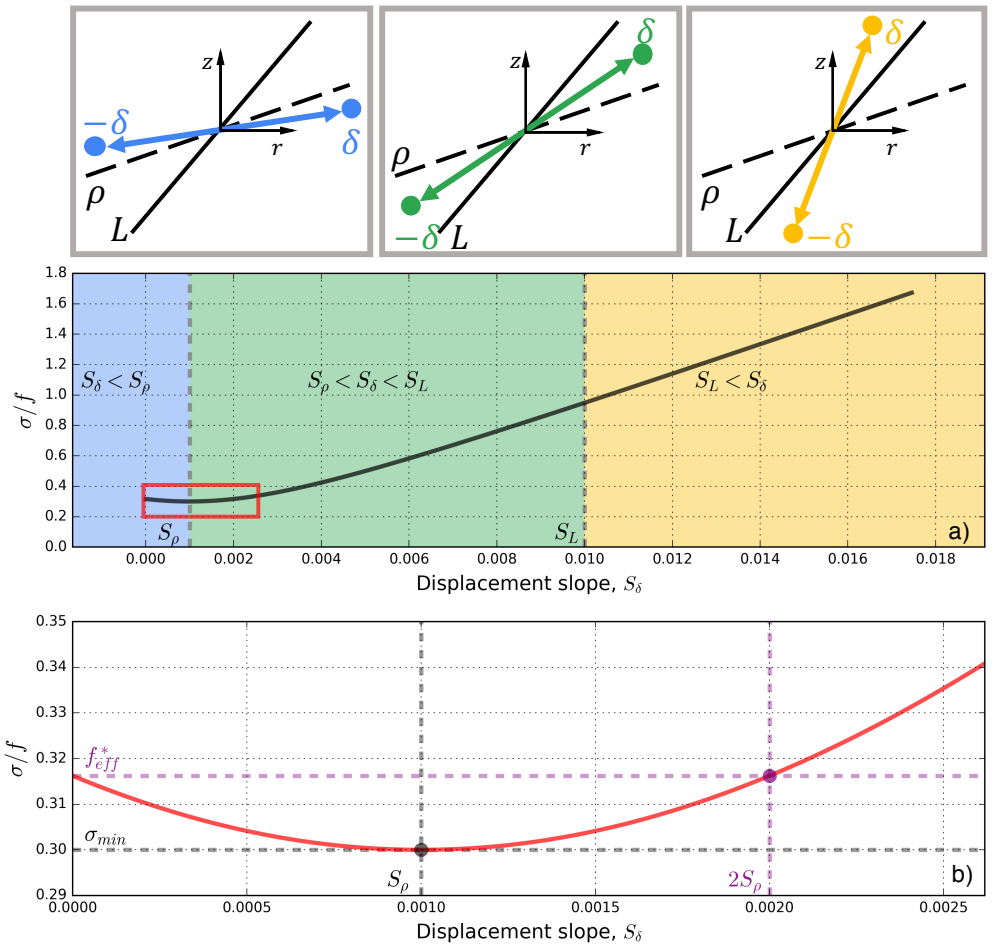

Figure 3.11: (a) Oscillating frequency σ of a displaced fluid parcel as a function of the displacement slope S_δ. The schematics above are corresponding to three scenarios: $S_\delta < S_\rho$, $S_\rho < S_\delta < S_L$, and $S_L < S_\delta$ (δ is displacement, ρ is density, L is absolute angular momentum, $S_L = {f^*_{eff}}^2/M^2$ is slope of L, and $S_\rho = M^2/N^2$ is isopycnal slope). The background field is configured with ${f^*_{eff}}^2 = 10^{-9}\ s^{-2}$, $M^2 = 10^{-7}\ s^{-2}$, and $N^2 = 10^{-4}\ s^{-2}$. (b) Zoomed view of the red box in a).

curvature effect.

The time-dependent Eliassen-Sawyer equation and the wave energy density formula are derived in cylindrical coordinates. The Eliassen-Sawyer equation is numerically solved in an idealized anti-cyclone to illustrate the energy density of the NIWs within a baroclinic vortex. On the other hand, the ray tracing based on the WKB approximation is conducted in the idealized vortex to illustrate the propagation and trapping of the NIWs. The numerical solution is consistent with the ray tracing result. Both the numerical solution and ray tracing result show that the curvature effect of the anti-cyclone extends the propagation area of the NIWs, and the NIWs can be trapped deeper than previously predicted.

A fully non-linear numerically simulation is conducted to simulate the NIWs in the idealized vortex based on the ROMS. The result shows that the curvature-modification theory well predicts the propagation region of the NIWs. Furthermore, the ray tracing is conducted in an anti-cyclone based on a realistic simulation on the Texas-Louisiana shelf with the curvature effect taken into account. The result shows that the NIWs propagate downward and converge in the interior at the base of the vortex, which suggests the wave trapping and wave amplification. Correspondingly, the internal mixing is found to be enhanced at the locations where the wave rays converge. This feature indicates that the bottom water could be periodically ventilated by the trapping of NIWs, which is helpful to interpret the patchy and transient features of summertime bottom hypoxia in the northern Gulf of Mexico.

3.7 Acknowledgments

This chapter is based on a manuscript in preparation, co-authored by Professor Robert Hetland and Professor Leif Thomas at Stanford University. The MCH and TABS data were provided by Professor Steven DiMarco. The code used for numerical calculations was developed by Dr. Daniel Whitt at National Center for Atmospheric Research during his work with Professor Leif Thomas at Stanford University. The support of Veronica Ruiz Xomchuk and Arthur Ramos at Barcelona Supercomputing Center is also gratefully acknowledged. This study is supported by the grant 18-132-000-A673 from Texas General Land Office, grant 2018SP-S-Qu-GIA from Texas Sea Grant,

and a scholarship from China Scholarship Council.

4. TEMPORAL RESOLUTION OF WIND FORCING REQUIRED FOR RIVER PLUME SIMULATIONS *

4.1 Introduction

As a typical buoyancy-driven flow in coastal zones, river plumes are of the central importance of understanding coastal ecosystems and environments (Horner-Devine et al., 2015). Rivers transport freshwater, sediments, nutrients, and pollutants from continents to the ocean. Annually, about $4 \times 10^4\ km^3$ of freshwater (one-third of the total precipitation over land) and 12.6 billion metric tons of sediments are transported to the global ocean via rivers (Syvitski et al., 2005; Trenberth et al., 2007). The large input of nutrients stimulates phytoplankton and zooplankton growth, which can give rise to productive fisheries in river plume regions. As a negative consequence, this high productivity, combined with the enhanced stratification, can create hypoxic bottom water under plume regions (Lohrenz et al., 1999; Rabalais et al., 1999; Hetland and DiMarco, 2008). Moreover, the high-nutrient conditions created by the runoff of industrial and agricultural wastes can induce toxic algal blooms, which threaten the communities living in coastal regions and hurt the shellfisheries and other potential industries that rely on clean water (Franks and Anderson, 1992). This chapter will focus on the river plume simulations. Particularly, the temporal resolution of wind forcing required for river plume simulations is explored to provide guidance on selecting wind forcing data.

Wind is a primary forcing agent for the river plume variability. For selecting wind forcing data, there are often two choices, i.e., single-point measurements or atmospheric general circulation model (GCM) data. Wind data from single-point measurements often have higher temporal resolutions (sampling rates are often higher than hourly) compared to the GCM data. To use this will be reasonable if the spatial scale of the simulation region is smaller than, or comparable with, the wind decorrelation scale (Hetland and DiMarco, 2012a). However, it will not be a good choice for the situations where the spatial structure of wind matters even though the simulation area is

*This chapter is a reprint of material published in the Journal of Geophysical Research - Oceans with permission.

small. For instance, the Pearl River plume region over the northern South China Sea shelf is frequently affected by typhoons, leading single-point measurements to miss the phase information of passing fronts. Therefore, under some circumstances, we have to use GCM data, which possess lower temporal resolution but with spatial information. This is a trade-off between resolving finer spatial structure or high-frequency temporal variability, and we simply do not know which one is more important, because it is not clear which temporal resolution is needed for simulating river plumes.

Wind data from atmospheric GCMs can be found in multiple temporal resolutions. There are numerous meteorologic reanalysis and forecast products. The associated institutions include the European Center for Medium-Range Weather Forecasts (ECMWF), National Centers for Environmental simulation (NCEP) of National Oceanic and Atmospheric Administration (NOAA), and National Aeronautics and Space Administration (NASA). For reanalysis data products, JRA-25 (Onogi et al., 2007) and NCEP-DOE Reanalysis 2 (Kanamitsu et al., 2002) provide 6-hourly sea surface wind data, ERA-Interim (Simmons et al., 2007) and NCEP NARR (Mesinger et al., 2006) provide 3-hourly wind data, and NASA MERRA (Rienecker et al., 2011) and NCEP CFSR (Saha et al., 2010) provide hourly wind data. For forecast data products, GFS/NOAA provides 3-hour surface wind forecast up to +240 hours (NCEP, 2003), and ECMWF forecast provides 3-hourly data up to +144 hours and 6-hourly data from +150 to +240 hours (Andersson, 2015). A data product with a lower temporal resolution may have a better performance on reproducing or predicting winds in a specific region compared to the ones with higher resolutions. In this situation, we have to use the wind data with the relatively low temporal resolution, but we simply do not know how important is the missing high-frequency information.

The goal of this chapter is to quantify the temporal resolution of wind forcing required for accurate river plume simulations. In particular, the problems mentioned above will be addressed by evaluating the influence of missing high-frequency wind information in a series of idealized numerical simulations. The simulation errors will be examined in three aspects: the plume extent, freshwater transport, and plume structure in salinity coordinates. The factor controlling the plume

simulation errors will be explored, and subsequently, suggestions on properly selecting wind forcing for river plume simulations will be provided.

4.2 Methods

4.2.1 Idealized Numerical Model

The hydrodynamic model employed in this study is the version 3.8 of Regional Ocean Modeling System (ROMS) (Shchepetkin and McWilliams, 2005). ROMS is a free-surface, hydrostatic, primitive equation ocean model using orthogonal curvilinear coordinates in the horizontal direction and S-coordinate in the vertical direction. The model domain is a uniformly sloping shelf with a straight estuary attached (Fig 4.1a). The size of the shelf region is approximately 100 km (across-shore) $\times$ 360 km (along-shore), and the depth ranges from 10 m to 100 m offshore. The estuary is 20 km long and 1 km wide and has a parabolic bathymetry ranging from 3 m to 10 m in the cross-channel direction. Model grid focuses on the estuary and the adjoining shelf region, with the finest resolution of 200 m $\times$ 200 m. Resolution decreases away from the outflow region and is coarsest at the edges of the domain. Model grid and resolution in the river plume region are shown in Fig 4.1b. In the vertical direction, the model has 20 layers with fine resolution at the surface ($< 1\ m$ in the upper 5 m). The s-coordinate parameters are set to $V_{transform} = 2,\ V_{stretching} = 4,\ \theta_S = 5.0,\ \theta_B = 0.01$, and $T_{cline} = 5.0$. Flow is initially at rest, and initial temperature and salinity are set to uniformly 25°C and 32 psu, respectively. River discharge has a constant rate of 1000 m^3s^{-1} with the temperature of 25°C and the salinity of 0 psu. $k - \epsilon$ turbulence closure scheme is used to calculate vertical mixing, and Canuto A stability function formulation is applied (Umlauf and Burchard, 2003; Canuto et al., 2001). This idealized model with similar configurations has been used in previous, general studies to understand the mixing within river plumes, such as Hetland (2005) and Cole and Hetland (2016). Consequently, the model is capable of capturing the main features of a wind-dominated, surface-advected river plume, and supports the associated plume dynamics in a variety of situations.

The momentum forcing is along-shore and spatially uniform and has no across-shore compo-

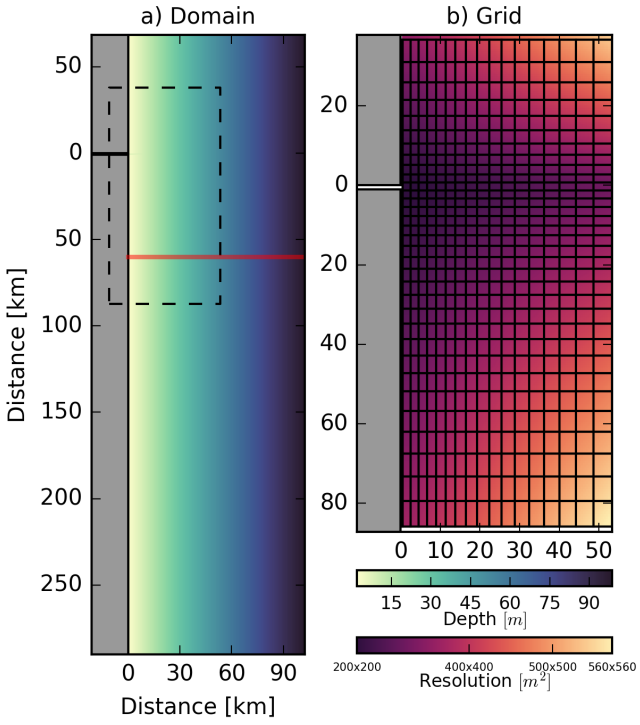

Figure 4.1: a) Idealized model domain with bathymetry in color. Dashed box encloses the region shown to the right, and red line marks a section at 60 km downstream. b) Model grid (lines) and resolution (color). Black lines mark every 10 grid cells. Reprinted with permission from Qu and Hetland (2019).

nent (see Section 4.2.2). The reason for excluding the across-shore component is that the structure and position of a river plume over a shelf are dominated by the along-shore winds (upwelling and downwelling winds) through the Ekman transport (Fong and Geyer, 2001; Moffat and Lentz, 2012). The across-shore winds could merely affect the across-shore transport in an unstratified inner shelf, where the surface and bottom Ekman layers can interact with each other so that the fluid is friction-dominated (Tilburg, 2003). But, in this study, we focus on the river plumes on a stratified, broad shelf, so the across-shore transport due to the across-shore winds should be a secondary effect in this scenario.

4.2.2 Wind Forcing Data

Surface wind data are gathered from the Texas Automated Buoy System (TABS) buoy B, which is located on the Texas-Louisiana shelf and in the Mississippi River plume region (Fig 4.2a). We use the data in August 2014, which possess a sampling rate of 30 minutes. Fig 4.2b shows the observed wind speed in the zonal direction, positive eastward. The wind speed approximately ranges from -10 m/s to 8 m/s, which is a typical wind condition in this region (Jebson, 2007). This observational data are used as a reference to reconstruct a near-realistic wind forcing for idealized numerical experiments. The near-realistic wind is required to be as realistic as possible to keep the natural characters of the observed wind, yet idealized enough to clearly highlight the relation between temporal resolutions and simulation errors.

Fast Fourier Transformation (FFT) is used to decompose the observed wind time series, and the associated spectrum is shown in Fig 4.2a. In logarithmic coordinates, the energy spectrum increases with increasing periods in an approximately linear trend. The linear regression of the spectrum is shown in Fig 4.2a. Correlation between the regression and the raw spectrum is $r^2 = 0.85$, and the two-sided T-test shows that they are statistically indistinguishable with $p = 0.48$. A near-realistic wind is reconstructed by inverse FFT using the linear-regressed spectrum and the original FFT phases. Fig 4.2b shows the comparison between the reconstructed and the original wind data; we can see that the main features of the original wind are still preserved. This near-realistic wind is used to force the idealized model to build the control run. Furthermore, in order to quantify simulation errors caused by temporal subsampling, the near-realistic wind is low-pass filtered (see Section 4.2.3) to generate a series of winds with various temporal resolutions, and subsequently the simulations forced by the filtered winds are compared with the control run.

4.2.3 Low-Pass Filters

Two types of low-pass filters are used in this study. One is the **attenuated amplitude** filter, a low-pass filter that passes signals with frequencies lower than a cutoff frequency and attenuates amplitudes of signals with frequencies higher than the cutoff frequency. The other one is the

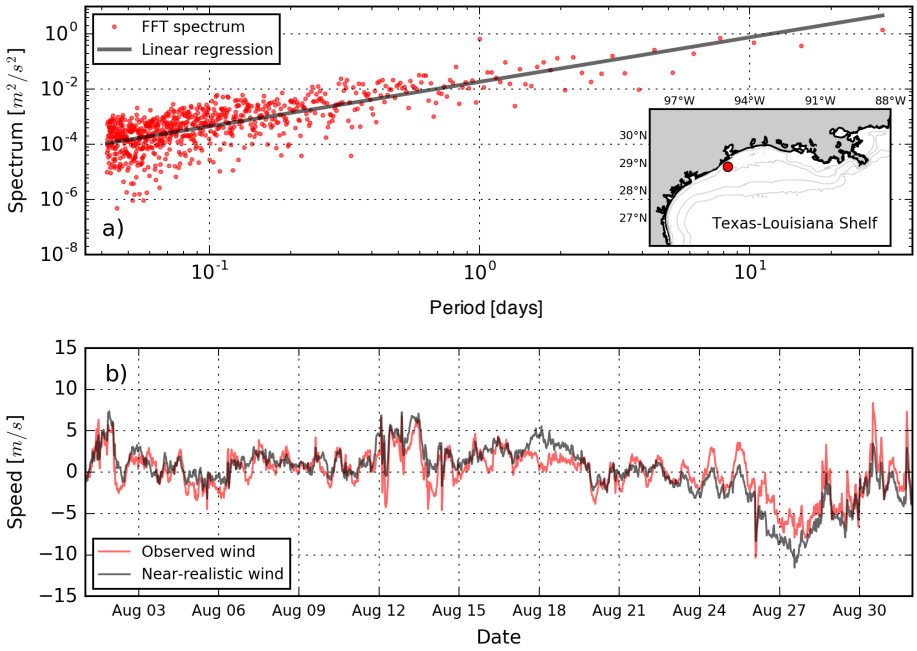

Figure 4.2: a) FFT spectrum of the surface wind speed observed at TABS Buoy B and the associated linear regression. b) Comparison between the observed and reconstructed winds. Only the zonal component of the wind data is exhibited, and eastward is positive. Lower-right panel in a) shows the buoy location (red circle). 10, 20, 50, and 100 m isobath contours are marked. Reprinted with permission from Qu and Hetland (2019).

randomized phase filter, a low-pass filter that passes low-frequency signals in terms of both amplitudes and phases, while preserves the amplitudes of high-frequency signals, but randomizes the phases of high-frequency signals.

Applying the attenuated amplitude filter (see the upper panels of Fig 4.3), the portion of the FFT spectrum with frequencies lower than the cutoff frequency is preserved, while the high-frequency proportion of the spectrum above the cutoff frequency is set to zero amplitude. A new wind time series is reconstructed by inverting the modified spectrum with the corresponding proportion of the FFT phases. On the other hand, applying the randomized phase filter (see the lower panels of Fig 4.3), the entire spectrum is preserved, while the phases with frequencies lower than the cutoff frequency are preserved, but the high-frequency proportion of the phases above the cutoff frequency are randomized. A new wind time series is reconstructed by inverting the original spectrum with the modified phases. In order to more effectively show the cutoff points, cutoff frequencies will be expressed as cutoff periods for the rest article, which are proportional to the reciprocal of the cutoff frequencies.

4.2.4 Metrics

The metrics to evaluate river plume simulation errors are the plume extent distance, freshwater transport, and plume structure in salinity coordinates. Plume extent distance, D, is defined as the maximum surface offshore extent of 28 psu isohaline and used to characterize the cross-shore freshwater transport by a plume. Root-Mean-Square (RMS) error is used to evaluate simulation errors. RMS error of plume extent, RMS_D, is given by

$$RMS_D = \sqrt{\frac{1}{N}\sum_{n=1}^{N}[D^E(t_n) - D^C(t_n)]^2}\,, \tag{4.1}$$

where $D^E(t_n)$ and $D^C(t_n)$ are the plume extent of a filtered run and the control run, respectively, and $t_n,\ n = 1, 2, ..., N$, are the output time points. Analogously, RMS error of surface salinity,

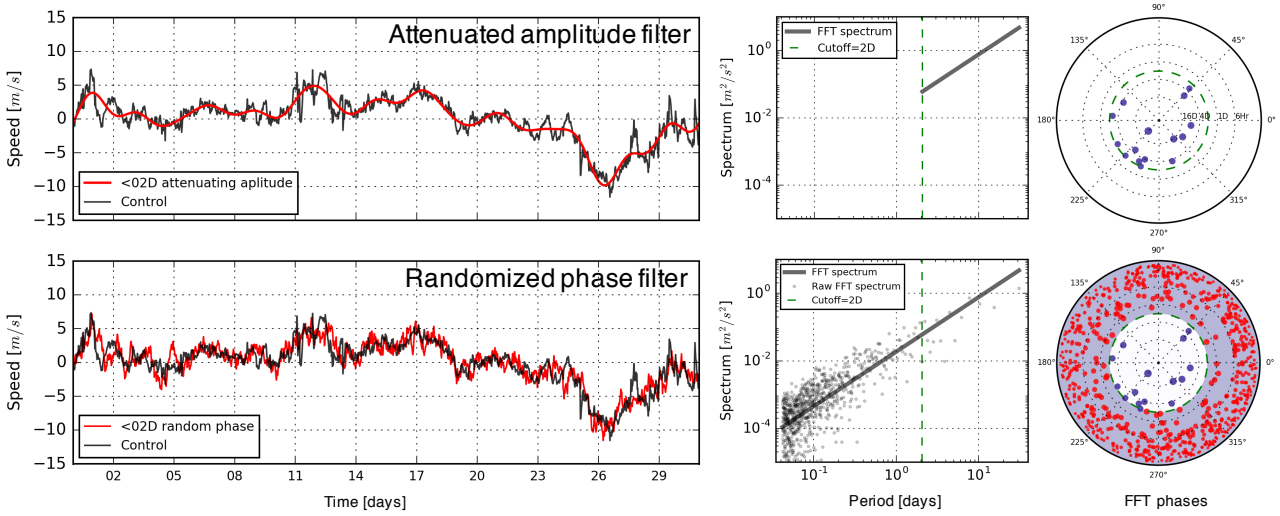

Figure 4.3: Examples of the attenuated amplitude filter (upper) and randomized phase filter (lower) outputs with the FFT spectra and phases to the right. Non-filtered and filtered winds are marked by gray lines and red lines. Cutoff period is set to 2 days marked by dashed green lines in the spectrum and phase plots. In the spectrum plots, gray lines represent the idealized spectra, and gray dots represent the raw spectrum. In the phase plots, 16 days, 4 days, 1 day, and 6 hours are marked by dashed gray lines, and size of a phase dot represents the amplitude of the corresponding signal. Reprinted with permission from Qu and Hetland (2019).

$RMS_S(x,y)$, is given by

$$RMS_S(x,y) = \sqrt{\frac{1}{N}\sum_{n=1}^{N}[S^E(x,y,t_n) - S^C(x,y,t_n)]^2}\ , \tag{4.2}$$

where $S^E(x,y,t)$ and $S^C(x,y,t)$ are the surface salinity of a filtered run and the control run, respectively.

Freshwater transport, T, is defined as the transport across the 60 km, down-coast section (marked in Fig 4.1) and used to characterize plume along-shore transport. The transport is defined as the freshwater content within the total seawater transport, relative to the background salinity S_0 (32 psu), which is expressed as

$$T(t) = \int\int_A \frac{S_0 - S(x,z,t)}{S_0}\, v(x,z,t)\, dxdz\ , \tag{4.3}$$

where $S(x, z, t)$ is the salinity at the section, $v(x, z, t)$ is the across-section velocity, and A is the section area. RMS error of freshwater transport, RMS_T, is given by

$$RMS_T = \sqrt{\frac{1}{N}\sum_{n=1}^{N}[T^E(t_n) - T^C(t_n)]^2}\ , \tag{4.4}$$

where $T^E(t_n)$ and $T^C(t_n)$ are the freshwater transport of a filtered run and the control run, respectively.

In contrast to Cartesian coordinates, salinity coordinates have the advantage of following a river plume and tracking freshwater distribution as the plume moves and mixes with ambient water (Hetland, 2005). The key link to describe a river plume in salinity coordinates is the freshwater content, $V(S)$, as a function of salinity, S. Given a volume where salinity is less than a reference salinity S_r, the freshwater content relative to S_r, $V(S_r)$, is defined by the integral of the freshwater fraction in this volume relative to the background salinity S_0, which is expressed as

$$V(S_r) = \int\int\int_{S<S_r} \frac{S_0 - S(x, y, z)}{S_0}\, dxdydz\ , \tag{4.5}$$

where $S(x, y, z)$ is the 3-dimensional salinity distribution in Cartesian coordinates. Consequently, the structure of a plume in salinity coordinates can be described by the freshwater distribution function $V'(S) = \frac{dV(S)}{dS}$, which is the salinity derivative of the freshwater content $V(S)$. Although the freshwater distribution function could not provide the stratification information of a river plume in a Cartesian reference frame (e.g. the stratification or plume depth at a specific location), it can indicate the overall mixing status of the plume and track the freshwater entrainment and transfer across salinity classes due to a variety of mixing processes within the plume. Hetland (2005) demonstrates its capability on tracking the changes of the stratification status when the winds shift between upwelling and downwelling phases; this suggests that the freshwater distribution is effective to quantify the wind-induced mixing effects on river plume structures and hence can be used as a metric to evaluate the simulation errors caused by subsampling winds.

4.3 Results

4.3.1 Comparative Experiments

Comparative experiments are conducted to examine the relative effects of the low- and high-frequency wind components on river plume variability. There are three groups of experiments: the control run, randomized low-frequency group (3 ensemble members), and randomized high-frequency group (3 ensemble members). All model settings except wind forcing are the same across all three groups. The wind forcing in the control run is the near-realistic wind shown in Fig 4.2b. In the randomized low-frequency group, the winds have the same FFT spectrum as the wind in the control run, but FFT phases of the winds are randomized at periods longer than 1 day (see Fig 4.4b). Analogously, in the randomized high-frequency group, the FFT spectra are the same, but the FFT phases with periods shorter than 1 day are randomized (see Fig 4.4c). The randomized winds are compared to the near-realistic winds in Fig 4.4d and 4.4e.

According to the surface salinity snapshots (not shown), the plumes of the randomized low-frequency group are diverse, and the salinity structures are different from the control run. In contrast, the plumes of the randomized high-frequency group are similar, and the salinity structures are consistent with the control run. Surface salinity RMS errors, $RMS_S(x, y)$, of the randomized low- and high-frequency groups are calculated based on Eq. (4.2) and shown in Fig 4.5; the low-frequency group has generally larger RMS errors than the high-frequency group, especially in the bulge and far-field regions. Moreover, the time-averaged 28 psu isohalines of the randomized low-frequency group are more divergent from the control run than the randomized high-frequency group; this also confirms that the low-frequency group are more deviated from the control run. Consequently, it can be inferred that river plumes are strongly influenced by low-frequency components in wind rather than high-frequency components.

In the phase setting of the randomized high-frequency group (see Fig 4.4c), only 4% of the FFT phases are original, other 96% randomized. However, the surface salinity structure is successfully reproduced. In contrast, 96% of the FFT phases are preserved originally in the phase setting of

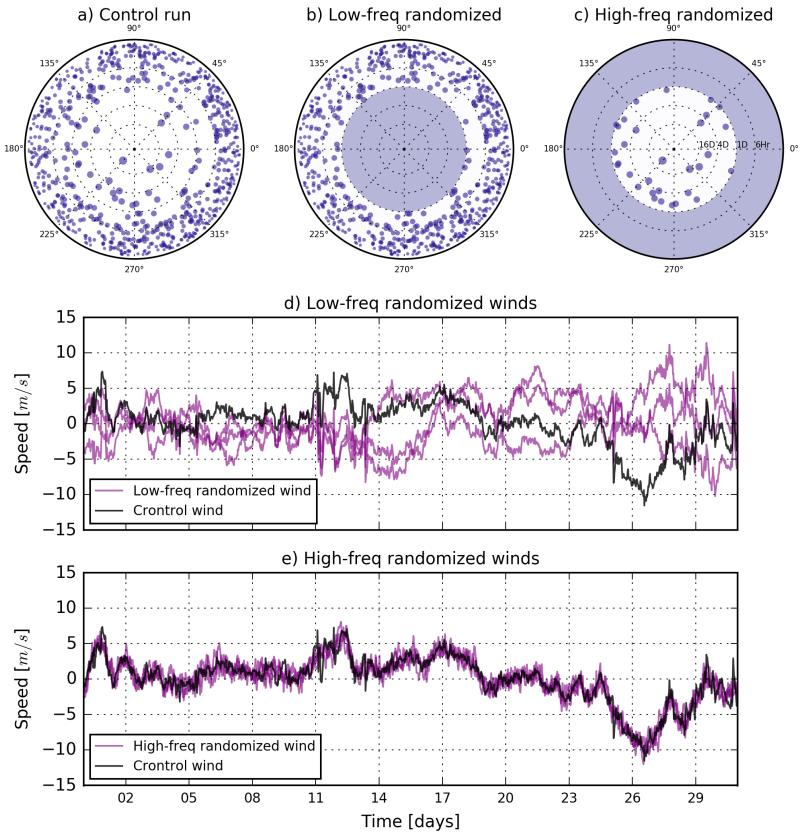

Figure 4.4: a) FFT phases of the near-realistic wind. b) and c) are the phases of the randomized low-frequency and high-frequency groups, respectively. Phases at purple areas are randomized. 16 days, 4 days, 1 day, and 6 hours are marked by dashed gray lines. Size of a phase dot represents the amplitude of the corresponding signal. d) and e) show the comparisons between the randomized winds and the near-realistic wind in those two groups. Reprinted with permission from Qu and Hetland (2019).

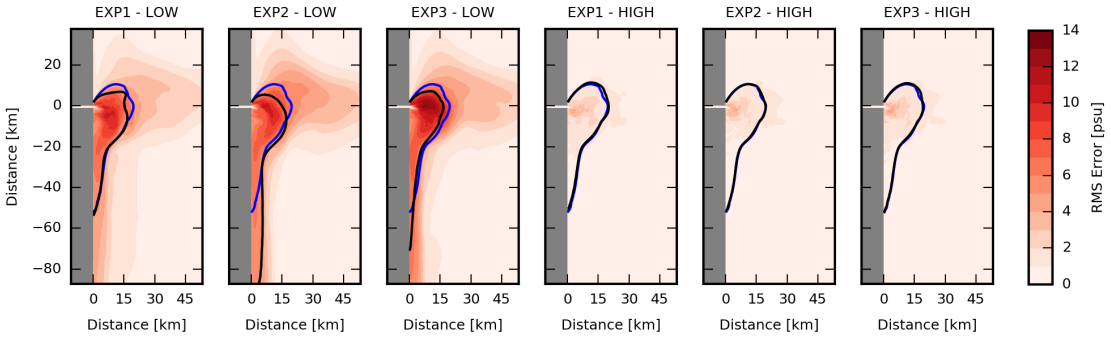

Figure 4.5: Surface salinity RMS errors, $RMS_S(x, y)$, of the randomized low-frequency and high-frequency groups. Blue and black contours represent the time-averaged 28 psu contours of the control run and ensemble simulations, respectively. Reprinted with permission from Qu and Hetland (2019).

the randomized low-frequency group (see Fig 4.4b), but the plumes are very different from the control run. The reason seems to be related to the fact that the low-frequency components have much higher energy than the high-frequency components (see Fig 4.2a); these experiments lead to the hypothesis that the amount of the missing FFT components might not be the dominant factor controlling simulation errors, but the fraction of the missing energy is.

4.3.2 Low-Pass Filter Experiments

In the experiment assocaited with the low-pass attenuated amplitude filter, the wind forcing data are a series of filtered winds – the winds created by applying the low-pass attenuated amplitude filter on the wind of the control run. The cutoff periods are: 3 hours, 6 hours, 12 hours, 18 hours, 24 hours, 35 hours, 2 days, 3 days, 4 days, 5 days, 6 days, 8 days, 10 days, and 16 days. Other model settings are the same as the control run. River plume simulation errors are examined using the metrics of plume extent and freshwater transport.

Surface salinity RMS errors, $RMS_S(x, y)$, of the cutoff runs are shown in Fig 4.6a. Compared to the surface salinity pattern of the control run (upper-left panel of Fig 4.6a), we can see that the large errors are mainly located at the plume bulge region, and the errors significantly decrease with decreasing cutoff periods. Also, the time-averaged 28 psu isohalines of the cutoff runs are compared with the control run, as shown in Fig 4.6a. The contours of the cutoff runs converge to the control run with the decreasing cutoff periods. RMS errors of the plume extent, RMS_D, and freshwater transport, RMS_T, are shown in Fig 4.6b and 4.6c, respectively. Both RMS errors significantly decrease with decreasing cutoff periods. RMS_D decreases approximately from 10 km to 0.5 km, and RMS_T decreases approximately from 400 m^3s^{-1} to 40 m^3s^{-1}.

In the experiment assocaited with the low-pass randomized phase filter, the wind forcing data are created by applying the randomized filter on the wind forcing of the control run. One statistical advantage of the randomized filter is generating ensemble members for a given cutoff period by creating randomized phases. There are 12 ensemble members for each cutoff run. The cutoff periods are the same as used in the attenuated amplitude filter experiment. Other model settings are the same as the control run. In addition, a max error run is set up, in which there are also 12

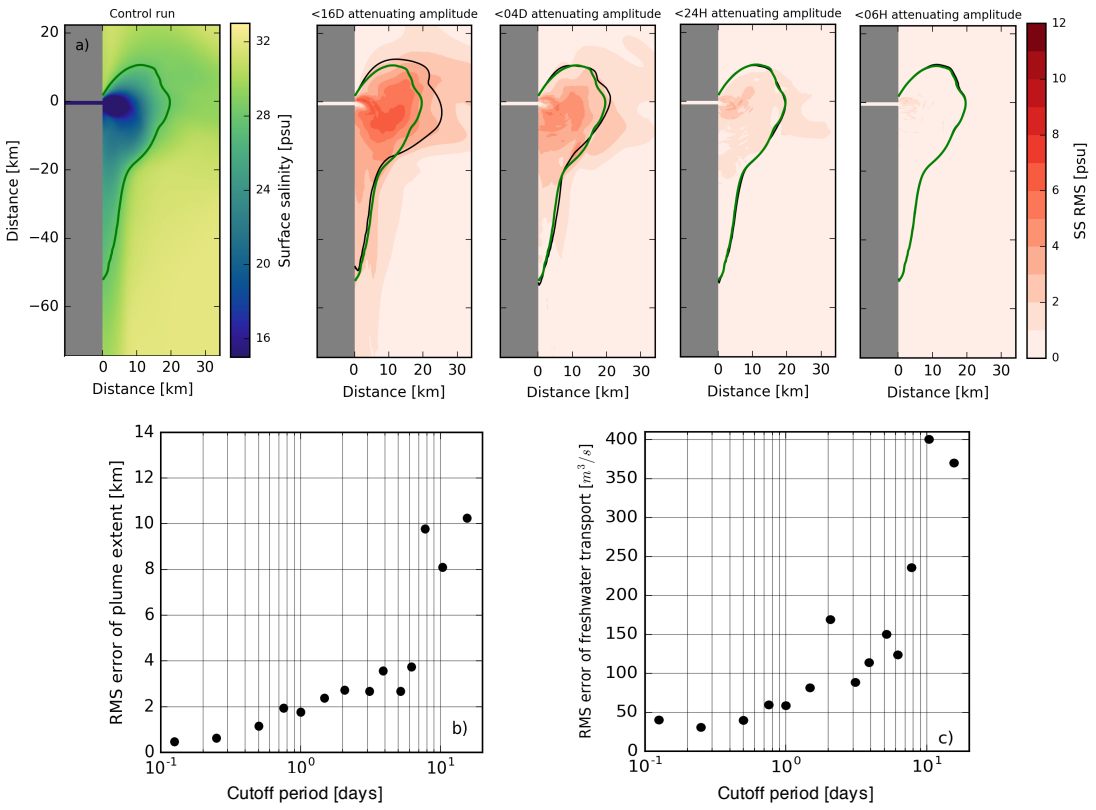

Figure 4.6: a) Surface salinity RMS errors, $RMS_S(x, y)$, of the low-pass attenuated amplitude filter experiment. Time-averaged surface salinity of the control run is shown in the upper-left panel. Green and black contours represent the time-averaged 28 psu contours in the control run and the cutoff runs, respectively. b) Plume extent RMS errors, RMS_D, as a function of the cutoff period. c) Freshwater transport RMS errors, RMS_T, as a function of the cutoff period. Reprinted with permission from Qu and Hetland (2019).

ensemble members, but the wind forcing of each member is created using a totally randomized phase.

Surface salinity RMS errors, $RMS_S(x, y)$, of the max error run and the cutoff runs are shown in Fig 4.7a. Instead of exhibiting the error of each ensemble member, ensemble-averaged RMS error, $\overline{RMS_S}$, is displayed; that is defined by $\overline{RMS_S}(x, y) = \frac{1}{M} \sum_{m=1}^{M} RMS_S^m(x, y)$, where $RMS_S^m(x, y)$ is the surface salinity RMS error of the m^{th} member, and $M = 12$ is the total number of the ensemble members. The result shows that the significant errors are also mainly located in the plume bulge regions, which is consistent with the result of the attenuated amplitude filter experiment. The

max error run has the largest error reaching 12 psu, and the errors of the cutoff runs significantly decrease with decreasing cutoff periods. Time-averaged 28 psu isohalines of all ensemble members are compared with the one of the control run (see Fig 4.7a). The ensemble contours converge to the control run with decreasing cutoff periods.

Ensemble-averaged RMS errors of the plume extent, $\overline{RMS_D}$, and freshwater transport, $\overline{RMS_T}$, are shown in Fig 4.7b and 4.7c, respectively. $\overline{RMS_D}$ and $\overline{RMS_T}$ are defined by $\overline{RMS_D} = \frac{1}{M}\sum_{m=1}^{M} RMS_D^m$ and $\overline{RMS_T} = \frac{1}{M}\sum_{m=1}^{M} RMS_T^m$, where RMS_D^m and RMS_T^m are the RMS errors of the m^{th} member. Compared to the results of the attenuated amplitude filter experiment (Fig 4.6b and 4.6c), $\overline{RMS_D}$ and $\overline{RMS_T}$ also significantly decrease with decreasing cutoff periods in similar trends. $\overline{RMS_D}$ varies more continuously than RMS_D in the attenuated amplitude filter experiment. Moreover, $\overline{RMS_D}$ and $\overline{RMS_T}$ have similar variation ranges compared to RMS_D and RMS_T of the attenuated amplitude filter experiment; $\overline{RMS_D}$ decreases approximately from 13 km to 0.4 km, and $\overline{RMS_D}$ decreases approximately from 340 m^3s^{-1} to 40 m^3s^{-1}.

4.3.3 Comparison of Two Filter Experiments

Both the attenuated amplitude filter experiment and the randomized phase filter experiment show that simulation errors decrease with decreasing cutoff periods (see Fig 4.6b/c and Fig 4.7b/c). Although two types of filter experiments show similar decreasing trends, some difference still exists between the results. Fig 4.8a shows the comparison of plume extent RMS errors (RMS_D versus $\overline{RMS_D}$), and Fig 4.8b shows the comparison of of freshwater transport RMS errors (RMS_T versus $\overline{RMS_T}$).

In Fig 4.8a, the errors associated with the cutoff periods shorter than 3 days are nearly identical. However, for the longer cutoff periods, the randomized phase filter runs have higher errors than those of the attenuated amplitude filter runs. The reason for "3 days" can be explained using the classic Ekman transport theory. Given that the plume extent is defined in the plume bulge region, the Ekman transport in the plume bulge is explored. To be consistent with the definition of the plume extent, the definition of the plume bulge is also based on the criterion of 28 psu, which is the volume where salinity is less than 28 psu. The across-shore section through the center of the

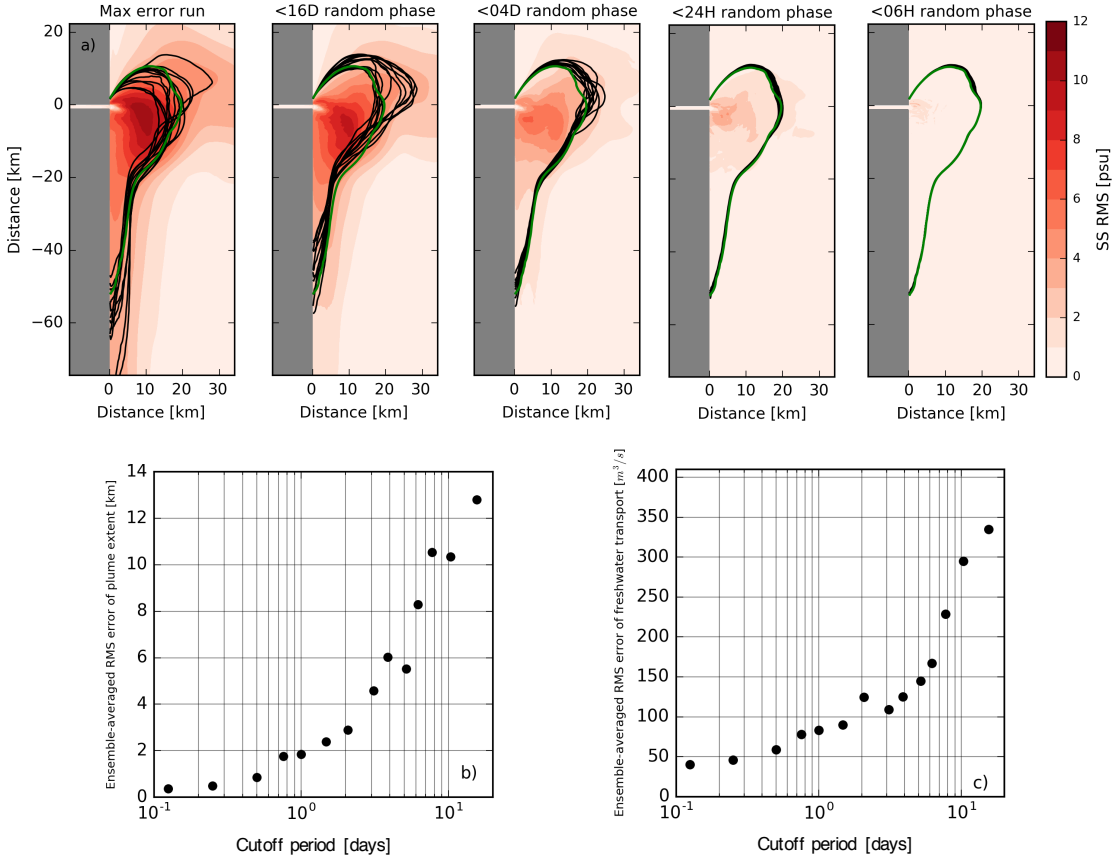

Figure 4.7: a) Ensemble-averaged surface salinity RMS errors, $\overline{RMS_S}(x, y)$, of the low-pass randomized phase filter experiment. Green and black contours represent the time-averaged 28 psu contours of the control run and the ensemble members, respectively. b) Ensemble-averaged RMS errors of plume extent, $\overline{RMS_D}$, as a function of the cutoff period. c) Ensemble-averaged RMS errors of freshwater transport, $\overline{RMS_T}$, as a function of the cutoff period. Reprinted with permission from Qu and Hetland (2019).

time-averaged bulge in the control run is shown in Fig 4.8c.

Consider the plume bulge as a layer of freshwater, with density ρ_0 and thickness of h_f, overlaying denser oceanic water. In the freshwater layer, the Ekman transport caused by a wind stress τ can be given by

$$\overline{u}h_f = \frac{\tau}{f\rho_0} , \tag{4.6}$$

where $\overline{u}$ is the depth-averaged velocity in the freshwater layer and f is the Coriolis parameter. The across-shore velocity $\overline{u}$ can be estimated as $\frac{\Delta x}{\Delta t}$, where Δt is the duration of the wind and Δx is the moving distance of a fluid parcel. Therefore, the across-shore moving distance Δx can be expressed as a function of the wind duration Δt,

$$\Delta x = \frac{\tau}{f\rho_0 h_f}\Delta t . \tag{4.7}$$

The difference of wind forcing between two experiments is that a randomized phase filtered wind has additional, randomized high-frequency fluctuations compared to an attenuated amplitude filtered wind using the same cutoff period. If the additional wind fluctuations could cause a moving distance Δx larger than the bulge width W, the spatial dimension of the bulge would be changed, and hence the randomized phase filtered wind can cause extra errors compared to the attenuated amplitude filtered wind. Otherwise, if the additional fluctuations cause a Δx smaller than W, the spatial dimension of the bulge would not be changed since the motion is confined within the bulge, and hence the randomized phase filtered wind would cause a similar error as the attenuated amplitude filtered wind; this implies a constraint of the wind duration Δt to yield similar errors in two experiments,

$$\Delta t \ < \ \frac{f\rho_0 h_f}{\tau} W . \tag{4.8}$$

According to the wind record (see Fig 4.2b), the mean wind speed U_W is 2.0 m s^{-1} such that the mean wind stress is $\tau = \rho_a C_D U_W^2 = 4.9 \times 10^{-3}$ N m^{-2}, where $\rho_a = 1.225$ kg m^{-3} is the air density and $C_D = 0.0015$ is the drag coefficient (Cushman-Roisin and Beckers, 2011). Based on the spatial dimension of the plume bulge in the control run (see Fig 4.8c), the plume width W

is approximately 20 km, and the thickness of the upper layer is approximately 1 m (horizontal-averaged). Given that f is 10^{-4} s^{-1} and ρ_0 is 10^3 kg m^{-3}, applying Eq. 4.8, yields $\Delta t < 3.15$ days; this indicates that the randomized components with periods shorter than 3 days in the randomized phase filtered wind can not cause extra error compared to the attenuated amplitude filtered wind. In other words, two filtered winds with the cutoff periods shorter than 3 days will have similar errors, even if the randomized phase filtered wind has additional random high-frequency components. For the longer cutoff periods, the random components in the randomized phase filtered winds can cause large across-shore motions so that spatial structures of plume bulges can be further modified and create larger $\overline{RMS_D}$; this explains the larger $\overline{RMS_D}$ after the 3 days cutoff.

In Fig 4.8b, the RMS errors of two experiments are nearly 1:1, especially when the cutoff period is smaller than 3 days. In this cutoff period range, the attenuated amplitude filter experiment has nearly identical errors as the randomized phase filter experiment, in terms of both plume extent and freshwater transport; it implies that the error caused by missing high-frequency components is nearly 1:1 to the error caused by adding random perturbations at this high-frequency band. Furthermore, the cutoff period that is shorter than 3 days is equivalent to the temporal resolution that is finer than 1.5 days. This resolution range is where the temporal resolutions of atmospheric GCM data and single-point measurements are located. Hence, the randomized phase filter experiment would be capable of quantifying the simulation errors caused by subsampling.

4.3.4 Quantifying River Plume Simulation Errors

The freshwater distribution function in salinity coordinates can provide a comprehensive description of the structure of a river plume (Hetland, 2005). On the other hand, the randomized phase filter experiment can provide more statistical information by setting up ensemble runs. Therefore, we choose the freshwater distribution in the randomized phase filter experiment as the metric to quantify the error rate for a river plume simulation.

Time-averaged freshwater distribution functions of the control run, max error run, and cutoff runs are shown in Fig 4.9a. As discussed by Hetland (2005), freshwater is concentrated at high-salinity classes. As the cutoff period decreases, the results of the ensemble runs converge to the

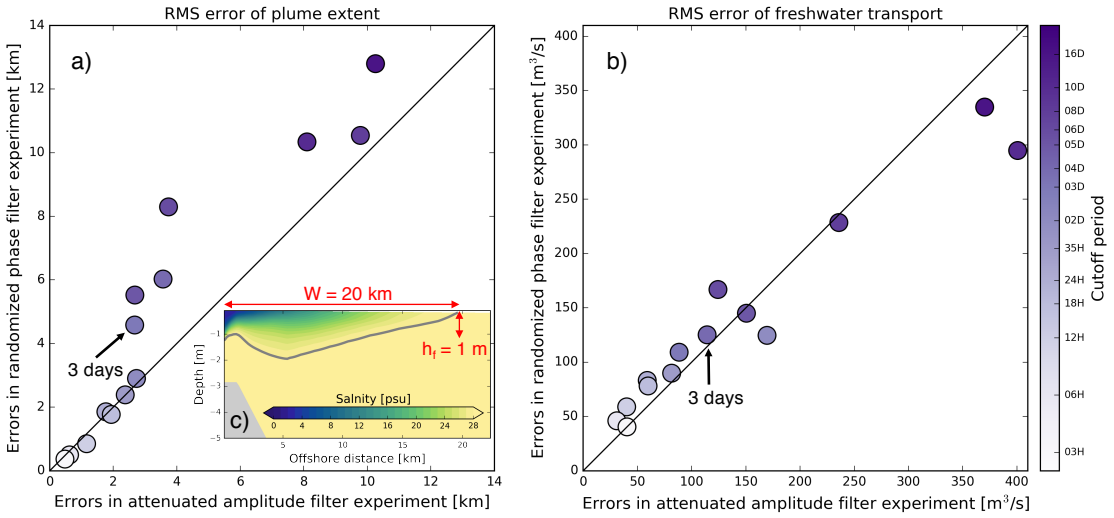

Figure 4.8: a) RMS_D versus $\overline{RMS_D}$. b) RMS_T versus $\overline{RMS_T}$. Color represents cutoff period, and grey lines are 1:1 lines. c) Across-shore section through the center of the time-averaged plume bulge in the control run. Grey contour marks the 28 isohaline. Reprinted with permission from Qu and Hetland (2019).

result of the control run. Assuming $V'_m(S)$ is the freshwater distribution function of the m^{th} ensemble member and $\overline{V'}(S)$ is the ensemble mean of all the $V'_m(S)$, the ensemble standard deviation σ of the freshwater distribution is defined as

$$\sigma = \frac{1}{N_S}\sum_{S_r\in\mathbb{S}} STD(S_r) = \frac{1}{N_S}\sum_{S_r\in\mathbb{S}}\sqrt{\frac{1}{M-1}\sum_{m=1}^{M}[V'_m(S_r)-\overline{V'}(S_r)]^2}\,, \tag{4.9}$$

where $S_r \in \mathbb{S}$, $\mathbb{S}$ is a discrete salinity space with N_S elements ranging from 16 to 32 psu, and $M = 12$ is the total number of the ensemble members. $STD(S)$ is the unbiased estimation of standard deviation based on the 12 ensemble members, and it is calculated on each salinity point $S_r \in \mathbb{S}$. Then, $STD(S_r)$ are averaged across all the salinity points $S_r \in \mathbb{S}$ to get the mean ensemble standard deviation σ. Large ensemble standard deviation σ indicates a large plume simulation error, and small σ indicates a small error.

Assuming that σ^{cut} and σ^{max} are the standard deviations of a cutoff run and the max error run,

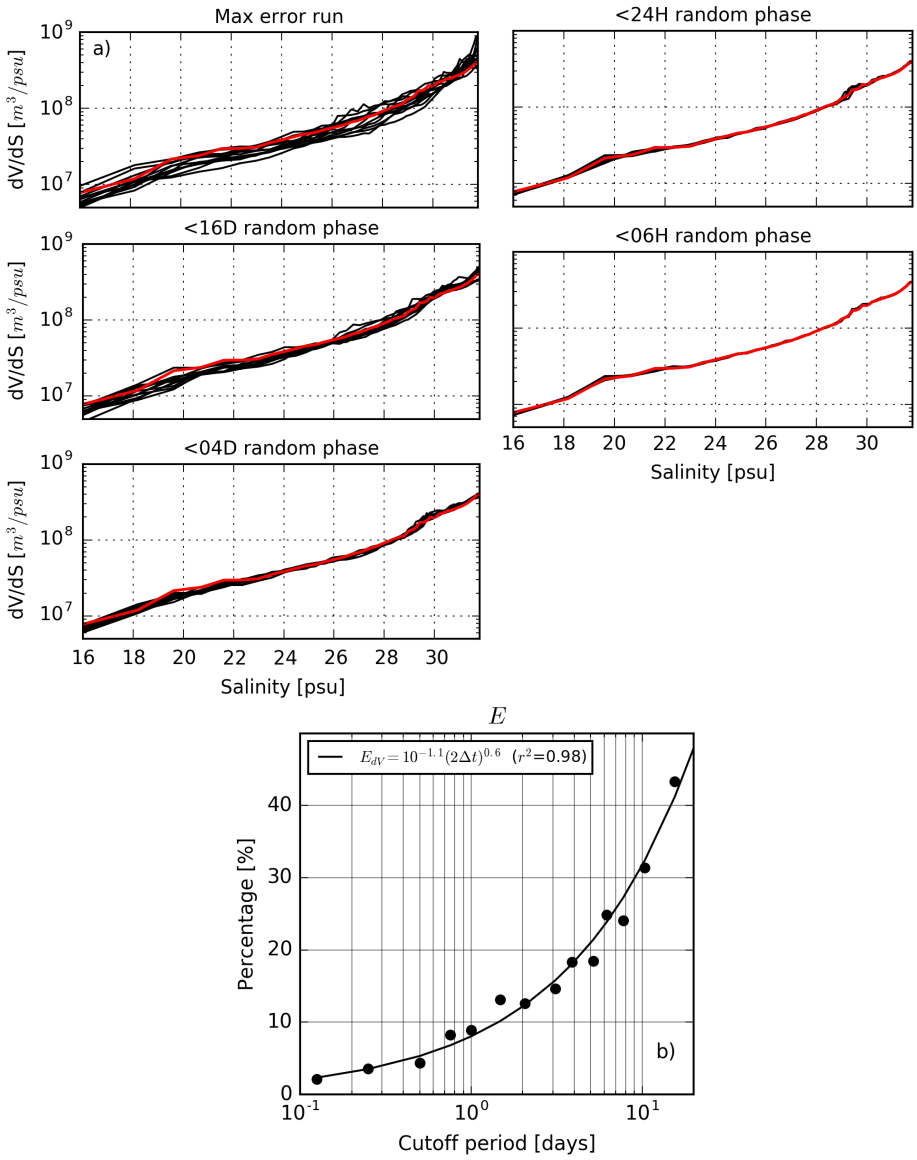

Figure 4.9: a) Freshwater distribution functions, $V'(S) = \frac{dV(S)}{dS}$, in the low-pass randomized phase filter experiment, and red and black lines represent the functions in the control run and the ensemble runs, respectively. b) Simulation error rate, E, as a function of the cutoff period, and black line is the best power function to fit the dots. Reprinted with permission from Qu and Hetland (2019).

respectively, the error rate E for the cutoff run is defined as the ratio between σ^{cut} and σ^{max},

$$E = \frac{\sigma^{cut}}{\sigma^{max}} \, . \tag{4.10}$$

Here, the standard deviation of the max error run σ^{max} is used to normalize the standard deviation of the cutoff run σ^{cut}. The reason is as follows. As shown in Fig 4.9a, the freshwater distribution $dV(S)$ becomes more diverse with the increasing cutoff periods. Correspondingly, σ^{cut} must increase with increasing cutoff periods, but also it must have an upper limit that is σ^{max}, since the max error run is the most diverse situation. Consequently, this normalization ensures that $E < 100\%$. Ideally, if the cutoff period is set to zero (all ensemble members are forcing with the same, unfiltered wind), every ensemble member will have the same freshwater distribution, and thus σ^{cut} will be zero; this ensures that the most accurate situation has $E = 0\%$. As noted above, E decreases with decreasing cutoff periods, varies between 0% and 100%, and hence represents the accuracy of a river plume simulation. In this study, $E = 5\%$ is used as the threshold to determine the accuracy of a river plume simulation.

Simulation error rate, E, as a function of the cutoff period is shown in Fig 4.9b, which can be regressed by a power function of the cutoff period with a robust correlation ($r^2 = 0.98$). Two-sided T test is conducted for the regression and the raw data, and the result shows that they are statistically indistinguishable with $p = 0.99$. Since a cutoff period is equal to two times of a temporal resolution, E can be related to a temporal resolution, Δt, as follows

$$E \; = \; 10^{-1.1} \times (2\Delta t)^{0.6} \, . \tag{4.11}$$

For the resolutions higher than 12-hourly (corresponding to the cutoff period less than 1 day), the error rates are lower than 90%. The single-point measurements with the sampling rate of 30 minutes seem to not be necessary to be used as wind forcing, because the improvement will be slight and the spatial information will be missed compared to the atmospheric GCM data. More details will be discussed in Section 4.4.

4.3.5 Linking Simulation Error to Missing Wind Energy

Comparative experiments in Section 4.3.1 lead to a hypothesis that the fraction of the missing wind energy is the dominant factor controlling simulation errors. This hypothesis will be tested in this section. In order to link the simulation error rate E to the missing wind energy, we normalize the missing wind energy by the total wind energy. Cumulative missing energy ratio, R, is defined as the ratio between the cumulative missing wind energy and the total wind energy based on FFT spectrum. Based on the regressed FFT spectrum shown in Fig 4.2a, R is calculated for all the cutoff periods used in the filter experiment. Fig 4.10a shows the R as a function of the cutoff period. We can see that R decreases with decreasing cutoff periods as E does, and the best power function to fit R is

$$R \;=\; 10^{-1.2} \times (2\Delta t)^{0.7}\,, \tag{4.12}$$

where Δt is the temporal resolution ($2\Delta t$ is the cutoff period). Correlation between the regression and the raw data is $r^2 = 0.99$, and the two-sided T test shows that they are statistically indistinguishable with $p = 0.93$.

The similarity between Eq. (4.11) and Eq. (4.12) implies a strong link between the simulation error rate, E, and the cumulative missing energy ratio, R. Fig 4.10b shows the comparison between E and R for all cutoff runs in the randomized phase filter experiment. Correlation between E and R is $r^2 = 0.98$. A two-sided T test is conducted to test if E and R are statistically identical, with similar values. The test results are $t = -0.03$ and $p = 0.97$. Based on the criterion of $p = 0.05$, we cannot reject the null hypothesis in the T test, indicating E and R are indistinguishable; this implies that R is the primary factor indicating river plume simulation errors. In other words, the reason why E is a power function of the cutoff period is due to R being a power function of the cutoff period. Furthermore, Fig 4.10a shows that the wind energy at the periods of several hours is weak (less than 5% of total energy) and hence is insignificant to influence mixing in a river plume. Note that, the specific numbers of E and R are associated with the choice of the wind data that is a single-point measurement in the Mississippi River plume region. However, the 1:1 relation

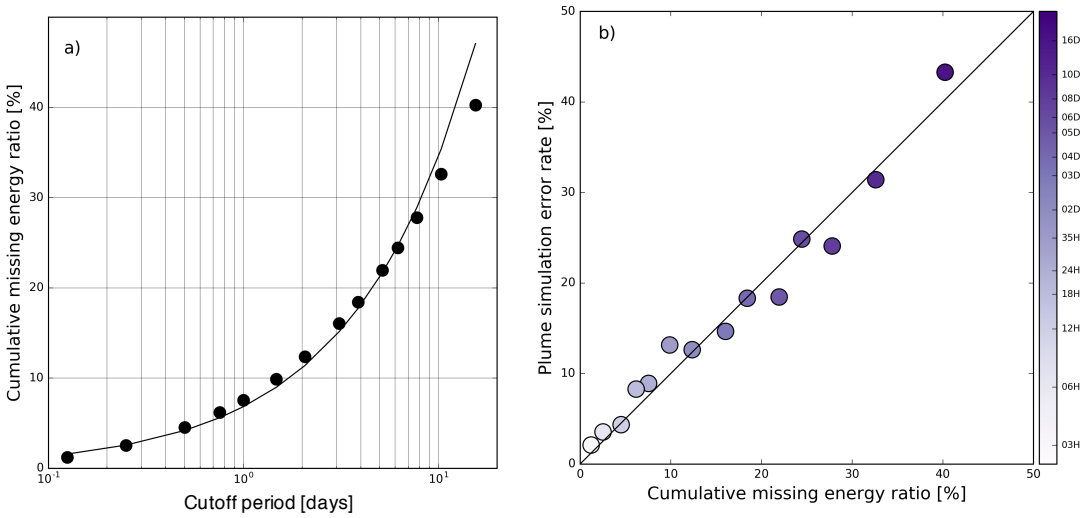

Figure 4.10: a) Cumulative missing energy ratio, R, as a function of the cutoff period, and black line is the best power function to fit the dots. b) Comparison between the cumulative missing energy ratio, R, and the simulation error rate, E, and black line is the 1:1 line. Colors represent the cutoff periods. Reprinted with permission from Qu and Hetland (2019).

between E and R should be general for the river plume simulations in other regions. Therefore, R can be used to estimate the error of a river plume simulation caused by temporal subsampling of wind forcing.

4.4 Discussion and Conclusions

Should single-point measurements or atmospheric GCM data be used as the wind forcing in river plume simulations? Or, if choosing atmospheric GCM data, what temporal resolution should be selected? The cumulative missing energy ratio can be used to tackle these problems. Analyzing the FFT spectrum of a wind measurement in the simulation region will be helpful for deriving an estimation of the simulation error.

Here, we give three realistic examples, the Mississippi River, Columbia River, and Merrimack River, to show the determination of temporal resolution of wind forcing. The wind data for the Mississippi River are the realistic wind measurements shown in Fig 4.2b. The other two observations are from the National Data Buoy Center (NDBC). The buoy in the Columbia River plume

Table 4.1: Cumulative missing energy ratios, R, of the subsampled winds in the Mississippi River, Columbia River, and Merrimack River regions. Reprinted with permission from Qu and Hetland (2019).

Resolution	6-hourly	4-hourly	3-hourly	2-hourly	hourly
Mississippi	8.94%	6.69%	4.93%	3.46%	1.66%
Columbia	5.91%	3.72%	3.00%	1.97%	0.79%
Merrimack	9.04%	6.47%	4.91%	3.69%	1.42%

region is NDBC Station 46029, NDBC Station IOSN3 for the Merrimack River plume region. Both subsampling rates are 10 minutes, and the along-shore wind records in August 2014 are used. First, FFT spectra of the wind data are calculated. Then, the cumulative missing energy ratios R are calculated based on the spectra and the selected cutoff periods. The cutoff periods are selected as: 24 hours, 12 hours, 8 hours, 6 hours, 4 hours, and 2 hours, and the corresponding temporal resolutions are at the half of the associated cutoff periods. R for these three wind measurements are shown in Tab 4.1.

R of the Columbia River case is generally smaller than the Merrimack River and Mississippi River cases. The reason is that, according to the analysis of FFT spectra (not shown), the wind energy at the periods of several hours in the Columbia River region is generally weaker. Considering that R is 1:1 related to the simulation error E and 5% error rate is the accuracy criterion, the 4-hourly wind forcing for the Columbia River plume simulation will be very accurate with an error rate around 3.72%. However, the 4-hourly wind forcing in the Mississippi River and Merrimack River regions would cause the error rates of around 6.69% and 6.47%, respectively. These error rates cannot meet the criterion, so it is necessary to choose the 3-hourly wind forcing to get the acceptable error rates. In all cases, the single-point measurements with the sampling rates of 10 or 30 minutes are not necessary to be used as wind forcing. Of course, different specific applications may have different acceptable error rates. Other, large sources of error may render even a 10% error rate inconsequential; well calibrated simulations may find errors of even a few percents unacceptable.

Supported by idealized numerical simulations, the river plume simulation errors caused by

temporal subsampling of wind forcing are evaluated using the metrics of plume extent, freshwater transport, and plume structure in salinity coordinates. The wind forcing used in the control run is a reconstructed, near-realistic wind based on a wind measurement in the Mississippi River plume region. Low-pass attenuated amplitude filter and randomized phase filter are applied to generate subsampled wind forcing, and the associated simulations are compared to the control run. We find that, if the cutoff periods are smaller than 3 days, the attenuated and the randomized winds cause nearly identical simulation errors (in terms of plume extent and freshwater transport). This indicates that the evolution of a river plume is not sensitive to the high-frequency (period $< 3\ days$) variation of the wind and missing high-frequency wind components has a similar effect as adding random information at the high-frequency bands. Furthermore, the simulation error rate (in terms of plume structure in salinity coordinates) is found to be significantly ($r^2 = 0.98$, $p = 0.99$) related to the temporal resolution by $E = 10^{-1.1} \times (2\Delta t)^{0.6}$.

The factor controlling simulation error rates has been explored. Comparative experiments imply that the amount of missing FFT components in wind is not the dominant factor, but the fraction of missing wind energy can significantly influence the accuracy of a river plume simulation. The primary finding of this study is that the key factor controlling simulation errors is the cumulative missing energy ratio of a subsampled wind forcing. River plume simulation error rates are significantly ($r^2 = 0.98$, $p = 0.97$) 1:1 related to the cumulative missing energy ratios. The results established in this study is based on the scenario of simulating the Mississippi River plume but is supposed to be general for the other river plume simulations.

This finding allows us to better estimate potential plume simulation errors introduced by temporally subsampling winds prior to running a model. Since the cumulative missing energy ratio can be easily calculated based on the FFT spectrum of a wind speed series, conducting an FFT analysis on a wind measurement in the simulation region will be helpful for properly selecting wind forcing data and setting up a model configuration. According to the cumulative missing energy ratios of the wind records in the Mississippi River, Columbia River, and Merrimack River regions, the 3-hourly or 4-hourly atmospheric GCM data would be an acceptable choice for a criterion of

5% error rate, and single-point measurements with higher temporal resolutions are not necessary, because the temporal improvement will be slight.

This study does not address spatial errors in winds, and it may be possible that improvements in high temporal resolution may be undermined by errors in spatial structure of winds, such as the timing and magnitude of frontal passages. However, if the errors in the spatial wind structure can be estimated based on comparison with observations, this may be compared with the errors due to temporal resolution, so that the best wind products to use for a simulation may be selected.

4.5 Acknowledgments

This chapter is based on an article published in the Journal of Geophysical Research - oceans, 2019, co-authored by Professor Robert Hetland. The TABS data were provided by Professor Steven DiMarco. The support of Brian Buckingham, and Dr. Kristen Thyng, grant 18-132-000-A673 from Texas General Land Office, and a scholarship from China Scholarship Council is also gratefully acknowledged.

5. CONCLUSIONS

Supported by numerical simulations, the classical theories of baroclinic instabilities and NIWs have been revisited and extended in an attempt to better understand the fundamental physics of the submesoscale vortices and NIWs in coastal buoyancy-driven flows. To better simulate coastal buoyancy-driven flows, the simulation errors caused by temporally subsampling winds are quantified to provide general guidance on properly selecting wind forcing. Main findings of these studies are summarized as follows.

Baroclinic instabilities are ubiquitous in open oceans but seldom observed in coastal zones, even though lateral density gradients within coastal fronts are often stronger than those of open ocean fronts. This study explores the non-geostrophic baroclinic instability theories adapted to the scenario with sloping bathymetry and demonstrates the suppression of instabilities, through a reduction in growth rate, in the non-geostrophic limit. Both the layered and continuously stratified models reveal that the suppression is related to a new parameter, slope-relative Burger number $S_r = \frac{N}{f}(\alpha + \frac{M^2}{N^2})$, which represents the gradient of potential vorticity supplemented by topographic effects. The instability growth is found to be inhibited with increasing S_r. The underlying mechanism of S_r is that the growth of baroclinic instabilities is directly related to Rossby wave resonance, and S_r controls the wave resonance by modifying the properties of the Rossby waves, thereby influencing the the growth of instabilities. One limitation of the adapted theories is the assumption of a tilted surface. However, this limitation does not prohibit application to the flat-surface cases, so long as the slope Burger number $S = \frac{N}{f}\alpha \lesssim O(10^{-1})$ and horizontal slope Burger number $S_H = \frac{M^2}{f^2}\alpha \lesssim O(10^{-1})$; this feasibility is verified by a set of numerical simulations. S_r is inversely proportional to the Richardson number $Ri^{1/2}$, and coastal fronts are often energetic, characterized by low Ri, which is why baroclinic instabilities may be suppressed in coastal regions where they might otherwise be expected.

NIWs are ubiquitous in the ocean and actively interact with ocean fronts. The modifications of NIWs at jet-like fronts have been extensively investigated, while the modifications at curved

fronts such as mesoscale and submesoscale eddies are less understood. This study focuses on how the curvature of a front modifies the properties of NIWs; particularly, the modifications in an anti-cyclonic baroclinic vortex are explored. The time-dependent Eliassen-Sawyer equation, dispersion relation, and wave energy density equation are derived in cylindrical coordinates to describe the NIWs in a baroclinic vortex. Ray tracing and the numerical calculation of wave energy density provide support that NIWs in an energetic anti-cyclonic vortex can be significantly modified by the curvature – the fully non-linear, idealized simulation also confirms that NIWs in such a vortex can propagate deeper than at a front without curvature and hence might cause deeper mixing than previously predicted. The theory is used to interpret the results from realistic simulations of the northern Gulf of Mexico, which exhibit enhanced mixing at the base of an anti-cyclone that is related to the trapping of NIWs. It is possible that this mixing could result in the ventilation of bottom waters and might explain the transient features of bottom hypoxia in this region.

Wind is a primary forcing agent for river plume variability. Consequently, the temporal resolution of wind forcing is an important factor to consider for river plume simulations. This study evaluates river plume simulation errors caused by temporal subsampling of wind forcing data. We use an idealized model of a river plume over a continental shelf and force the model with temporally filtered winds to quantify the effect of temporal subsampling on simulation accuracy. The simulation error is proportional to the fraction of energy missing in the high-frequency wind absent from the forcing. These results set requirements for temporal wind resolution in realistic simulations of river plumes. Spectral analysis of observed wind records at the Mississippi River, Columbia River, and Merrimack River regions indicates that, for simulation errors due to insufficient temporal wind resolution to be smaller than 5% of the variance, 3-hourly or 4-hourly wind data are reasonable. Though horizontal variations in wind forcing are lost, analyzing FFT spectrum of a single-point wind measurement in the simulation region is helpful for estimating simulation errors due to temporal resolution, and hence aid in properly selecting temporal resolutions.

REFERENCES

Alford, M. H. (2003). Redistribution of energy available for ocean mixing by long-range propagation of internal waves. *Nature*, 423(6936):159.

Alford, M. H., MacKinnon, J. A., Simmons, H. L., and Nash, J. D. (2016). Near-inertial internal gravity waves in the ocean. *Annual review of marine science*, 8:95–123.

Andersson, E. (2015). User guide to ecmwf forecast products. *http://www.ecmwf.int/en/forecasts/datasets/catalogue-ecmwf-real-time-products*.

Barkan, R., McWilliams, J. C., Molemaker, M. J., Choi, J., Srinivasan, K., Shchepetkin, A. F., and Bracco, A. (2017a). Submesoscale dynamics in the northern gulf of mexico. part ii: Temperature–salinity relations and cross-shelf transport processes. *Journal of Physical Oceanography*, 47(9):2347–2360.

Barkan, R., McWilliams, J. C., Shchepetkin, A. F., Molemaker, M. J., Renault, L., Bracco, A., and Choi, J. (2017b). Submesoscale dynamics in the northern gulf of mexico. part i: Regional and seasonal characterization and the role of river outflow. *Journal of Physical Oceanography*, 47(9):2325–2346.

Barkan, R., Winters, K. B., and McWilliams, J. C. (2017c). Stimulated imbalance and the enhancement of eddy kinetic energy dissipation by internal waves. *Journal of Physical Oceanography*, 47(1):181–198.

Bianchi, T. S., DiMarco, S., Cowan Jr, J., Hetland, R., Chapman, P., Day, J., and Allison, M. (2010). The science of hypoxia in the northern gulf of mexico: a review. *Science of the Total Environment*, 408(7):1471–1484.

Blumsack, S. L. and Gierasch, P. (1972). Mars: The effects of topography on baroclinic instability. *Journal of the Atmospheric Sciences*, 29(6):1081–1089.

Boccaletti, G., Ferrari, R., and Fox-Kemper, B. (2007). Mixed layer instabilities and restratification. *Journal of Physical Oceanography*, 37(9):2228–2250.

Brannigan, L., Marshall, D. P., Naveira Garabato, A. C., Nurser, A. G., and Kaiser, J. (2017). Sub-

mesoscale instabilities in mesoscale eddies. *Journal of Physical Oceanography*, 47(12):3061–3085.

Burns, K. J., Vasil, G. M., Oishi, J. S., Lecoanet, D., and Brown, B. (2016). Dedalus: Flexible framework for spectrally solving differential equations. *Astrophysics Source Code Library*.

Callies, J., Ferrari, R., Klymak, J. M., and Gula, J. (2015). Seasonality in submesoscale turbulence. *Nature communications*, 6:6862.

Callies, J., Flierl, G., Ferrari, R., and Fox-Kemper, B. (2016). The role of mixed-layer instabilities in submesoscale turbulence. *Journal of Fluid Mechanics*, 788:5–41.

Canuto, V. M., Howard, A., Cheng, Y., and Dubovikov, M. (2001). Ocean turbulence. part i: One-point closure modelâĂŤmomentum and heat vertical diffusivities. *Journal of Physical Oceanography*, 31(6):1413–1426.

Chaigneau, A., Pizarro, O., and Rojas, W. (2008). Global climatology of near-inertial current characteristics from lagrangian observations. *Geophysical Research Letters*, 35(13).

Chant, R. (2012). *Interactions between Estuaries and Coasts: River Plumes - Their Formation, Transport, and Dispersal*, volume 2, pages 213–235. Elsevier Inc., United States.

Cole, K. L. and Hetland, R. D. (2016). The effects of rotation and river discharge on net mixing in small-mouth kelvin number plumes. *Journal of Physical Oceanography*, 46(5):1421–1436.

Cushman-Roisin, B. and Beckers, J.-M. (2011). *Introduction to geophysical fluid dynamics: physical and numerical aspects*, volume 101. Academic Press.

DiMarco, S. F., Howard, M. K., and Reid, R. O. (2000a). Seasonal variation of wind-driven diurnal current cycling om the Texas-Louisiana Continental Shelf. *Geophys. Res. Lett.*, 27(7):1017–1020.

DiMarco, S. F., Howard, M. K., and Reid, R. O. (2000b). Seasonal variation of wind-driven diurnal current cycling on the texas-louisiana continental shelf. *Geophysical Research Letters*, 27(7):1017–1020.

DiMarco, S. F. and Reid, R. O. (1998). Characterization of the principal tidal current constituents on the Texas-Louisiana Shelf. *J. Geophys. Res.*, 103(2):3093–3110.

Eady, E. T. (1949). Long waves and cyclone waves. *Tellus*, 1(3):33–52.

Eliassen, A. (1951). Slow thermally or frictionally controlled meridional circulation in a circular vortex. *Astrophysica Norvegica*, 5:19.

Eliassen, A. (1962). On the vertical circulation in frontal zones. *Geofys. publ*, 24(4):147–160.

Epifanio, C. and Garvine, R. (2001). Larval transport on the atlantic continental shelf of north america: a review. *Estuarine, coastal and shelf Science*, 52(1):51–77.

Ferrari, R. and Wunsch, C. (2009). Ocean circulation kinetic energy: Reservoirs, sources, and sinks. *Annual Review of Fluid Mechanics*, 41.

Fong, D. A. and Geyer, W. R. (2001). Response of a river plume during an upwelling favorable wind event. *Journal of Geophysical Research: Oceans*, 106(C1):1067–1084.

Fong, D. A. and Geyer, W. R. (2002). The alongshore transport of freshwater in a surface-trapped river plume. *Journal of Physical Oceanography*, 32(3):957–972.

Fong, D. A., Geyer, W. R., and Signell, R. P. (1997). The wind-forced response on a buoyant coastal current: Observations of the western gulf of maine plume. *Journal of Marine Systems*, 12(1-4):69–81.

Fox-Kemper, B., Ferrari, R., and Hallberg, R. (2008). Parameterization of mixed layer eddies. part i: Theory and diagnosis. *Journal of Physical Oceanography*, 38(6):1145–1165.

Franks, P. and Anderson, D. (1992). Alongshore transport of a toxic phytoplankton bloom in a buoyancy current: Alexandrium tamarense in the gulf of maine. *Marine Biology*, 112(1):153–164.

Grisouard, N. and Thomas, L. N. (2015). Critical and near-critical reflections of near-inertial waves off the sea surface at ocean fronts. *Journal of Fluid Mechanics*, 765:273–302.

Grisouard, N. and Thomas, L. N. (2016). Energy exchanges between density fronts and near-inertial waves reflecting off the ocean surface. *Journal of Physical Oceanography*, 46(2):501–516.

Haine, T. W. and Marshall, J. (1998). Gravitational, symmetric, and baroclinic instability of the ocean mixed layer. *Journal of physical oceanography*, 28(4):634–658.

Haza, A. C., DâĂŹAsaro, E., Chang, H., Chen, S., Curcic, M., Guigand, C., Huntley, H., Jacobs, G., Novelli, G., Özgökmen, T., et al. (2018). Drogue-loss detection for surface drifters during the lagrangian submesoscale experiment (laser). *Journal of Atmospheric and Oceanic Technology*, 35(4):705–725.

Hetland (2010). The effects of mixing and spreading on density in near-field river plumes. *Dynamics of Atmospheres and Oceans*, 49(1):37–53.

Hetland and DiMarco, S. F. (2012a). Skill assessment of a hydrodynamic model of circulation over the texas–louisiana continental shelf. *Ocean Modelling*, 43:64–76.

Hetland and Hsu, T. (2013). Freshwater and sediment dispersal in large river plumes. *Biogeochemical Dynamics at Large River-Coastal Interfaces: Linkages with Global Climate Change*, pages 55–85.

Hetland, R. D. (2005). Relating river plume structure to vertical mixing. *Journal of Physical Oceanography*, 35(9):1667–1688.

Hetland, R. D. (2017). Suppression of baroclinic instabilities in buoyancy-driven flow over sloping bathymetry. *Journal of Physical Oceanography*, 47(1):49–68.

Hetland, R. D. and DiMarco, S. F. (2008). How does the character of oxygen demand control the structure of hypoxia on the texas–louisiana continental shelf? *Journal of Marine Systems*, 70(1-2):49–62.

Hetland, R. D. and DiMarco, S. F. (2012b). Skill assessment of a hydrodynamic model of circulation over the Texas- Louisiana continental shelf. *Ocean Modelling*, 43-44:64–76, doi:10.1016/j.ocemod.2011.11.009.

Horner-Devine, A. R., Fong, D. A., Monismith, S. G., and Maxworthy, T. (2006). Laboratory experiments simulating a coastal river inflow. *Journal of Fluid Mechanics*, 555:203–232.

Horner-Devine, A. R., Hetland, R. D., and MacDonald, D. G. (2015). Mixing and transport in coastal river plumes. *Annual Review of Fluid Mechanics*, 47:569–594.

Jebson, S. (2007). National meteorological library and archive fact sheet 6: The beaufort scale. *Met Office, United Kingdom*.

Joyce, T. M., Toole, J. M., Klein, P., and Thomas, L. N. (2013). A near-inertial mode observed within a gulf stream warm-core ring. *Journal of Geophysical Research: Oceans*, 118(4):1797–1806.

Kanamitsu, M., Ebisuzaki, W., Woollen, J., Yang, S.-K., Hnilo, J., Fiorino, M., and Potter, G. (2002). Ncep–doe amip-ii reanalysis (r-2). *Bulletin of the American Meteorological Society*, 83(11):1631–1643.

Kourafalou, V. H., Lee, T. N., Oey, L.-Y., and Wang, J. D. (1996). The fate of river discharge on the continental shelf: 2. transport of coastal low-salinity waters under realistic wind and tidal forcing. *Journal of Geophysical Research: Oceans*, 101(C2):3435–3455.

Kunze, E. (1985). Near-inertial wave propagation in geostrophic shear. *Journal of Physical Oceanography*, 15(5):544–565.

Kunze, E. and Boss, E. (1998). A model for vortex-trapped internal waves. *Journal of physical oceanography*, 28(10):2104–2115.

Kunze, E. and Sanford, T. B. (1984). Observations of near-inertial waves in a front. *Journal of Physical Oceanography*, 14(3):566–581.

Kunze, E., Schmitt, R. W., and Toole, J. M. (1995). The energy balance in a warm-core ring's near-inertial critical layer. *Journal of physical oceanography*, 25(5):942–957.

Lapeyre, G. and Klein, P. (2006). Dynamics of the upper oceanic layers in terms of surface quasi-geostrophy theory. *Journal of physical oceanography*, 36(2):165–176.

Lee, D.-K. and Niiler, P. P. (1998). The inertial chimney: The near-inertial energy drainage from the ocean surface to the deep layer. *Journal of Geophysical Research: Oceans*, 103(C4):7579–7591.

Lentz, S. (2004). The response of buoyant coastal plumes to upwelling-favorable winds. *Journal of Physical oceanography*, 34(11):2458–2469.

Lentz, S. J. and Helfrich, K. R. (2002). Buoyant gravity currents along a sloping bottom in a rotating fluid. *Journal of Fluid Mechanics*, 464:251–278.

Lohrenz, S. E., Fahnenstiel, G. L., Redalje, D. G., Lang, G. A., Dagg, M. J., Whitledge, T. E., and

Dortch, Q. (1999). Nutrients, irradiance, and mixing as factors regulating primary production in coastal waters impacted by the mississippi river plume. *Continental Shelf Research*, 19(9):1113–1141.

Luo, H., Bracco, A., Cardona, Y., and McWilliams, J. C. (2016). Submesoscale circulation in the northern gulf of mexico: Surface processes and the impact of the freshwater river input. *Ocean Modelling*, 101:68–82.

Mariano, A., Ryan, E., Huntley, H., Laurindo, L., Coelho, E., Griffa, A., Özgökmen, T., Berta, M., Bogucki, D., Chen, S., et al. (2016). Statistical properties of the surface velocity field in the northern gulf of mexico sampled by glad drifters. *Journal of Geophysical Research: Oceans*, 121(7):5193–5216.

Marta-Almeida, M., Hetland, R. D., and Zhang, X. (2013). Evaluation of model nesting performance on the texas-louisiana continental shelf. *Journal of Geophysical Research: Oceans*, 118(5):2476–2491.

Masse, A. K. and Murthy, C. (1990). Observations of the niagara river thermal plume (lake ontario, north america). *Journal of Geophysical Research: Oceans*, 95(C9):16097–16109.

Masse, A. K. and Murthy, C. (1992). Analysis of the niagara river plume dynamics. *Journal of Geophysical Research: Oceans*, 97(C2):2403–2420.

Mesinger, F., DiMego, G., Kalnay, E., Mitchell, K., Shafran, P. C., Ebisuzaki, W., Jović, D., Woollen, J., Rogers, E., Berbery, E. H., et al. (2006). North american regional reanalysis. *Bulletin of the American Meteorological Society*, 87(3):343–360.

Moffat, C. and Lentz, S. (2012). On the response of a buoyant plume to downwelling-favorable wind stress. *Journal of Physical Oceanography*, 42(7):1083–1098.

Mooers, C. N. (1975). Several effects of a baroclinic current on the cross-stream propagation of inertial-internal waves. *Geophysical and Astrophysical Fluid Dynamics*, 6(3):245–275.

Morey, S. L., Martin, P. J., O'Brien, J. J., Wallcraft, A. A., and Zavala-Hidalgo, J. (2003). Export pathways for river discharged fresh water in the northern Gulf of Mexico. *J. Geophys. Res.*, 108(C10):doi:10.1029/2002JC001674.

Nagai, T., Tandon, A., Kunze, E., and Mahadevan, A. (2015). Spontaneous generation of near-inertial waves by the kuroshio front. *Journal of Physical Oceanography*, 45(9):2381–2406.

NCEP (2003). Global climate and weather modelling branch: The gfs atmospheric model. *NCEP Office Note 422, Camp Springs, Maryland, USA*.

O'Donnell, J., Dam, H. G., Bohlen, W. F., Fitzgerald, W., Gay, P. S., Houk, A. E., Cohen, D. C., and Howard-Strobel, M. M. (2008). Intermittent ventilation in the hypoxic zone of western long island sound during the summer of 2004. *Journal of Geophysical Research: Oceans*, 113(C9).

Onogi, K., Tsutsui, J., Koide, H., Sakamoto, M., Kobayashi, S., Hatsushika, H., Matsumoto, T., Yamazaki, N., Kamahori, H., Takahashi, K., et al. (2007). The jra-25 reanalysis. *Journal of the Meteorological Society of Japan. Ser. II*, 85(3):369–432.

Pedlosky, J. (2013). *Geophysical fluid dynamics*. Springer Science & Business Media.

Pedlosky, J. (2016). Baroclinic instability over topography: Unstable at any wave number. *Journal of Marine Research*, 74(1):1–19.

Perkins, H. (1976). Observed effect of an eddy on inertial oscillations. In *Deep Sea Research and Oceanographic Abstracts*, volume 23, pages 1037–1042. Elsevier.

Phillips, N. A. (1954). Energy transformations and meridional circulations associated with simple baroclinic waves in a two-level, quasi-geostrophic model. *Tellus*, 6(3):274–286.

Poje, A. C., Özgökmen, T. M., Bogucki, D. J., and Kirwan, A. (2017). Evidence of a forward energy cascade and kolmogorov self-similarity in submesoscale ocean surface drifter observations. *Physics of Fluids*, 29(2):020701.

Polzin, K. L. and Lvov, Y. V. (2011). Toward regional characterizations of the oceanic internal wavefield. *Reviews of Geophysics*, 49(4).

Qu, L. and Hetland, R. D. (2019). Temporal resolution of wind forcing required for river plume simulations. *Journal of Geophysical Research: Oceans*, 124(3):1459–1473.

Rabalais, N. N., Turner, R. E., Justic, D., Dortch, Q., and Wiseman Jr, W. J. (1999). Characterization of hypoxia: topic i report for the integrated assessment on hypoxia in the gulf of mexico.

Rienecker, M. M., Suarez, M. J., Gelaro, R., Todling, R., Bacmeister, J., Liu, E., Bosilovich, M. G.,

Schubert, S. D., Takacs, L., Kim, G.-K., et al. (2011). Merra: Nasa?s modern-era retrospective analysis for research and applications. *Journal of climate*, 24(14):3624–3648.

Rocha, C. B., Wagner, G. L., and Young, W. R. (2018). Stimulated generation: extraction of energy from balanced flow by near-inertial waves. *Journal of Fluid Mechanics*, 847:417–451.

Saha, S., Moorthi, S., Pan, H.-L., Wu, X., Wang, J., Nadiga, S., Tripp, P., Kistler, R., Woollen, J., Behringer, D., et al. (2010). The ncep climate forecast system reanalysis. *Bulletin of the American Meteorological Society*, 91(8):1015–1057.

Sakai, S. (1989). Rossby-kelvin instability: a new type of ageostrophic instability caused by a resonance between rossby waves and gravity waves. *Journal of Fluid Mechanics*, 202:149–176.

Sawyer, J. (1956). The vertical circulation at meteorological fronts and its relation to frontogenesis. In *Proceedings of the Royal Society of London A: Mathematical, Physical and Engineering Sciences*, volume 234, pages 346–362. The Royal Society.

Shchepetkin, A. F. and McWilliams, J. C. (2005). The regional oceanic modeling system (roms): a split-explicit, free-surface, topography-following-coordinate oceanic model. *Ocean Modelling*, 9(4):347–404.

Shcherbina, A. Y., D'Asaro, E. A., Lee, C. M., Klymak, J. M., Molemaker, M. J., and McWilliams, J. C. (2013). Statistics of vertical vorticity, divergence, and strain in a developed submesoscale turbulence field. *Geophysical Research Letters*, 40(17):4706–4711.

Simmons, A., Uppala, S., Dee, D., and Kobayashi, S. (2007). Era-interim: New ecmwf reanalysis products from 1989 onwards. *ECMWF newsletter*, 110(110):25–35.

Simmons, H. L. and Alford, M. H. (2012). Simulating the long-range swell of internal waves generated by ocean storms. *Oceanography*, 25(2):30–41.

Smolarkiewicz, P. K. and Margolin, L. G. (1998). Mpdata: A finite-difference solver for geophysical flows. *Journal of Computational Physics*, 140(2):459–480.

Stone, P. H. (1966). On non-geostrophic baroclinic stability. *Journal of the Atmospheric Sciences*, 23(4):390–400.

Stone, P. H. (1970). On non-geostrophic baroclinic stability: Part ii. *Journal of the Atmospheric*

Sciences, 27(5):721–726.

Stone, P. H. (1971). Baroclinic stability under non-hydrostatic conditions. *Journal of Fluid Mechanics*, 45(4):659–671.

Syvitski, J. P., Vörösmarty, C. J., Kettner, A. J., and Green, P. (2005). Impact of humans on the flux of terrestrial sediment to the global coastal ocean. *Science*, 308(5720):376–380.

Taylor, S. and Straub, D. (2016). Forced near-inertial motion and dissipation of low-frequency kinetic energy in a wind-driven channel flow. *Journal of Physical Oceanography*, 46(1):79–93.

Thomas, L. N. (2012). On the effects of frontogenetic strain on symmetric instability and inertia–gravity waves. *Journal of Fluid Mechanics*, 711:620–640.

Thomas, L. N. (2017). On the modifications of near-inertial waves at fronts: implications for energy transfer across scales. *Ocean Dynamics*, 67(10):1335–1350.

Thomas, L. N. and Taylor, J. R. (2014). Damping of inertial motions by parametric subharmonic instability in baroclinic currents. *Journal of Fluid Mechanics*, 743:280–294.

Thyng, K. and Marta-Almeida, M. (2017). Texas automated buoy system. *http://pong.tamu.edu/tabswebsite*.

Thyng, K. M. and Hetland, R. D. (2017). Texas and louisiana coastal vulnerability and shelf connectivity. *Marine pollution bulletin*, 116(1-2):226–233.

Thyng, K. M. and Hetland, R. D. (2018). Seasonal and interannual cross-shelf transport over the texas and louisiana continental shelf. *Continental Shelf Research*, 160:23–35.

Tilburg, C. E. (2003). Across-shelf transport on a continental shelf: Do across-shelf winds matter? *Journal of Physical Oceanography*, 33(12):2675–2688.

Trenberth, K. E., Smith, L., Qian, T., Dai, A., and Fasullo, J. (2007). Estimates of the global water budget and its annual cycle using observational and model data. *Journal of Hydrometeorology*, 8(4):758–769.

Umlauf, L. and Burchard, H. (2003). A generic length-scale equation for geophysical turbulence models. *Journal of Marine Research*, 61(2):235–265.

Wagner, G. and Young, W. (2016). A three-component model for the coupled evolution of near-

inertial waves, quasi-geostrophic flow and the near-inertial second harmonic. *Journal of Fluid Mechanics*, 802:806–837.

Wenegrat, J. O., Callies, J., and Thomas, L. N. (2018). Submesoscale baroclinic instability in the bottom boundary layer. *Journal of Physical Oceanography*, 48(11):2571–2592.

Whalen, C., Talley, L., and MacKinnon, J. (2012). Spatial and temporal variability of global ocean mixing inferred from argo profiles. *Geophysical Research Letters*, 39(18).

Whitt, D. B. and Thomas, L. N. (2013). Near-inertial waves in strongly baroclinic currents. *Journal of Physical Oceanography*, 43(4):706–725.

Whitt, D. B., Thomas, L. N., Klymak, J. M., Lee, C. M., and D?Asaro, E. A. (2018). Interaction of superinertial waves with submesoscale cyclonic filaments in the north wall of the gulf stream. *Journal of Physical Oceanography*, 48(1):81–99.

Wunsch, C. and Ferrari, R. (2004). Vertical mixing, energy, and the general circulation of the oceans. *Annu. Rev. Fluid Mech.*, 36:281–314.

Xie, J.-H. and Vanneste, J. (2015). A generalised-lagrangian-mean model of the interactions between near-inertial waves and mean flow. *Journal of Fluid Mechanics*, 774:143–169.

Zhang, X., DiMarco, S. F., Smith IV, D. C., Howard, M. K., Jochens, A. E., and Hetland, R. D. (2009). Near-resonant ocean response to sea breeze on a stratified continental shelf. *Journal of Physical Oceanography*, 39(9):2137–2155.

Zhang, X., Marta-Almeida, M., and Hetland, R. (2012). A high-resolution pre-operational forecast model of circulation on the texas-louisiana continental shelf and slope. *Journal of Operational Oceanography*, 5(1):19–34.

Zhang, X., Smith IV, D. C., DiMarco, S. F., and Hetland, R. D. (2010). A numerical study of sea-breeze-driven ocean poincare wave propagation and mixing near the critical latitude. *Journal of Physical Oceanography*, 40(1):48–66.

Zhang, Z., Hetland, R., and Zhang, X. (2014). Wind-modulated buoyancy circulation over the texas-louisiana shelf. *Journal of Geophysical Research: Oceans*, 119(9):5705–5723.

Zimmerle, H. and DiMarco, S. (2017). Mch atlas: Oceanographic observations of the mechanisms

controlling hypoxia project. *Texas A&M University, Texas Sea Grant*, pages TAMU–SG–17–601.

APPENDIX A

LAYERED MODEL OF NON-GEOSTROPHIC BAROCLINIC INSTABILITY – ADAPTED SAKAI MODEL

The following derivation follows Sakai (1989) but is modified to account for the presence of sloping bottom and surface. Considering a rotating two-layer channel with sloping bottom and top and currents in the thermal wind balance, the linearized equations for perturbation are

$$\begin{aligned}
&\frac{\partial u_1^*}{\partial t^*} + U_0\frac{\partial u_1^*}{\partial x^*} - fv_1^* = -\frac{1}{\rho_0}\frac{\partial p_1^*}{\partial x^*}\ ,\\
&\frac{\partial v_1^*}{\partial t^*} + U_0\frac{\partial v_1^*}{\partial x^*} + fu_1^* = -\frac{1}{\rho_0}\frac{\partial p_1^*}{\partial y^*}\ ,\\
&\frac{\partial u_2^*}{\partial t^*} - U_0\frac{\partial u_2^*}{\partial x^*} - fv_2^* = -\frac{1}{\rho_0}\frac{\partial p_2^*}{\partial x^*}\ ,\\
&\frac{\partial v_2^*}{\partial t^*} - U_0\frac{\partial v_2^*}{\partial x^*} + fu_2^* = -\frac{1}{\rho_0}\frac{\partial p_2^*}{\partial y^*}\ ,\\
&\frac{\partial h^*}{\partial t^*} + U_0\frac{\partial h^*}{\partial x^*} = \frac{\partial H_1^* u_1^*}{\partial x^*} + \frac{\partial H_1^* v_1^*}{\partial y^*}\ ,\\
&\frac{\partial h^*}{\partial t^*} - U_0\frac{\partial h^*}{\partial x^*} = -(\frac{\partial H_2^* u_2^*}{\partial x^*} + \frac{\partial H_2^* v_2^*}{\partial y^*})\ ,\\
&p_2^* - p_1^* = \rho_0 g^{'} h^*\ ,
\end{aligned} \tag{A.1}$$

subject to

$$\begin{aligned}
v_1^*|_{y^*=\pm Y_{max}^*} &= 0,\\
v_2^*|_{y^*=\pm Y_{max}^*} &= 0,
\end{aligned} \tag{A.2}$$

where u^* is the perturbed along-slope velocity, v^* is the perturbed across-slope velocity, p^* is the perturbed pressure, h^* is the interface displacement, g' is the reduced gravity, f is the Coriolis parameter, $\pm Y_{max}^*$ are the across-slope boundaries, and the upper and lower layer variables are denoted by the subscripts of 1 and 2, respectively. The background thermal wind velocities in the upper and lower layers are set to U_0 and $-U_0$ for simplicity (Sakai, 1989). $H_1^* = H_0 - \alpha y^* - \beta y^*$ is the thickness of the upper layer, and $H_2^* = H_0 + \alpha y^* + \beta y^*$ for the lower layer, where α is the

bottom slope and $\beta \equiv \frac{M^2}{N^2} = \frac{2U_0 f}{g'}$ is the isopycnal slope.

Considering the time scale as $1/f$, the horizontal length scale as the Rossby deformation radius $R_d = \frac{\sqrt{\frac{1}{2}g'H_0}}{f}$, and the vertical length scale as H_0, the scaling relations about the variables in Eq. (A.1) are

$$\begin{aligned} (x^*, y^*) &= R_d(x, y) \\ t^* &= f^{-1}t \end{aligned} \qquad \begin{aligned} (u_1^*, u_2^*) &= U_0(u_1, u_2) \\ (v_1^*, v_2^*) &= U_0(v_1, v_2) \\ (p_1^*, p_2^*) &= \rho_0 U_0 \sqrt{\frac{1}{2}g'H_0}(p_1, p_2) \end{aligned} \qquad \begin{aligned} H_1 &= \frac{H_1^*}{H_0} = 1 - S_r y \\ H_2 &= \frac{H_2^*}{H_0} = 1 + S_r y, \end{aligned} \tag{A.3}$$

where $S_r = (\delta + 1)Ri_b^{-1/2}$ is the slope-relative Burger number. $Ri_b = \frac{g^{'}H_0}{2U_0^2}$ is the bulk Richardson number, and $\delta = \frac{\alpha g^{'}}{2U_0 f}$ is the slope parameter. The dimensionless form of Eq. (A.1) is, then,

$$\begin{aligned} \frac{\partial u_1}{\partial t} + Ri_b^{-1/2}\frac{\partial u_1}{\partial x} - v_1 &= -\frac{\partial p_1}{\partial x}\,, \\ \frac{\partial v_1}{\partial t} + Ri_b^{-1/2}\frac{\partial v_1}{\partial x} + u_1 &= -\frac{\partial p_1}{\partial y}\,, \\ \frac{\partial u_2}{\partial t} - Ri_b^{-1/2}\frac{\partial u_2}{\partial x} - v_2 &= -\frac{\partial p_2}{\partial x}\,, \\ \frac{\partial v_2}{\partial t} - Ri_b^{-1/2}\frac{\partial v_2}{\partial x} + u_2 &= -\frac{\partial p_2}{\partial y}\,, \\ \frac{\partial p_2 - p_1}{\partial t} + Ri_b^{-1/2}\frac{\partial p_2 - p_1}{\partial x} &= 2H_1\frac{\partial u_1}{\partial x} + 2\frac{\partial H_1 v_1}{\partial y}\,, \\ \frac{\partial p_2 - p_1}{\partial t} - Ri_b^{-1/2}\frac{\partial p_2 - p_1}{\partial x} &= -2H_2\frac{\partial u_2}{\partial x} - 2\frac{\partial H_2 v_2}{\partial y}\,, \end{aligned} \tag{A.4}$$

subject to

$$\begin{aligned} v_1|_{y=\pm Y_{max}} &= 0, \\ v_2|_{y=\pm Y_{max}} &= 0. \end{aligned} \tag{A.5}$$

Assuming an ansatz of the form $\phi = \widetilde{\phi}(y)e^{i(kx-\sigma t)}$, substituting the ansatz into Eq. (A.4) and (A.5)

yields the eigenvalue problem as followed (dropping tilde accents for clarity),

$$
\begin{aligned}
(\sigma - Ri_b^{-1/2}k)u_1 - iv_1 - kp_1 &= 0\,, \\
(\sigma - Ri_b^{-1/2}k)v_1 + iu_1 + i\frac{\partial p_1}{\partial y} &= 0\,, \\
(\sigma + Ri_b^{-1/2}k)u_2 - iv_2 - kp_2 &= 0\,, \\
(\sigma + Ri_b^{-1/2}k)v_2 + iu_2 + i\frac{\partial p_2}{\partial y} &= 0\,, \\
(\sigma - Ri_b^{-1/2}k)p_1 - 2k(1 - S_r y)u_1 + i2(1 - S_r y)\frac{\partial v_1}{\partial y} - i2Fv_1 - (\sigma - Ri_b^{-1/2}k)p_2 &= 0\,, \\
(\sigma + Ri_b^{-1/2}k)p_2 - 2k(1 + S_r y)u_2 + i2(1 + S_r y)\frac{\partial v_2}{\partial y} + i2Fv_2 - (\sigma + Ri_b^{-1/2}k)p_1 &= 0\,,
\end{aligned}
\tag{A.6}
$$

subject to

$$
\begin{aligned}
v_1|_{y=\pm Y_{max}} &= 0, \\
v_2|_{y=\pm Y_{max}} &= 0.
\end{aligned}
\tag{A.7}
$$

APPENDIX B

CONTINUOUSLY STRATIFIED MODEL OF NON-GEOSTROPHIC BAROCLINIC INSTABILITY – ADAPTED STONE MODEL

The following derivation follows Stone (1966, 1970, 1971) but is modified to account for the presence of sloping bottom and surface. The coordinates are rotated to align with the sloping topography as Wenegrat et al. (2018), and the derivation is essentially equivalent to Wenegrat et al. (2018) but with a different orientation. Dimensionally, the equations describing a rotational flow field of an adiabatic inviscid fluid with Boussinesq and hydrostatic approximations in the rotated coordinates are

$$\begin{aligned}
\frac{du^*}{dt^*} - fv^*cos\theta - fw^*sin\theta &= -\frac{1}{\rho_0}\frac{\partial p^*}{\partial x^*} \,, \\
\frac{dv^*}{dt^*} + fu^*cos\theta &= -\frac{1}{\rho_0}\frac{\partial p^*}{\partial y^*} - b^*sin\theta \,, \\
\frac{dw^*}{dt^*} + fu^*sin\theta &= -\frac{1}{\rho_0}\frac{\partial p^*}{\partial z^*} + b^*cos\theta \,, \\
\frac{db^*}{dt^*} &= 0 \,, \\
\frac{\partial u^*}{\partial x^*} + \frac{\partial v^*}{\partial y^*} + \frac{\partial w^*}{\partial z^*} &= 0 \,,
\end{aligned} \tag{B.1}$$

subject to

$$\begin{aligned}
w^*|_{z^*=0} &= 0, \\
w^*|_{z^*=H} &= 0,
\end{aligned} \tag{B.2}$$

where θ is the slope angle,u^* is the along-slope velocity, v^* is the across-slope velocity, and w^* is the vertical velocity, p^* is the pressure, and $b^* = g(\rho_0 - \rho)\rho_0^{-1}$ is the buoyancy (ρ and ρ_0 are the seawater density and the reference, respectively). Rigid-lid boundary conditions are applied at the surface ($z^* = H$) and bottom ($z^* = 0$).

Considering the horizontal velocity scale as U, the time scale as f^{-1}, the horizontal length scale as U/f, and the vertical length scale as H, the scaling relations about the variables in Eq.

(B.1) are, then,

$$
\begin{aligned}
(x^*, y^*) &= U f^{-1}(x, y) & (u^*, v^*) &= U(u, v) & b^* &= N^2 H b \\
z^* &= H z & w^* &= H f w & p^* &= \rho_0 N^2 H^2 p \quad .
\end{aligned}
\tag{B.3}
$$

Thus, Eq. (B.1) and (B.2) have the dimensionless form

$$
\begin{aligned}
\frac{du}{dt} - v\, cos\theta - \epsilon w\, sin\theta &= -\mathrm{Ri}\frac{\partial p}{\partial x}\,, \\
\frac{dv}{dt} + u\, cos\theta &= -\mathrm{Ri}\frac{\partial p}{\partial y} - \delta b\, cos\theta\,, \\
\epsilon^2\frac{dw}{dt} + \epsilon u\, sin\theta &= -\mathrm{Ri}\frac{\partial p}{\partial z} + \mathrm{Ri} b\, cos\theta\,, \\
\frac{db}{dt} &= 0\,, \\
\frac{\partial u}{\partial x} + \frac{\partial v}{\partial y} + \frac{\partial w}{\partial z} &= 0\,,
\end{aligned}
\tag{B.4}
$$

subject to

$$
\begin{aligned}
w|_{z=0} &= 0, \\
w|_{z=1} &= 0,
\end{aligned}
\tag{B.5}
$$

where $\mathrm{Ri} = N^2H^2U^{-2} = N^2f^2M^{-4}$ is the Richardson number, $\delta = \alpha N^2 M^{-2}$ is the slope parameter, and $\epsilon = fHU^{-1} = f^2M^{-2}$ is the non-hydrostatic parameter.

Considering a mean current flowing only in the along-shore, downcoast direction, constrained by the thermal wind relation, the mean state can be described as

$$
\begin{aligned}
u_0 &= \frac{z}{cos\theta}\,, \\
v_0 &= 0\,, \\
w_0 &= 0\,, \\
b_0 &= (cos\theta - \epsilon Ri^{-1} sin\theta)z - (\delta + 1)Ri^{-1} cos\theta\, y\,,
\end{aligned}
\tag{B.6}
$$

where $b_0 = \frac{b_0^*}{N^2 H} = \frac{N^2(z^* cos\theta - y^* sin\theta) - M^2(z^* sin\theta + y^* cos\theta)}{N^2 H}$. Assuming u_1, v_1, w_1, b_1, and p_1 are the small perturbations from the mean state, the equations governing the perturbed motion can be linearized by neglecting the product of small terms as (dropping the subscripts for clarity)

$$\begin{aligned}
\frac{\partial u}{\partial t} + u_0\frac{\partial u}{\partial x} + w\frac{\partial u_0}{\partial z} - v\ cos\theta - \epsilon w\ sin\theta &= -\mathrm{Ri}\frac{\partial p}{\partial x}\ , \\
\frac{\partial v}{\partial t} + u_0\frac{\partial v}{\partial x} + u\ cos\theta &= -\mathrm{Ri}\frac{\partial p}{\partial y} - \delta b\ cos\theta\ , \\
\epsilon^2\frac{\partial w}{\partial t} + \epsilon^2 u_0\frac{\partial w}{\partial x} + \epsilon u\ sin\ \theta &= -\mathrm{Ri}\frac{\partial p}{\partial z} + \mathrm{Ri}b\ cos\theta\ , \\
\frac{\partial b}{\partial t} + u_0\frac{\partial b}{\partial x} + v\frac{\partial b_0}{\partial y} + w\frac{\partial b_0}{\partial z} &= 0\ , \\
\frac{\partial u}{\partial x} + \frac{\partial v}{\partial y} + \frac{\partial w}{\partial z} &= 0\ .
\end{aligned} \tag{B.7}$$

Assuming an ansatz of the form $\phi = \widetilde{\phi}(z)e^{i(kx+\lambda y-\sigma t)}$, substituting the ansatz into Eq. (B.7) yields the eigenvalue problem as followed (dropping tilde accents for clarity),

$$\begin{aligned}
i(-\sigma + k\frac{z}{cos\theta})u + \frac{w}{cos\theta} - v\ cos\theta - \epsilon w\ sin\theta + ik\mathrm{Ri}p &= 0\ , \\
i(-\sigma + k\frac{z}{cos\theta})v + u\ cos\theta + i\lambda\mathrm{Ri}p + \delta b\ cos\theta &= 0\ , \\
i\epsilon^2(-\sigma + k\frac{z}{cos\theta})w + \epsilon u\ sin\ \theta - \mathrm{Ri}b\ cos\theta + \mathrm{Ri}p_z &= 0\ , \\
i(-\sigma + k\frac{z}{cos\theta})b - (\delta+1)Ri^{-1}v\ cos\theta + (cos\theta - \epsilon Ri^{-1}sin\theta)w &= 0\ , \\
iku + i\lambda v + w_z &= 0\ ,
\end{aligned} \tag{B.8}$$

subject to

$$\begin{aligned}
w|_{z=0} &= 0, \\
w|_{z=1} &= 0.
\end{aligned} \tag{B.9}$$

APPENDIX C

ROSSBY WAVE INTERACTIONS IN THE ADAPTED SAKAI MODEL

The following derivation follows Sakai (1989) but is modified to account for the presence of sloping bottom and top. The details about the interaction theory and associated derivation can be found in Section 4 and Appendix A of Sakai (1989). We will only focus on the interactions between Rossby waves. In the adapted Sakai model, the physical wave coordinates consisting of the Rossby waves in the upper and lower layers are, then,

$$\begin{aligned}
\mathbf{e}_{1n} &\equiv (u^*_{1n}, v^*_{1n}, p^*_{1n}) = (\frac{il^*_n}{f}, -\frac{ik^*}{f}, 1)e^{il^*_n y^*}, \\
\mathbf{e}_{2n} &\equiv (u^*_{2n}, v^*_{2n}, p^*_{2n}) = (\frac{il^*_n}{f}, -\frac{ik^*}{f}, 1)e^{il^*_n y^*}, \\
\sigma^*_1 &= -\frac{2k^*U_0}{2R_d^2(k^{*2}+l^{*2}_n)+1}\delta_r, \\
\sigma^*_2 &= \frac{2k^*U_0}{2R_d^2(k^{*2}+l^{*2}_n)+1}\delta_r,
\end{aligned} \tag{C.1}$$

where k^* is the dimensional along-slope wavenumber, $l^*_n = \frac{n\pi}{2Y^*_{max}}$ $(n = 1, 2, 3, ...)$ is the dimensional across-slope wavenumber, σ^* is the dimensional wave frequency, $R_d = \frac{\sqrt{\frac{1}{2}g'H_0}}{f}$ is the deformation radius, and $\delta_r = 1 + \frac{\alpha g'}{2U_0 f}$ is the slope-relative parameter. Assuming an ansatz of the form $\phi = \widetilde{\phi}(y^*)e^{i(k^*x^* - \sigma^* t^*)}$, one eigenmode in the mathematical coordinates can be projected onto the Rossby wave coordinates as followed,

$$\begin{aligned}
(\widetilde{u_1}^*, \widetilde{v_1}^*, \widetilde{w_1}^*) &= \Sigma\frac{1}{d_{1n}}A_n\mathbf{e}_{1n} = \Sigma\frac{1}{d_{1n}}A_n(u^*_{1n}, v^*_{1n}, p^*_{1n}), \\
(\widetilde{u_2}^*, \widetilde{v_2}^*, \widetilde{w_2}^*) &= \Sigma\frac{1}{d_{2n}}B_n\mathbf{e}_{2n} = \Sigma\frac{1}{d_{2n}}B_n(u^*_{2n}, v^*_{2n}, p^*_{2n}),
\end{aligned} \tag{C.2}$$

where A_n and B_n are the magnitudes in the physical wave coordinates, $d^2_{1n} \equiv \int \mathbf{E}^T_{1n} \cdot \mathbf{e}_{1n}\, dy$ ($\mathbf{E}_{1n}$ is the complex conjugate of the adjoint vector $(H^*_1 u^*_{1n}, H^*_1 v^*_{1n}, \frac{1}{g'}p^*_{1n})$) and the same for d_{2n}. The

interactions between Rossby waves can be described by

$$\begin{aligned}(\sigma^* - k^* U_0) A_n - \sigma_1^* A_n &= \epsilon_n (\sigma^* - k^* U_0) B_n, \\ (\sigma^* + k^* U_0) B_n - \sigma_2^* B_n &= \epsilon_n (\sigma^* + k^* U_0) A_n,\end{aligned} \tag{C.3}$$

where $\epsilon_n = \frac{1}{2R_d^2(k^{*2}+l_n^{*2})+1}$ is the interaction coefficient (invariant form with the presence of sloping bottom and top). Consequently, the resonance rate R^* can be obtained by eliminating A_n and B_n in Eq. (C.3):

$$R^* = Imag[\, k^* U_0 \sqrt{\frac{(1 - 2\delta_r \epsilon_n^*)^2 - \epsilon_n^{*2}}{1 - \epsilon_n^{*2}}}\,], \tag{C.4}$$

which can be reduced to the flat bottom case, $R^* = Imag[\, k^* U_0 \sqrt{1 - \frac{2}{R_d^2(k^{*2}+l_n^{*2})+1}}\,]$ (Sakai, 1989, Eq. (28)), by setting $\delta_r = 1$.

APPENDIX D

FORMULATING ELIASSEN-SAWYER EQUATION IN CYLINDRICAL COORDINATES

The linearized equations governing the perturbations in a balanced baroclinic vortex are:

$$\frac{\partial v_r^{'}}{\partial t} - (f + \frac{2V_\theta}{r})v_\theta^{'} = -\frac{1}{\rho_0}\frac{\partial p^{'}}{\partial r}, \tag{D.1}$$

$$\frac{\partial v_\theta^{'}}{\partial t} + v_r^{'}\frac{\partial V_\theta}{\partial r} + w^{'}\frac{\partial V_\theta}{\partial z} + (f + \frac{V_\theta}{r})v_r^{'} = 0, \tag{D.2}$$

$$-b^{'} = -\frac{1}{\rho_0}\frac{\partial p^{'}}{\partial z}, \tag{D.3}$$

$$\frac{\partial b^{'}}{\partial t} + v_r^{'}\frac{\partial B}{\partial r} + w^{'}\frac{\partial B}{\partial z} = 0, \tag{D.4}$$

$$\frac{\partial r v_r^{'}}{\partial r} + \frac{\partial r w^{'}}{\partial z} = 0, \tag{D.5}$$

where the capitalized variables are the background variables and the primed variables are the perturbations. Cross-differentiating Eq. (D.1) and Eq. (D.3) and eliminating $p^{'}$ lead to

$$\frac{\partial^2 v_r^{'}}{\partial t \partial z} - (f + \frac{2V_\theta}{r})\frac{\partial v_\theta^{'}}{\partial z} - \frac{2v_\theta^{'}}{r}\frac{\partial V_\theta}{\partial z} = -\frac{\partial b^{'}}{\partial r}. \tag{D.6}$$

Taking the derivative of Eq. (D.6) with respect to t and eliminating $v_\theta^{'}$ and $b^{'}$ by Eq. (D.2) and Eq. (D.4), we are left with an equation that only depends on the background variables and the perturbed velocities $v_r^{'}$ and $w^{'}$,

$$\frac{\partial^3 v_r^{'}}{\partial t^2 \partial z} + \underbrace{(f + \frac{2V_\theta}{r})\frac{\partial}{\partial z}[v_r^{'}\frac{\partial V_\theta}{\partial r} + w^{'}\frac{\partial V_\theta}{\partial z} + (f + \frac{V_\theta}{r})v_r^{'}]}_{\text{(I)}} + \underbrace{\frac{2}{r}\frac{\partial V_\theta}{\partial z}[v_r^{'}\frac{\partial V_\theta}{\partial r} + w^{'}\frac{\partial V_\theta}{\partial z} + (f + \frac{V_\theta}{r})v_r^{'}]}_{\text{(II)}}$$
$$= \frac{\partial}{\partial r}(v_r^{'}\frac{\partial B}{\partial r} + w^{'}\frac{\partial B}{\partial z}). \tag{D.7}$$

The following procedures are to simplify Eq. (D.7). First, the term (I) in Eq. (D.7) is reformed. Applying the product rule, the term (I) can be expanded as

$$Term\ (I) = \underbrace{(f+\frac{2V_\theta}{r})\frac{\partial V_\theta}{\partial r}\frac{\partial v_r^{'}}{\partial z}}_{\text{(i)}} + \underbrace{(f+\frac{2V_\theta}{r})\frac{\partial^2 V_\theta}{\partial r \partial z}v_r^{'}}_{\text{(ii)}} + \underbrace{(f+\frac{2V_\theta}{r})\frac{\partial V_\theta}{\partial z}\frac{\partial w^{'}}{\partial z}}_{\text{(iii)}} + \underbrace{(f+\frac{2V_\theta}{r})\frac{\partial^2 V_\theta}{\partial z^2}w^{'}}_{\text{(iv)}} + \underbrace{(f+\frac{2V_\theta}{r})(f+\frac{V_\theta}{r})\frac{\partial v_r^{'}}{\partial z}}_{\text{(v)}} + \underbrace{(f+\frac{2V_\theta}{r})\frac{\partial V_\theta}{\partial z}\frac{v_r^{'}}{r}}_{\text{(vi)}}. \tag{D.8}$$

Noticing $f_{eff}^{*} = \sqrt{(f+2\zeta_c)(f+\zeta_c+\zeta_s)}$, the sum of the terms (i) and (v) collapses to ${f_{eff}^{*}}^2\frac{\partial v_r^{'}}{\partial z}$. Making use of the modified thermal wind relation Eq. (3.3), the sum of the terms (iii) and (vi) becomes $-M^2\frac{\partial w^{'}}{\partial z} - M^2\frac{v_r^{'}}{r}$, and the sum of the terms (ii) and (iv) can be rewritten as

$$\begin{aligned} Term\ (ii) + Term\ (iv) &= -(f+\frac{2V_\theta}{r})(v_r^{'}\frac{\partial}{\partial r} + w^{'}\frac{\partial}{\partial z})\frac{M^2}{f+2V_\theta/r} \\ &= 2\frac{M^2}{f+2V_\theta/r}(\frac{\partial V_\theta}{\partial r} - \frac{V_\theta}{r})\frac{v_r^{'}}{r} - 2(\frac{M^2}{f+2V_\theta/r})^2\frac{w^{'}}{r}. \end{aligned} \tag{D.9}$$

Thus, the term (I) in Eq. (D.7) can be reformed as

$$Term\ (I) = {f_{eff}^{*}}^2\frac{\partial v_r^{'}}{\partial z} - M^2\frac{\partial w^{'}}{\partial z} - M^2\frac{v_r^{'}}{r} + 2\frac{M^2}{f+2V_\theta/r}(\frac{\partial V_\theta}{\partial r} - \frac{V_\theta}{r})\frac{v_r^{'}}{r} - 2(\frac{M^2}{f+2V_\theta/r})^2\frac{w^{'}}{r}. \tag{D.10}$$

Second, making use of the modified thermal wind relation Eq. (3.3), the term (II) in Eq. (D.7) can be reformed as

$$Term\ (II) = -2\frac{M^2}{f+2V_\theta/r}(f+\frac{V_\theta}{r}+\frac{\partial V_\theta}{\partial z})\frac{v_r^{'}}{r} + 2(\frac{M^2}{f+2V_\theta/r})^2\frac{w^{'}}{r}. \tag{D.11}$$

Last, substituting Eq. (D.10) and (D.11) into Eq. (D.7), it collapses to

$$\frac{\partial^3 v_r^{'}}{\partial t^2 \partial z} + {f_{eff}^{*}}^2\frac{\partial v_r^{'}}{\partial z} - M^2\frac{\partial w^{'}}{\partial z} - \frac{3M^2}{r}v_r^{'} = \frac{\partial}{\partial r}(-M^2 v_r^{'} + N^2 w^{'}). \tag{D.12}$$

With the modified thermal wind relation Eq. (3.3) and a little algebra, we can obtain $\frac{\partial {f^*_{eff}}^2}{\partial z} = -\frac{3M^2}{r}$, and hence Eq. (D.12) can be expressed as

$$\frac{\partial^3 v_r^{'}}{\partial t^2 \partial z} + \frac{\partial}{\partial r}(M^2 v_r^{'} - N^2 w^{'}) + \frac{\partial}{\partial z}({f^*_{eff}}^2 v_r^{'} - M^2 w^{'}) = 0. \tag{D.13}$$

According to Eq. (D.5), we can introducing a stream function Φ such that $v_r^{'} = \frac{1}{r}\frac{\partial \Phi}{\partial z}$ and $w^{'} = -\frac{1}{r}\frac{\partial \Phi}{\partial r}$, and hence Eq. (D.13) can be rewritten as a single PDE for the stream function Φ,

$$\frac{1}{r}\frac{\partial^4 \Phi}{\partial t^2 \partial z^2} + \frac{\partial}{\partial r}(\frac{N^2}{r}\frac{\partial \Phi}{\partial r} + \frac{M^2}{r}\frac{\partial \Phi}{\partial z}) + \frac{\partial}{\partial z}(\frac{M^2}{r}\frac{\partial \Phi}{\partial r} + \frac{{f^*_{eff}}^2}{r}\frac{\partial \Phi}{\partial z}) = 0, \tag{D.14}$$

which is the time-dependent Eliassen-Sawyer equation in cylindrical coordinates.

APPENDIX E

PARCEL ARGUMENTS IN A BAROCLINIC VORTEX

The following parcel argument closely follows Whitt and Thomas (2013) but relies on the principle of the absolute angular momentum conservation. The strategy is to link the perturbation variables to the parcel displacement and then to express the restoring force as a function of the displacement.

Consider a fluid parcel that is displaced from its neutral position with the displacement $\vec{\delta} = R\vec{i} + Z\vec{k}$. $v_\theta^{'}$ can be obtained by applying the absolute angular momentum conservation. The total absolute angular momentum L_t of a fluid parcel in a vortex is

$$L_t = rv_\theta^{'} + rV_\theta + \frac{1}{2}fr^2 = rv_\theta^{'} + L_b, \tag{E.1}$$

where $L_b = rV_\theta + \frac{1}{2}fr^2$ is the background absolute angular momentum. The conservation $\Delta L_t = 0$ yields $\Delta rv_\theta^{'} = -\Delta L_b$ – the change of L_b will induce the change of $v_\theta^{'}$. Assuming that the parcel is initially at rest, i.e., $v_\theta^{'}|_{t=0} = 0$, $v_\theta^{'}(t)$ after the displacement becomes

$$v_\theta^{'}(t) = -\frac{1}{r}\Delta L_b = -\frac{1}{r}\nabla L_b \cdot \vec{\delta} = -(f + \zeta_c + \zeta_s)R - \frac{\partial V_\theta}{\partial z}Z. \tag{E.2}$$

Making use of the buoyancy conservation, $b^{'}(t)$ after the displacement becomes

$$b^{'}(t) = -\nabla B \cdot \vec{\delta} = M^2R - N^2Z. \tag{E.3}$$

Next is to express the restoring force as a function of the displacement. Assuming that the pressure of the parcel can be instantaneously adjusted to the background pressure, the radial component of the restoring force F_R and the vertical component F_Z can be expressed as functions of the displacement (R, Z) by using the momentum equations in Eq. (3.5) and the expressions of $v_\theta^{'}$

and $b^{'}$ (Eq. (E.2) and (E.3)),

$$\begin{aligned} F_R &\equiv \frac{dv_r^{'}}{dt} = (f + 2\zeta_c)v_\theta^{'} = -{f_{eff}^*}^2 R + M^2 Z, \\ F_Z &\equiv \frac{dw^{'}}{dt} = b^{'} = M^2 R - N^2 Z. \end{aligned} \tag{E.4}$$

Projecting F_R and F_Z on the oscillating path yields the total restoring forcing

$$F_\delta = (-{f_{eff}^*}^2 + 2M^2 S_\delta - N^2 S_\delta^2)\delta, \tag{E.5}$$

where $S_\delta = Z/R$ is the displacement slope. Consequently, the oscillating frequency as a function of S_δ is

$$\sigma = \sqrt{{f_{eff}^*}^2 - 2M^2 S_\delta + N^2 S_\delta^2}. \tag{E.6}$$